Annual Report of Research Performed on the HIBALL Project Between 1 January and 31 December 1982 by Fusion Power Associates for the Kernforschungszentrum Karlsruhe GmbH, Karlsruhe, FRG

B. Badger, D. Bruggink, M.L. Corradini, R. Engelstad, G.L. Kulcinski, E.M. Larsen, G.A. Moses, R.R. Peterson, K.E. Plute, L. Pong, M.E. Sawan, I.N. Sviatoslavsky, K.R. Symon, D.K. Sze, W.F. Vogelsang, A. White

December 31,

FPA-82-6

FUSION POWER ASSOCIATES

2 Professional Drive, Suite 248
Gaithersburg, Maryland 20879
(301) 258-0545

1500 Engineering Drive
Madison, Wisconsin 53706
(608) 263-2308

ANNUAL REPORT

of

RESEARCH PERFORMED ON THE HIBALL PROJECT

between

JANUARY 1 and DECEMBER 31, 1982

by

FUSION POWER ASSOCIATES

for the

KERNFORSCHUNGSZENTRUM KARLSRUHE, GmbH

Karlsruhe, Federal Republic of Germany

B. Badger
D. Bruggink
M. Corradini
R. Engelstad
G. Kulcinski
E. Larsen
E. Lovell
G. Moses
R. Peterson
K. Plute
L. Pong
M. Sawan
I. Sviatoslavsky
K. Symon
D. Sze
W. Vogelsang
A. White

FPA-82-6

December 31, 1982

TABLE OF CONTENTS

1. Introduction

This report is a summary of the work performed on the HIBALL reactor by Fusion Power Associates during 1982. It was recognized at the time the HIBALL report was issued that much work remained to be done to verify or expand on considerations important to the design. Among the items to be considered were: final focusing magnet placement and beam line neutronics including the energy dumps for the beam lines, further development of the treatment of the condensing vapor in the cavity, expanded design and evaluation of the cavity "roof", further characterization of the silicon carbide fibers, radioactivity in the cavity and beam lines, and tritium leakage through the steam generator and other reactor components and systems. During 1982, a major revision of the accelerator system was made. These changes, while extensive, have not had a great impact on the design of the cavity. The principal change that concerns the cavity is the change from Bi^{2+} to Bi^{1+} ions. This change affects the final focusing magnets and thus the neutronics and radioactivity calculations for the beam lines. The other effect of the accelerator changes is in the projected costs of the revised system. A section assessing these cost changes has been included. To distinguish between the two accelerator designs the later one incorporating Bi^{1+} will, for the purposes of this report, be referred to as HIBALL-II. A section reviewing some of the safety aspects of HIBALL from the U.S. licensing point of view has also been included for comparison with the German situation.

There are other questions of interest which must be answered to insure the viability of the HIBALL concept. The final section of the report addresses some of these questions as areas for future study and investigation.

2. Evaporation and Recondensation of PbLi in the HIBALL Target Chamber

2.1 Introduction

The determination of the density of PbLi vapor in the reactor target chamber is one of the most serious and difficult problems of the HIBALL design. This is a serious issue because, since we have chosen to focus the ion beams on the target ballistically, the vapor density in the target chamber must be rather low at the time the beam is injected into the cavity. Large amounts of PbLi vapor are vaporized from the INPORT tubes (see Fig. 2.1) by target explosion generated x-rays and considerable time is needed for the vapor density to drop to the needed level through recondensation on the INPORT tubes and walls of the chamber. This recondensation time limits the rep rate of the reactor target chamber and thus affects the number of reactor cavities needed by the plant to generate a given output power.

Our original analysis of the problem, which was presented in the HIBALL report,(1) predicted that a rep rate of 5 Hz would be possible in each target chamber. This was based on a physical model for the Pb-Li vapor which accounted for vaporization off the INPORT units by x-rays and by thermal radiation and for condensation through viscous flow back onto the INPORT units. In this model, the thermal radiation on the INPORT units was calculated with the one-dimensional Lagrangian radiation transport computer simulation code FIRE,(2) which treats the radiation transport in the vapor as a diffusion process. For this radiation transport calculation, we assumed that the vapor starts near the INPORT units and then is allowed to flow hydrodynamically towards the center of the target chamber. This is shown in Fig. 2.2. The radiation transport is calculated while the vapor is moving but the mass of the vapor has heen held constant; that is, we neglected the effects on the

Fig. 2.1 HIBALL target chamber with INPORT (SiC) tubes.

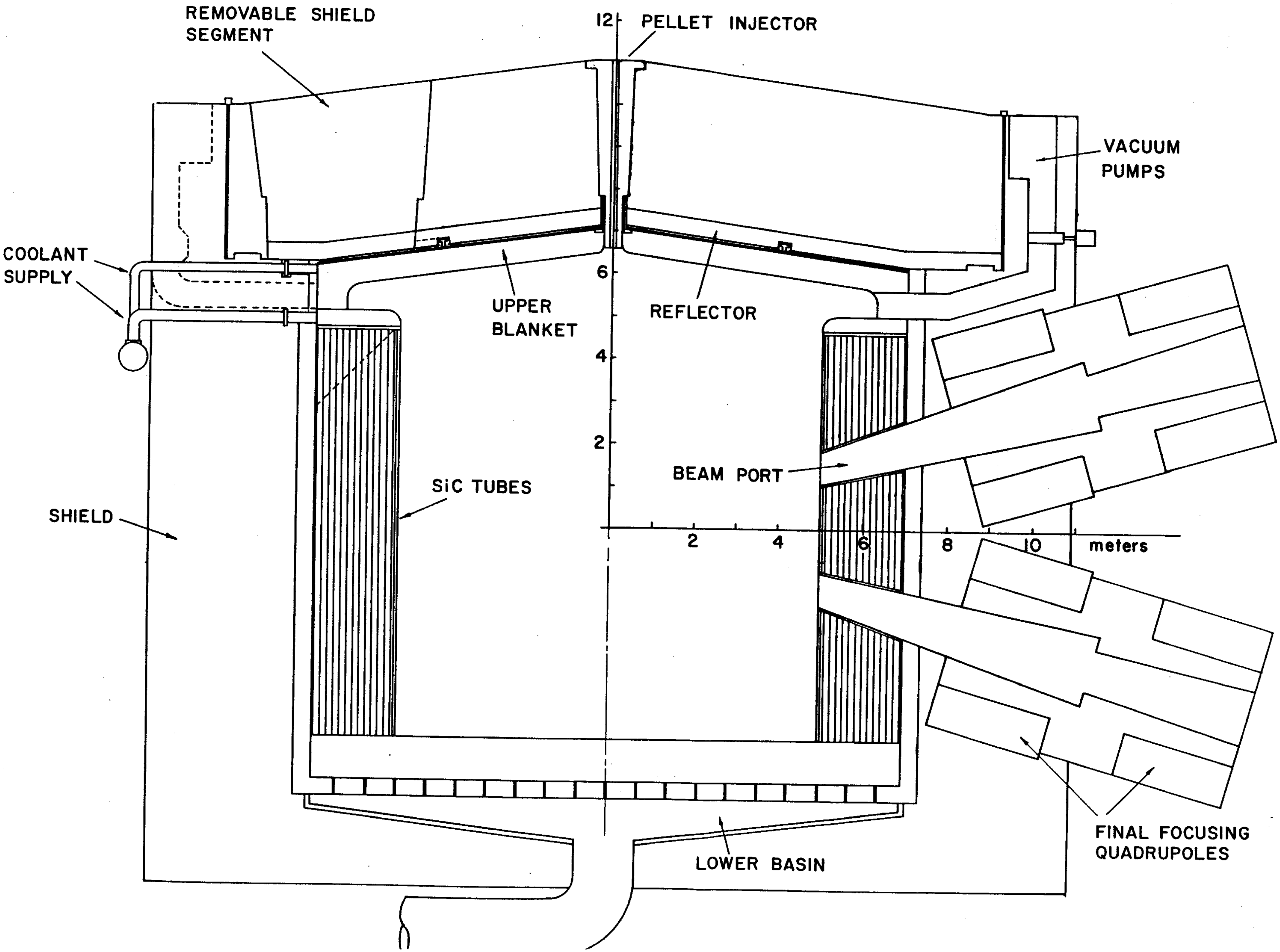

Fig. 2-2 Hydrodynamic motion of PbLi vapor.

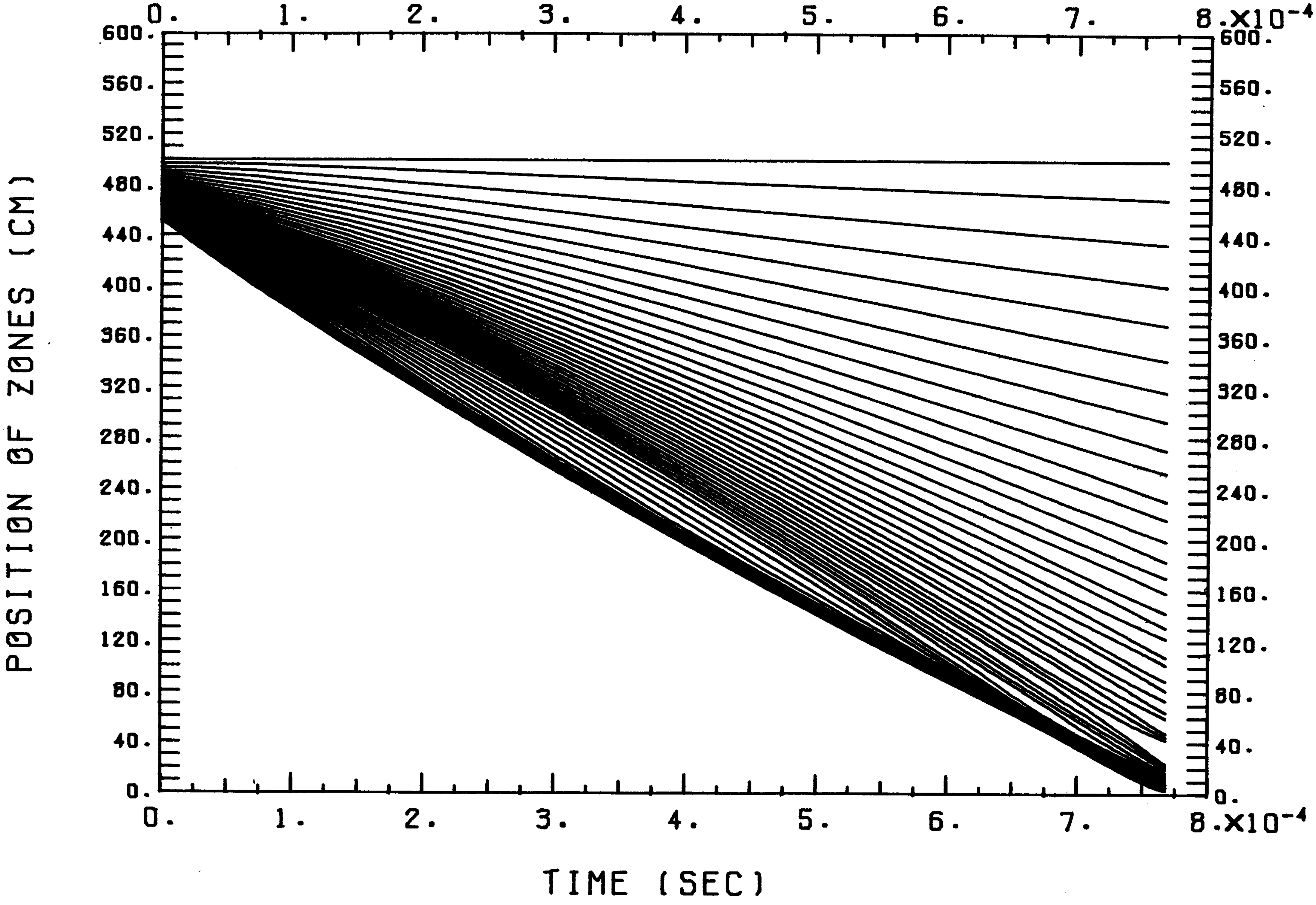

thermal heat flux of additional vaporization due to the thermal heat flux on the INPORT units and of condensation. The average cavity gas density predicted by this model is shown in Fig. 2.3. Since the density changes by many orders of magnitude during the time between shots, we felt that there may be large corrections needed to be made to the heat flux.

Since the publication of the HIBALL report in December 1981, we have made improvements to the analysis of the condensation of the PbLi vapor. A new computer code, CONRAD, has been constructed which does the radiation transfer calculations as FIRE does, but it allows the total mass of the radiating vapor to change as condensation and vaporization occur. This code is still under development but we have obtained some results over the past year.(3) We have also embarked on a study of the basic physics of the condensation and vaporization. The next two sections of this chapter will be devoted to description of the progress of these two efforts and discussion of what can be done in the future. The final section reports on new atomic physics data which may have an effect on the density needed for ballistic beam propagation.

2.2 Computer Simulation with CONRAD

CONRAD is a one-dimensional Lagrangian radiation transfer hydrodynamics computer code. The physical processes that we are attempting to model are depicted in Fig. 2.4. Here, the vaporization and condensation process is followed in time from the absorption of the target generated x-rays in the PbLi film on the INPORT units through to the condensation of the PbLi vapor back onto the film. After a target explosion, the x-ray energy is deposited in 10^{-3} cm of the liquid film, which is flowing down the outside of the SiC porous tubes. The temperature of the $Pb_{83}Li_{17}$ is raised above its boiling temperature and the $Pb_{83}Li_{17}$ is vaporized. The evaporated Li and Pb vapor

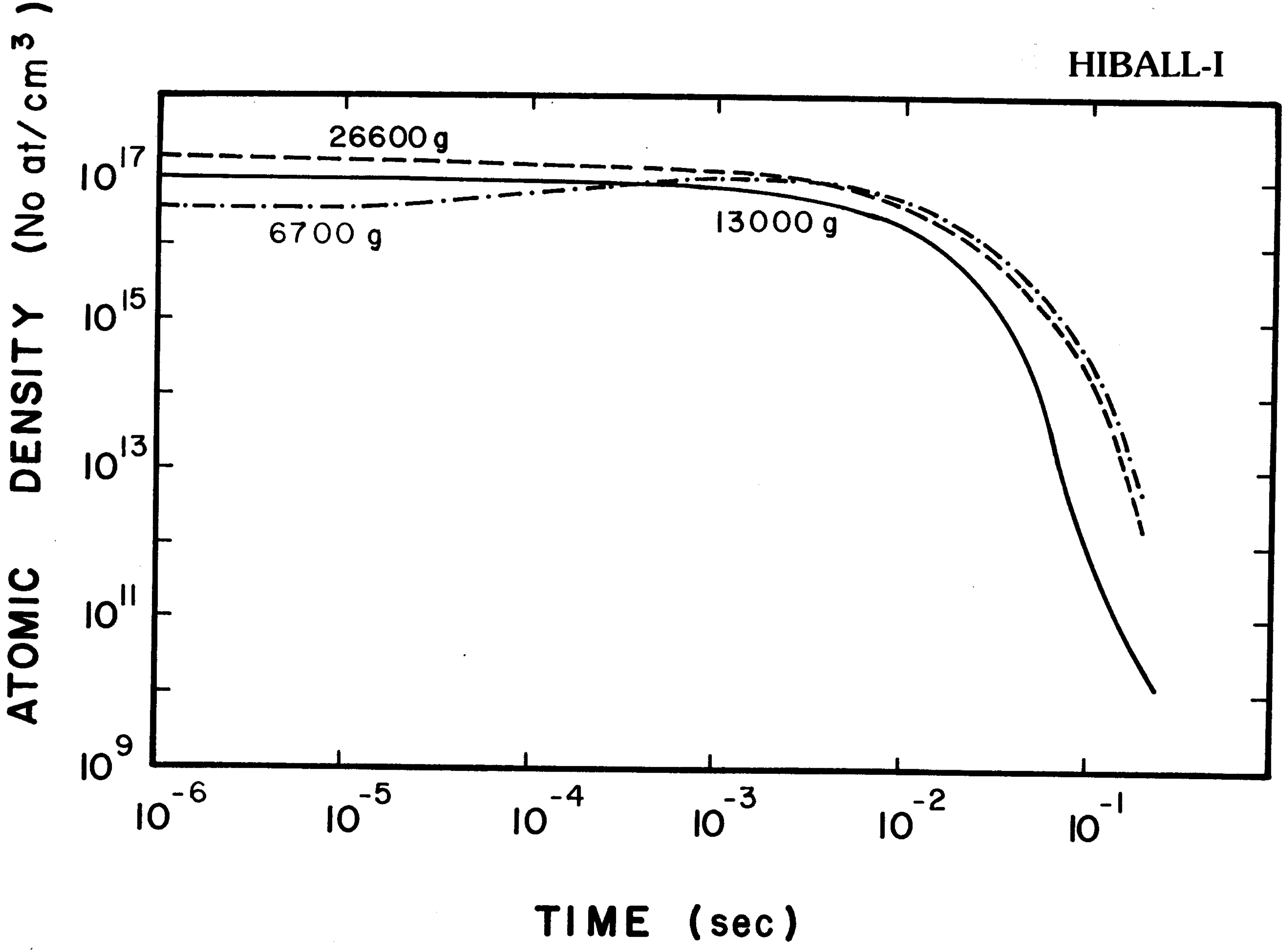

Fig. 2.3 Atomic density versus time for different masses of vaporized gas.

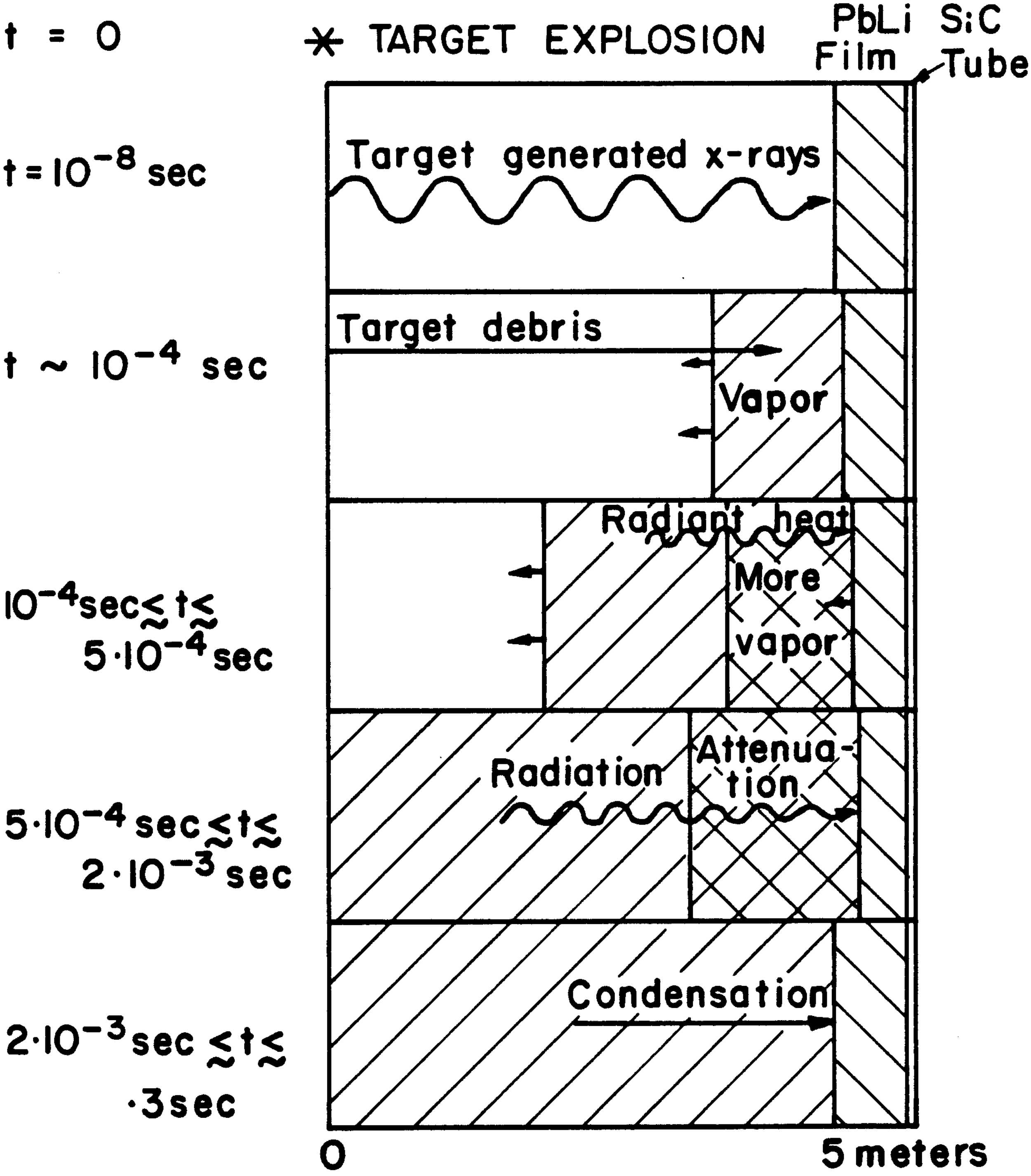

Figure 2.4 History of the $Li_{17}Pb_{83}$ Vapor

flow into the chamber and their temperature is further raised by absorbing the energy of the debris. Thus the first surface is also protected from the energetic ion debris. The hot gas then starts to radiate energy back to the INPORT tubes, causing additional $Pb_{83}Li_{17}$ to be evaporated into the chamber. The radiational heat will decrease because of the bulk gas cooling, and also because of the increasing gas opacity from the addition of mass. The cooling gas will condense back on the surface and deposit its energy, resulting in further $Pb_{83}Li_{17}$ evaporation.

The gas density is quite high after the inital x-ray deposition, and varies by the coupled effects of condensation and evaporation. For the target and debris spectra of HIBALL, a total of 13 kg of $Pb_{83}Li_{17}$ was calculated to be evaporated.(4) We have calculated the gas radiation, condensation and evaporation, based on the following conditions and assumptions:

1. By neglecting the curvature effect of the reactor chamber, we did a one-dimensional calculation.
2. Since the mass fraction of Li in the $Pb_{83}Li_{17}$ alloy is quite small (~ 0.6%), we assume all radiation, condensation and evaporation are due to Pb only.
3. The thermophysical properties of liquid $Pb_{83}Li_{17}$ are independent of temperature.
4. This calculation begins right after the liquid $Pb_{83}Li_{17}$ is blown off from the surface by absorption of high energy x-rays.
5. The ionization of the gas is assumed to occur in either Saha(5) or Coronal(6) model.
6. The radiative processes follow a semi-classical formalism.(7)

7. Condensation and evaporation happen within a few mean free paths from the liquid film.
8. According to its kinetic energy, the evaporated mass is assumed to stop in a certain ρR and uniformly distributes into this region.
9. Assume the conditions (pressure, temperature) of the liquid film are in static thermal equilibrium.
10. Assume all the molecules approaching the surface will condense, and all the molecules leaving the surface will eventually escape from the surface, neglecting the collisions between the condensed and evaporated particles.
11. Neglect the noncondensible gas (D, T, He) effect on the heat and mass transfer.
12. The thickness of the film is 1.5 mm.
13. Coolant temperature is 324°C and the heat transfer coefficient is 12 W/cm^2 °C.

CONRAD was developed to simulate this process by incorporating a heat transfer, vaporization and evaporation code into FIRE. CONRAD uses data for PbLi which was generated by the atomic physics code MIXERG. The analysis has been achieved with several coupled computer codes. We obtained the x-ray spectrum from a target burn simulation.(1) Deposition of the x-rays and creation of the vapor were modeled by an x-ray stopping code.(4) The major changes compared to our previous calculations are:

a) Combined gas radiation, evaporation and condensation effects. Before we first assumed the gas density was uniform, then calculated the history of radiation heat flux and the gas temperature from the FIRE(2) code. Using those data as the input to the first surface, we calculated the $Pb_{83}Li_{17}$

condensation and evaporation. This method is inconsistent since the evaporated and condensed mass will have a significant effect on the gas radiation, so in this calculation we combined those effects. The exchange of mass and energy between the bulk gas and the first surface is shown in Fig. 2.5. Q is the heat flux due to radiation, condensation and evaporation. G is the mass flux leaving or arriving at the surface. P, T are the pressure and temperature.

b) Use of a better model to modify the ionization state. We use both the Coronal and Saha models to describe the ionization at low and high gas density. This provides us with a more accurate set of data than previously for charge state, specific internal energy, Rosseland mean free path and Planck mean free path. For example, the charge state is shown in Fig. 2.6. The black line separates the regions in which either the Coronal or Saha model dominates.

For 13 kg initial evaporated mass after the x-ray deposition, the calculation results are shown in Figs. 2.7 through 2.10. Figure 2.7 shows the hydrodynamic motion of the $Pb_{83}Li_{17}$ gas. At about 1 msec, the gas reaches the cavity center. Figure 2.8 shows the surface heating due to radiation, evaporation and condensation. At the beginning the radiation and evaporation dominate; later, the condensation dominates. The peaks in the figure occur because at this time, the gas reaches the center and we assume that the gas converts its kinetic energy into heat. Figures 2.9 and 2.10 compare the history of the gas density with the old calculation and the improved calculation in linear and logarithmic plots. From these results, we can summarize the whole gas dynamic process into 9 states (Fig. 2.4):

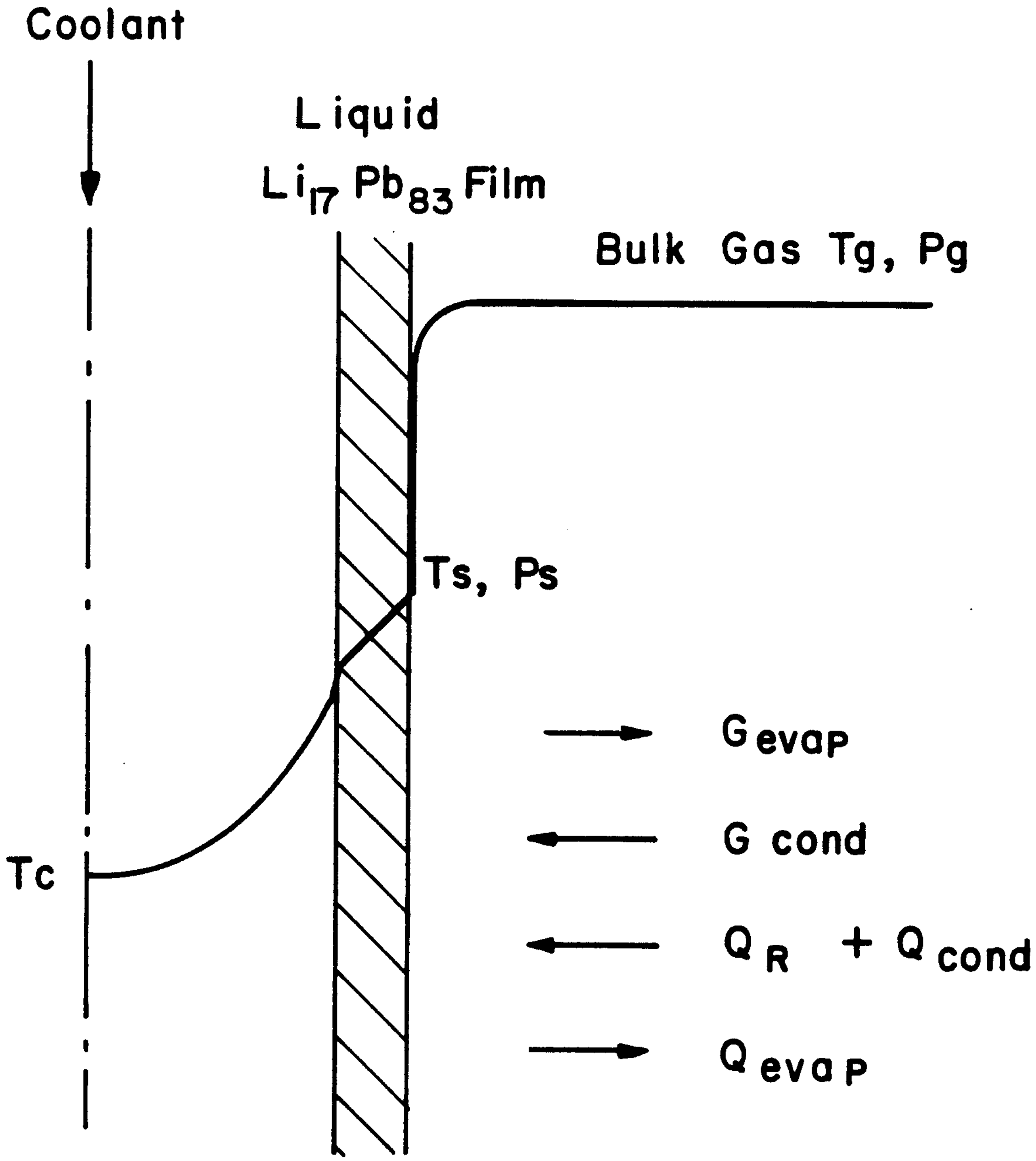

Figure 2.5 The exchange of mass, energy between the bulk gas and the first surface.

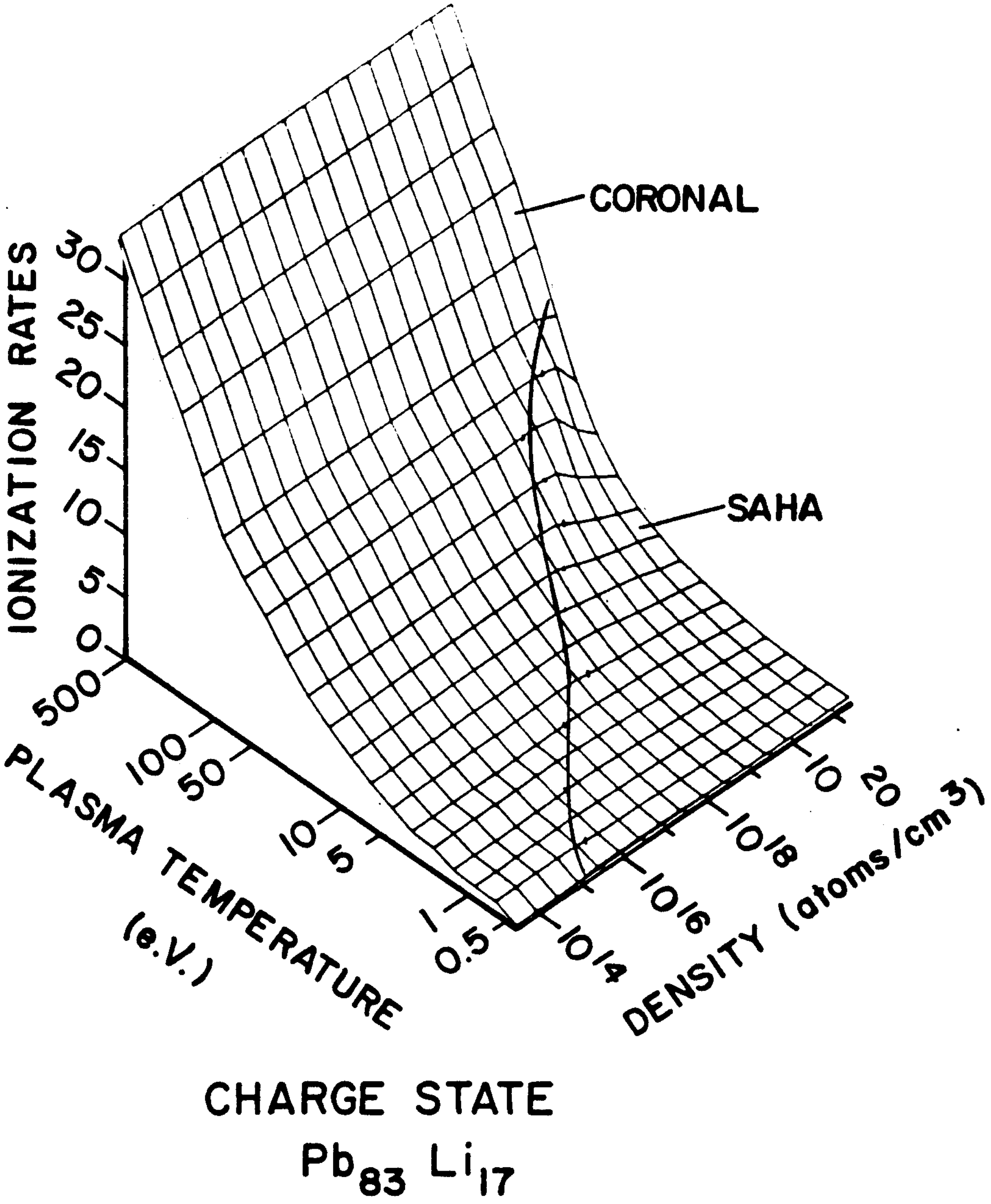

Figure 2.6 Ionization state for $Li_{17}Pb_{83}$ in Saha and Coronal model.

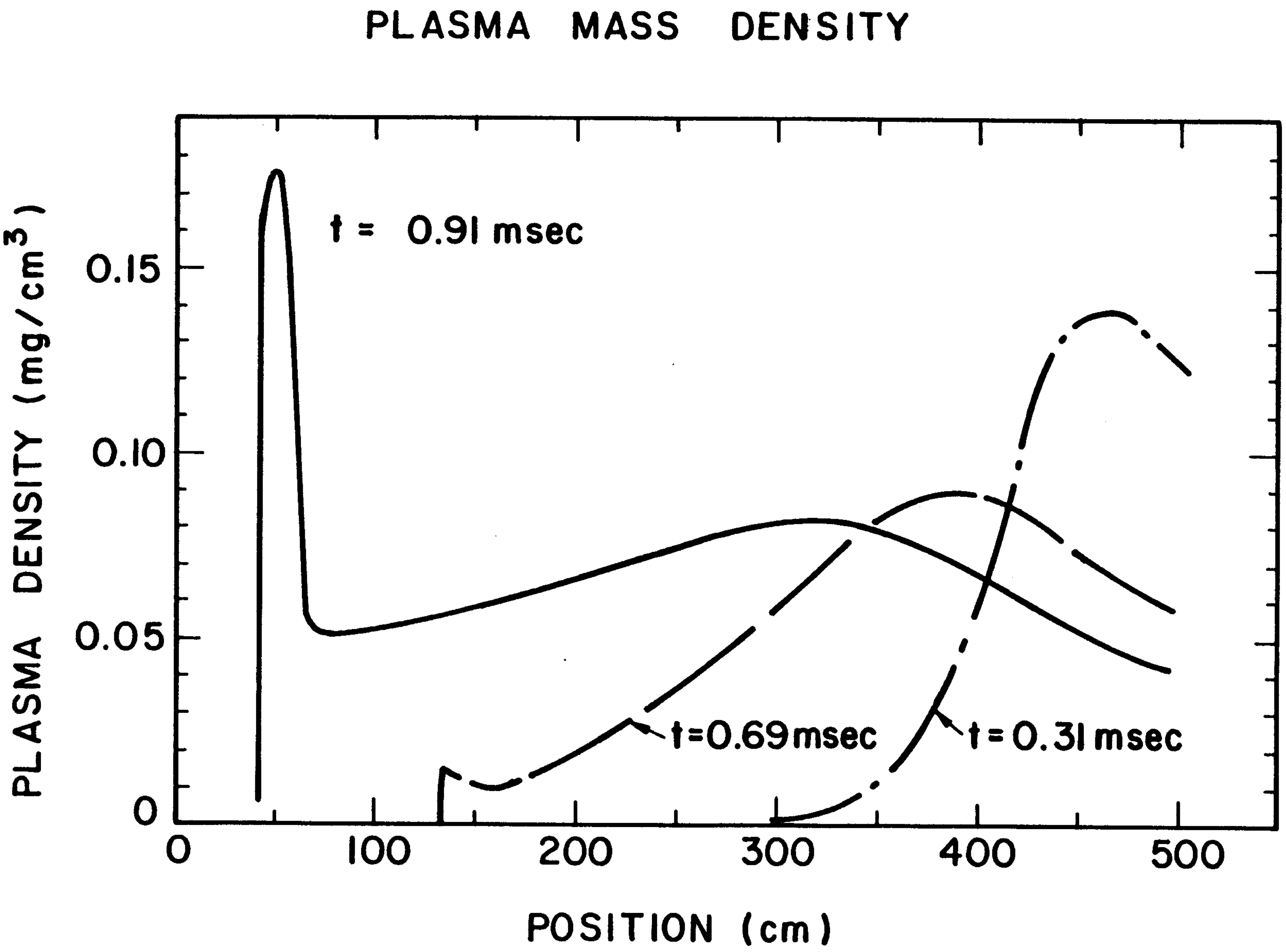

Figure 2.7 Hydrodynamic motion of $Li_{17}Pb_{83}$ vapor moving from tubes to cavity center.

Figure 2.8 First surface heat flux from radiation, condensation and evaporation.

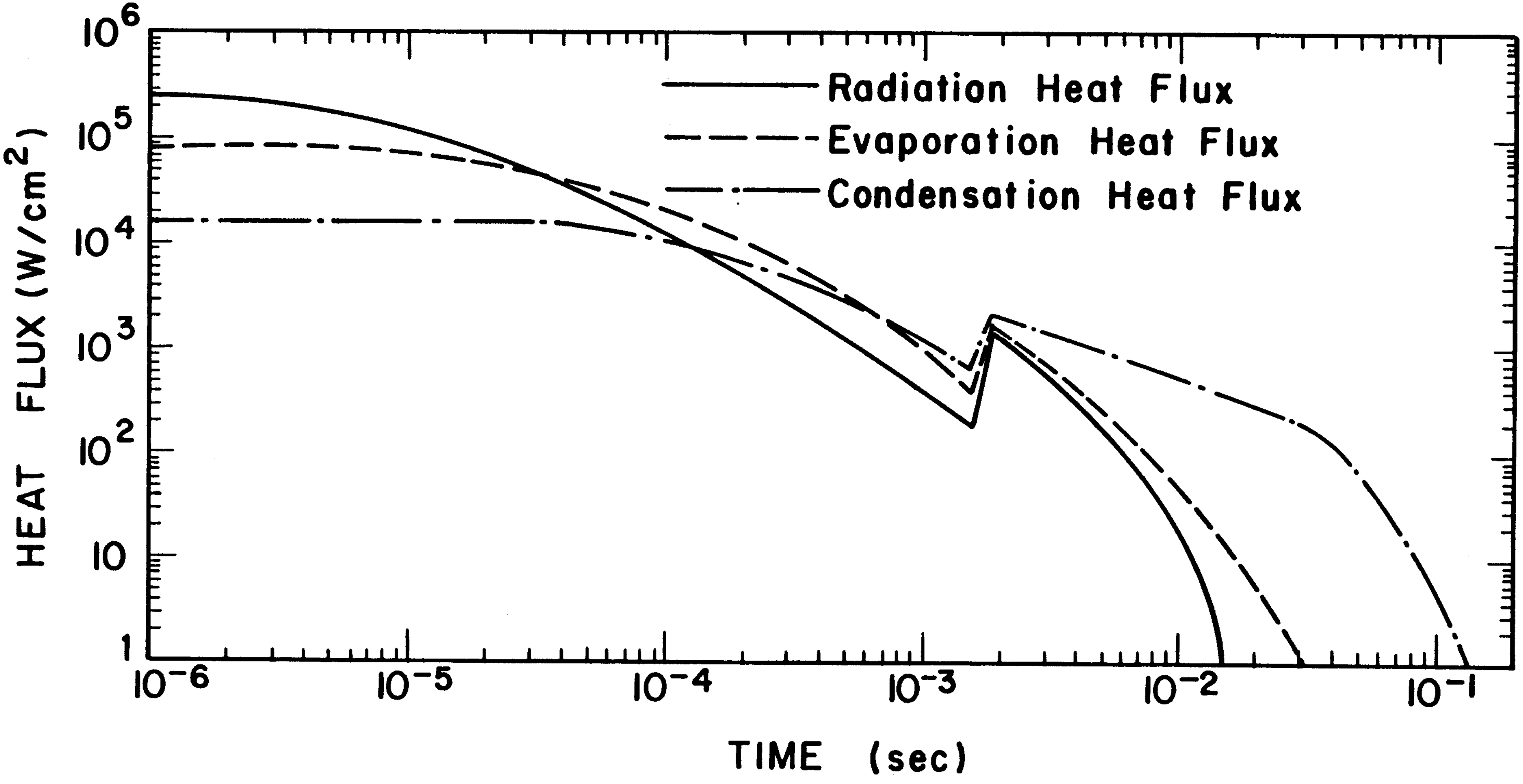

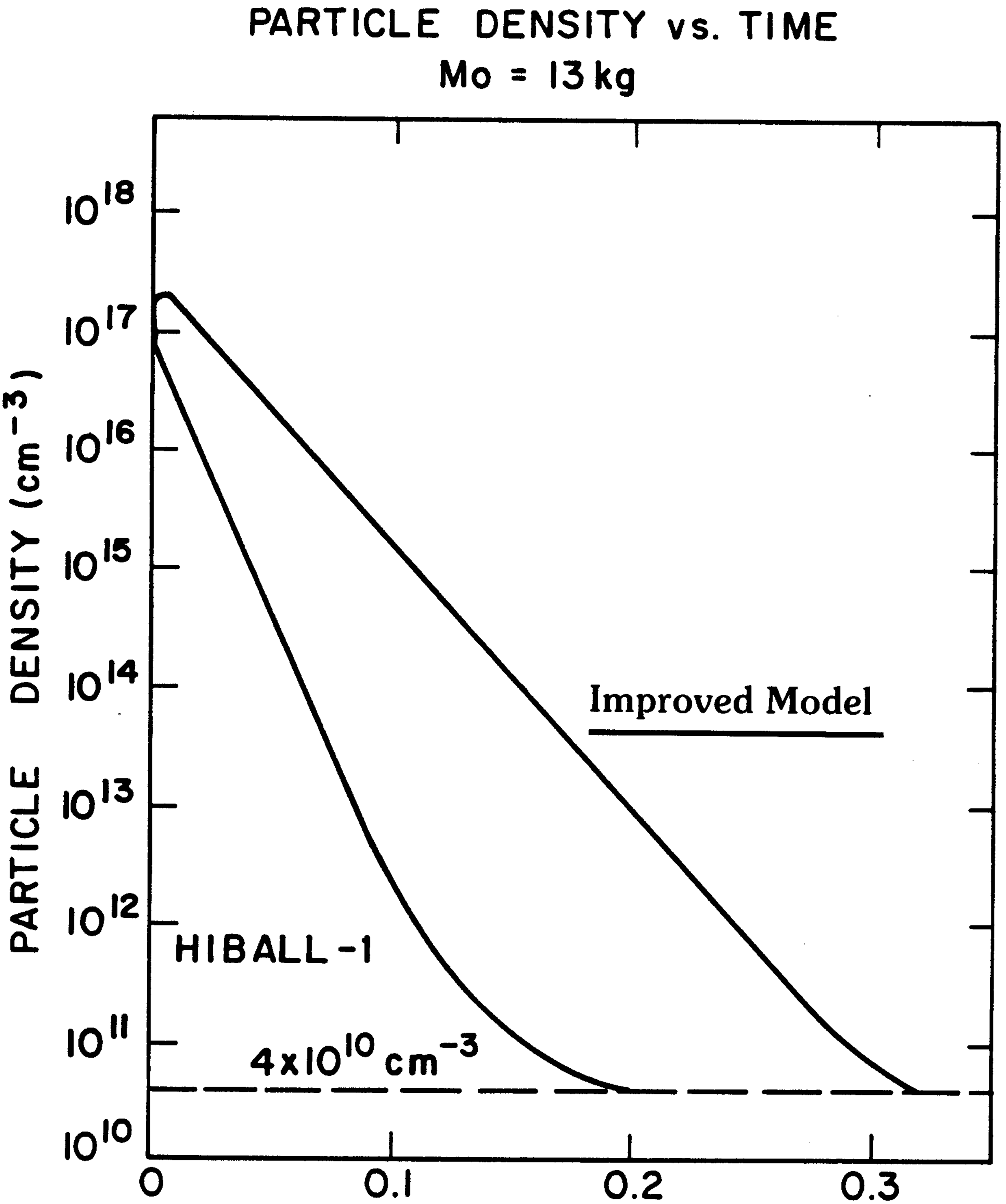

Figure 2.9 Cavity density versus time -- linear plot.

Figure 2.10 Cavity density versus time -- logarithmic plot.

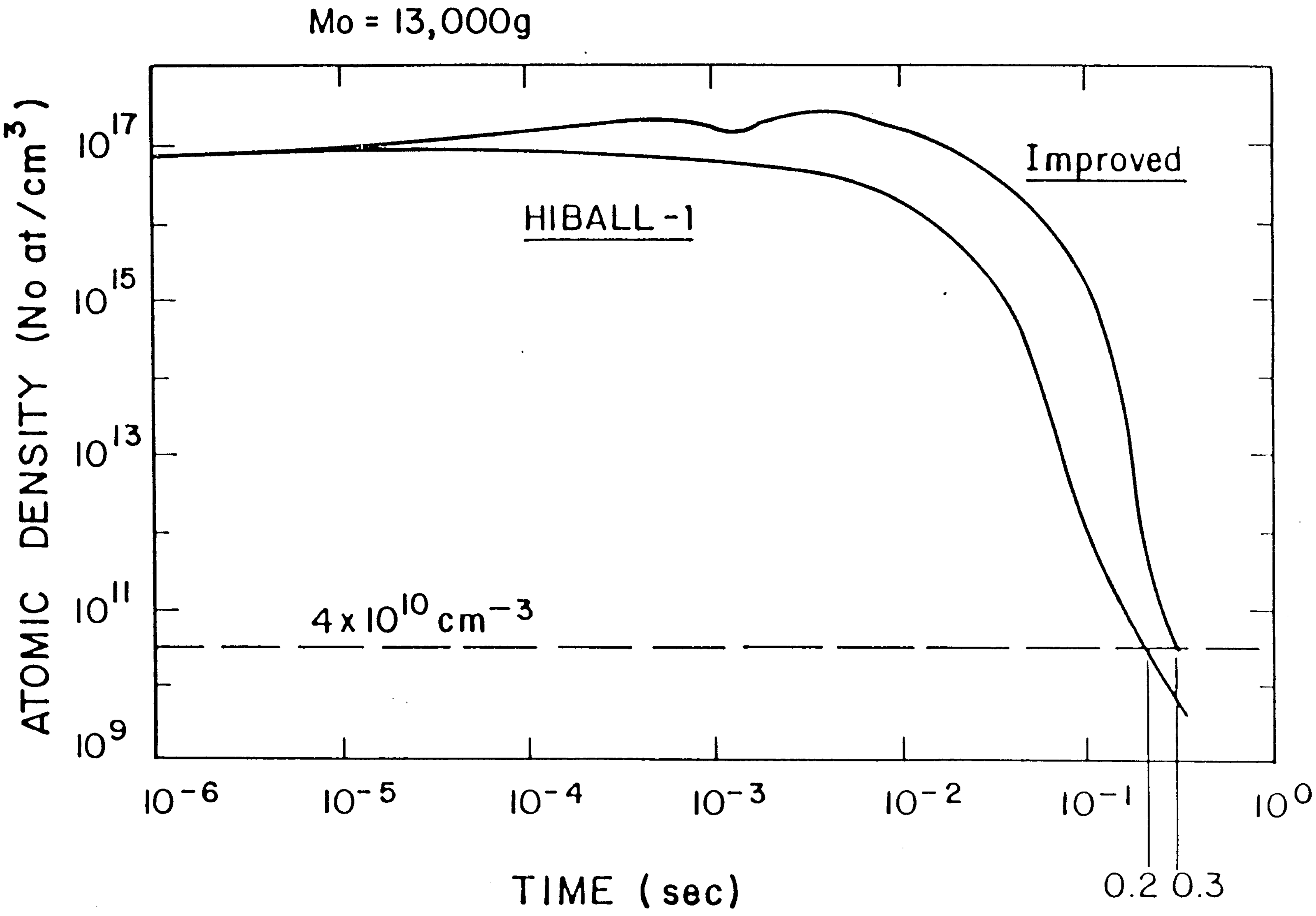

1. Target explosion.
2. The film is vaporized by the x-rays.
3. The vapor begins moving toward the target and absorbs the energy of the ions. After about 10^{-4} sec, the vapor temperature is raised to about 1.3 eV.
4. The gas continues flowing toward the center and begins radiating energy onto the INPORT tubes.
5. Additional $Pb_{83}Li_{17}$ is evaporated off of the tubes by this radiation heat flux.
6. The radiation heat flux reaching the tube surface is decreasing because of the increased amount of vaporized mass increasing the opacity of the gas.
7. Around 1 msec, the gas reaches the center and converts its kinetic energy into heat. This causes much $Pb_{83}Li_{17}$ evaporation.
8. The cooling gas condenses back onto the tubes.
9. After about 0.3 sec, the gas density will be below 4 x $10^{10}/cm^3$.

For HIBALL-I with 5 Hz repetition rate, our calculation shows that at 0.2 sec, the gas density is about 9 x $10^{12}/cm^3$. However, we note that there are some uncertainties involved in this calculation. From the target burn calculation, we know the total energy (includes x-ray and debris) input to the first surface should be 34.5 J/cm^2. At the end of our calculation, we got only 26.9 J/cm^2. This means we have a cooler gas than we actually predicted. If we have a hotter gas, the radiation heat flux will be higher, and there will be more gas evaporated. Also a hotter gas might have a higher kinetic energy. It will move to the surface more quickly, causing a higher condensation rate. There are a number of assumptions made in this analysis that require further study. For large condensation and evaporation rates we must modify assumptions 9 and 10. Futhermore, we now believe that the presence of noncondensible gases (T, D, and He) will have an effect on the condensation rate so that assumption 11 may not be fully justified.

The results presented here show that the gas recondenses to below 4 x 10^{10} cm^{-3} in 0.3 seconds and thus the maximum repetition rate is 3 Hz. However, the above discussion indicates that we are only beginning to understand this complex dynamic phenomenon and work is continuing to gain better insight into the problem.

2.3 Work on Basics of Vaporization and Condensation

The problem of liquid metal vapor condensation is critical to the HIBALL design. It is also critical to similar designs such as HYLIFE. For this reason we have chosen to go beyond the simple analysis used in the HIBALL design and study this problem in depth. We have reviewed the general problem of a vapor condensing in the presence of a noncondensible gas. In the case of HIBALL this noncondensible gas is the residual He and unburnt DT in the cavity. This review shows that:

1. Owing to the low mean free path of the vapor a nonequilibrium region exists near the condensation surface that causes the values of the temperature and pressure of the vapor to deviate from the surface temperature and the saturation pressure corresponding to the surface temperature. This region is called the "Knudsen layer."
2. A kinetic theory treatment of metal evaporation from a surface tells us that beyond a plane ~ 4 or 5 mean free paths from the surface, a hydrodynamic description becomes valid. In addition, the time required to reach steady state is about 100 vapor time constants.(8)

3. The noncondensible gas has a profound effect on the condensation rate. Because of the collisions with vapor, the noncondensible gas tends to collect at the lower temperature surface. Hence the vapor has to diffuse through the noncondensible gas layer, so the mass transfer will be reduced. Takeo(9) showed that the induced resistance for vapor mass flux is proportional to the total number density of noncondensible gas when it is concentrated in the thickness of one vapor mean free path divided by the average number density of vapor.

From the literature we have categorized two types of kinetic theory approaches to solving the condensation problem. The first approach is the so-called weak condensation.(9-11) This problem is shown in Fig. 2.11. The assumptions used here are:

1. one dimension;
2. steady state;
3. two surfaces with slightly different temperatures; and
4. condensible and noncondensible gas present.

The basic equations describing this problem start from the Gross-Krook equation for binary mixtures:

$$v_{xi} \frac{\partial f_i}{\partial x} = \nu_{ii}(F_i - f_i) + \nu_{ij}(\tilde{F}_i - f_i) \qquad i = 1,2$$

where: f_i = the distribution function for species i

ν_{ii},ν_{ij} = collision frequency

$F_i,\tilde{F}_i$ = local Maxwellian distribution

$$F_i = n_i(2\pi R_i T_i)^{-3/2} \exp[-(v_i - U_i)^2/2RT_i]$$

$$\tilde{F}_i = n_i(2\pi R_i \tilde{T}_i)^{-3/2} \exp[-(v_i - \tilde{U}_i)^2/2R\tilde{T}_i] \ .$$

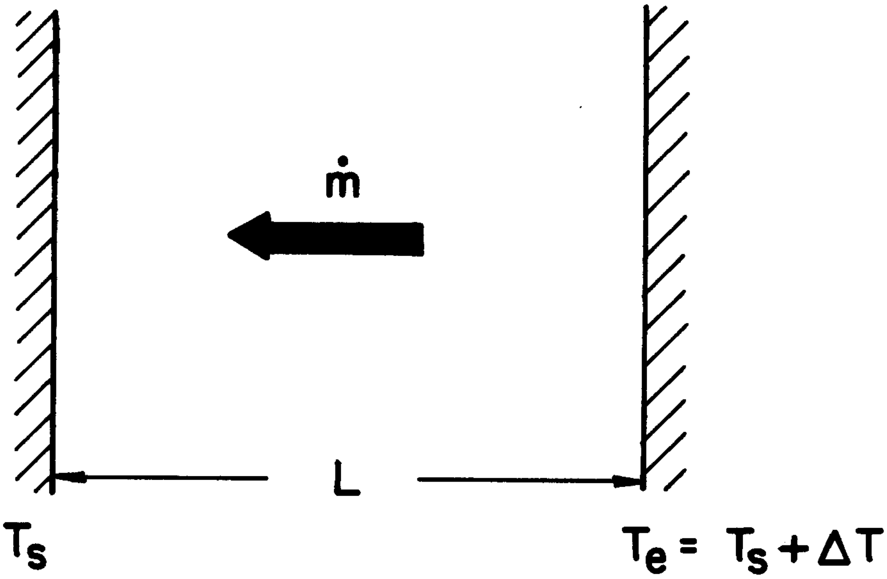

Fig. 2.11 Weak condensation.

Next we introduce the reduced distribution functions g and h:

$$g(x,v_x) = \iint_{-\infty}^{\infty} f \, dv_g dv_z$$

$$h(x,v_x) = \iint_{-\infty}^{\infty} (v_y^2 + v_z^2) f \, dv_y dv_z$$

$$v_{xi} \frac{\partial g_i}{\partial x} = A_{ii}\nu_{ii}(G_i - g_i) + A_{ij}\nu_{ij}(\tilde{G}_i - g_i) \qquad (2.1a)$$

$$v_{xi} \frac{\partial h_i}{\partial x} = A_{ii}\nu_{ii}(H_i - h_i) + A_{ij}\nu_{ij}(\tilde{H}_i - h_i) \; . \qquad (2.1b)$$

Then we assume:

1. All particles impinging onto the surface of the condensed phase are captured.
2. The vapor emitted from the surface has a Maxwellian distribution

$$F_1(x=0) = n_{1S}(2\pi R_1 T_S)^{-3/2} \exp(-v_1^2/2R_1T_S) \qquad v_{x1} > 0$$

$$F_1(x=L) = n_{1L}(2\pi R_1 T_e)^{-3/2} \exp(-v_1^2/2R_1T_e) \qquad v_{x1} < 0$$

3. The surface is impermeable to the noncondensible gas, so the mean velocity of noncondensible gas will be zero.
4. The conservation of noncondensible gas gives

$$\int_0^L n_2 \, dx = n_{2S}L \; .$$

5. The noncondensible gas reflects from the surface with a Maxwellian distribution:

$$f_2(x=0) = n_{2S}(2\pi R_2 T_S)^{-3/2} \exp(-v_2^2/2R_2T_S) \qquad v_{x2} > 0$$

$$f_2(x=L) = n_{2L}(2\pi R_2 T_e)^{-3/2} \exp(-v_2^2/2R_2T_e) \qquad v_{x2} < 0 \, .$$

The temperature difference between these two surfaces is assumed to be small, hence the exchange of mass and energy flux must be small. The authors linearize Eqs. (2.1a) and (2.1b), and use either a finite difference method or half range Hermite polynomials to solve the equations.

The second kinetic theory approach is for intensive condensation.(12) This is shown schematically in Fig. 2.12. Here the authors make the assumptions:

1. one dimension;
2. steady state; and
3. condensible gas only.

We divide the problem into two regions.

1. Region I (gas dynamic region): collision dominant, able to study the behavior of vapor on the basis of continuum mechanics considerations.
2. Region II (Knudsen layer): within this layer (~ several mean free paths), the ordinary macroscopic characteristics and the resulting gradient type transfer equations are invalid and a kinetic theory approach is required.

This problem can be solved by assuming:

1. In region I, the particles have the equilibrium Maxwellian distribution.

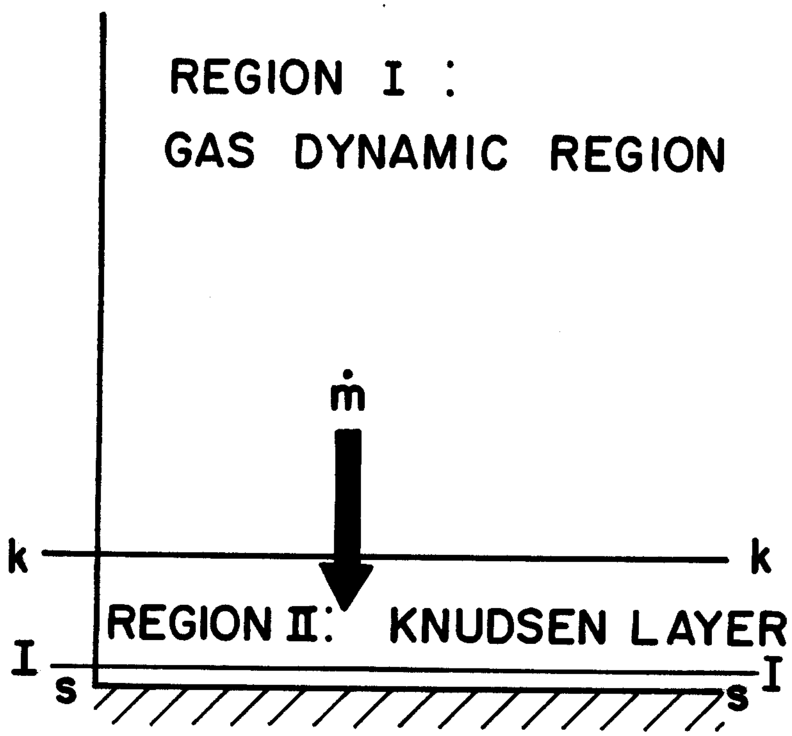

Fig. 2.12 Intensive condensation.

2. In k-k section, vapor has the Grad's 13-moment distribution

$$f_k = n_k\left(\frac{m}{2\pi T_k}\right) e^{-2}\left\{1 + \frac{1}{2}\frac{P_{11}}{P_k}(3\xi_1^2 - \underline{\xi}^2) + 2\frac{q_1\xi_1(\frac{2}{5}\underline{\xi}^2 - 1)}{P_k(2RT_e)^{1/2}}\right\}$$

$$P_k = n_k k T_k \qquad \xi = \frac{V}{(2RT_k)^{\xi}} \qquad V = v - U_k \qquad P_{ij} = P_{ij} - \delta_{ij}P \ .$$

3. The vapor emitted from the surface has a Maxwellian distribution

$$f = n_S(2\pi RT_S)^{3/2} \exp(-\ v^2/2RT_S) \qquad v_x > 0 \ .$$

4. Part of the flux from the k-k section will condense, so

$$f = Cf_k \qquad v_x < 0 \ .$$

The mass, momentum, and energy fluxes are evaluated for regions I and II and are matched at the k-k interface. For region II we get the equations:

$$1 - Cn_k\left(T_k^{1/2}\phi - \frac{U_k}{2}\psi + \frac{\phi}{2}\frac{P_{11}}{P_k}T_k^{1/2} - \frac{2}{5\pi}\frac{g_i U_k \phi}{P_k T_k^{1/2}}\right) = n_k U_k \tag{2.2}$$

$$\frac{1}{2} + Cn_k\left[\left(\frac{T_k}{2} + \frac{U_k^2}{4\pi} + \frac{P_{11}}{2P_k}T_k\right)\psi - \frac{U_k T_k^{1/2}}{2\pi}\phi - \frac{4q_1 T_k^{1/2}}{5\pi P_k}\phi\right] = n_k T_k + \frac{n_k U_k^2}{2\pi} + \frac{P_{11}}{P_k}n_k T_k \tag{2.3}$$

$$\begin{aligned}\frac{1}{2} - \frac{Cn_k}{2}\Big[T_k^{3/2}\left(1 + \frac{3}{4}\frac{P_{11}}{P_k}\right)\phi - \left(\frac{5}{8}T_k U_k + \frac{P_{11}}{4P_k}T_k U_k + \frac{U_k^3}{16\pi}\right)\psi + \frac{T_k^{1/2}U_k^2}{8\pi}\phi \\ - \frac{U_k T_k^{1/2} q_1}{5\pi P_k}\phi - \frac{T_k q_1}{P_k}\psi\Big] = \frac{5}{8}n_k T_k U_k + \frac{n_k U_k^3}{16\pi} + \frac{n_k U_k T_k}{4}\frac{P_{11}}{P_k} + n_k T_k\frac{q_1}{P_k} \ .\end{aligned} \tag{2.4}$$

For region I we get the equations:

$$U_k n_k = U_\infty n_\infty \tag{2.5}$$

$$n_k T_k + \frac{n_k U_k^2}{2\pi} + n_k T_k \frac{P_{11}}{P_k} = n_\infty T_\infty + \frac{n_\infty U_x^2}{2\pi} \tag{2.6}$$

$$\frac{5}{8} n_k T_k U_k + \frac{n_k U_k^3}{16\pi} + \frac{n_k U_k T_k}{4} \frac{P_{11}}{P_k} + n_k T_k \frac{q_1}{P_k} = \frac{5}{8} n_\infty T_\infty U_\infty + \frac{n_\infty U_\infty^3}{16\pi} \tag{2.7}$$

$$\frac{U_k}{U_\infty} \approx 1 - \frac{\frac{k}{k-1}(T_\beta - T_k) + \frac{U_\infty^2 - U_k^2}{4\pi}}{\frac{k}{k-1} T_\infty + \frac{U_\infty^2}{2\pi}} \qquad k = \frac{C_p}{C_v} \tag{2.8}$$

where we have introduced:

$$T_k = \frac{T_k}{T_S} \qquad n_k = \frac{n_k}{n_S} \qquad U_k = \frac{U_k}{(kT_S/2\pi m)^{1/2}} \qquad P_k \equiv \frac{P_k}{n_S k T_S}$$

$$P_{11} = \frac{P_{11}}{n_S k T_S} \qquad q_1 \equiv \frac{q_1}{4 n_S k T_S (kT_S/2\pi m)^{1/2}}$$

$$\phi = \exp\left(-\frac{U_k^2}{4\pi T_k}\right) \qquad \psi = 1 + \operatorname{erf}\left[-\frac{U_k}{2(\pi T_k)^{1/2}}\right] .$$

Using these one can specify n_∞, T_∞, n_S, T_S, and solve for T_k, U_k, C, n_k, P_{11}, q_1, and U_∞. The work that we found in the literature includes a linearized treatment of two phase condensation for a condensible gas in the presence of a noncondensible gas and nonlinear treatment of a single vapor phase intensive condensation phenomenon. We will try to extend this by studying the nonlinear two phase problem.

Following the intensive condensation method, we include the noncondensible gas effect. In addition to the assumptions presented above, we further assume that for noncondensible gas:

1. In region I, it has the equilibrium Maxwellian distribution. Since region I is collision dominant, the temperature of the noncondensible gas will be equal to the temperature of the condensible gas.
2. At the k-k section, we use Grad's 13-moment distribution

$$f_{2k} = n_{2k}\left(\frac{m_2}{2\pi T_{2k}}\right)e^{-\underline{\xi}^2}\left\{1 + \frac{1}{2}\frac{P_{211}}{P_{2k}}\left(3\xi_1^2 - \underline{\xi}^2\right) + \frac{2q_{21}\xi_1\left(\frac{2}{5}\underline{\xi}^2 - 1\right)}{P_{2k}(2R_2T_{2k})^{3/2}}\right\} .$$

3. In the immediate vicinity of the s-s plane, the noncondensible particles reflect with the same number density but different distribution function compared to the inward flux. The reflected particles have the distribution function corresponding to surface temperature T_S:

$$f_2 = C'f_{2k} \qquad v_x < 0$$

$$f_2 = C'n_{2k}\left(\frac{m_2}{2\pi T_S}\right) e^{-\underline{\xi}^2}\left\{1 + \frac{1}{2}\frac{P'_{211}}{P'_{2k}}\left(3\xi_1^2 - \underline{\xi}^2\right) + \frac{2q'_{21}\xi_1\left(\frac{2}{5}\underline{\xi}^2 - 1\right)}{P'_{2k}(2R_2T_S)^{3/2}}\right\} \qquad v_x > 0 .$$

4. The inward and reflected flux have the same diffusion velocity ($U_{2k} = U_{2S}$), but different temperature.
5. Assume the total pressure is constant

$$(n_{2k} + n_k)kT_k = (n_{2\infty} - n_\infty)kT_\infty .$$

With these assumptions, we can write the mass, momentum, energy flux equations in regions I and II for each component, and match them at surface k-k. We get 2 sets of equations similar to Eqs. (2.2) through (2.8) for condensible gas and noncondensible gas. After specifying the number density and temperature for the surface and at $x \to \infty$, we will try to solve the total 15 coupled nonlinear algebraic equations. Our future work will be to solve these 15 equations and understand the effects of noncondensible gas on the condensation rate and compare this to the linearized theory.

2.4 Density of Target Chamber Gas Needed for Beam Propagation

In the HIBALL report,(1) conservative estimates of the loss of beam due to change in the charge of beam ions through charge changing collisions predicted that no more than 4 x 10^{10} Pb atoms/cm^3 on average may be in the target chamber at the time of beam injection. As suggested earlier in this chapter, there may be some difficulties in reaching this density with a 5 Hz rep rate. We have recently re-examined this problem to determine if we have been overly conservative.

There have been recent measurements done at Lawrence Berkeley Laboratory(13) of charge-changing collision cross sections for heavy ions moving at the same speeds as the Bi^{2+} ions in HIBALL. Measured cross sections for Xe and Pb ions on N_2 are shown in Fig. 2.13 for many highly ionized states of the beam ions and for a few values of $\beta = v/c$. A comparision has been given in Fig. 2.13 for the measured election loss cross sections (which are relevant to HIBALL-I) and those calculated with the major theoretical methods. The work in HIBALL-I was based on some calculations by Y-K. Kim(14) which used the Born Approximation Sum Rule (BASR) method. From Fig. 2.13, one can see that BASR is higher than the measured values by at least a factor of four.

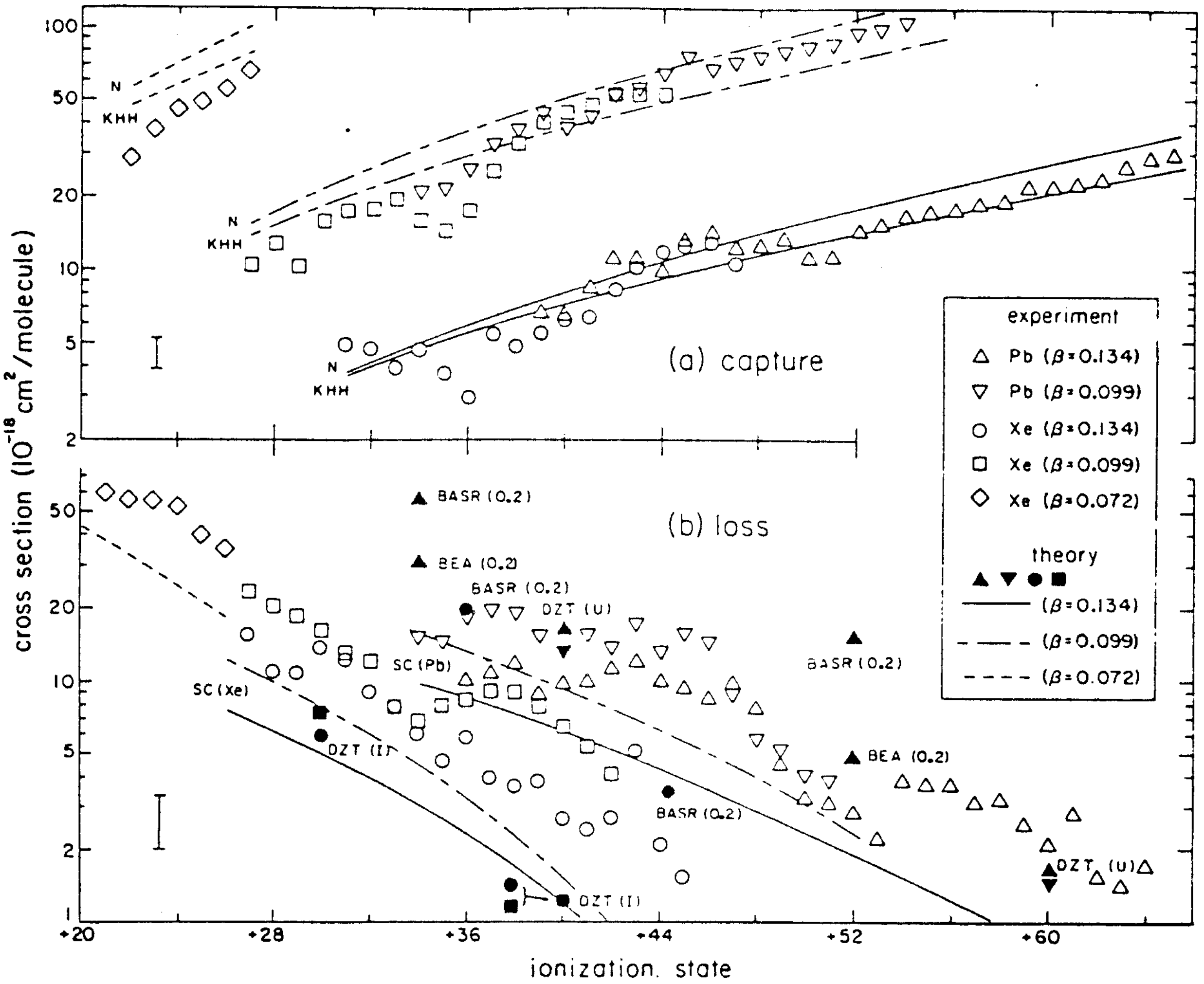

Fig. 2.13 (a) Capture and (b) single-electron-loss cross sections in N_2 as a function of the ionization state for Pb and Xe ions. Experiment is shown as open symbols, theory with the corresponding closed symbols and with broken and solid lines.

The loss of target ions using the BASR calculated cross sections for a 8×10^{10} Pb atoms/cm^3 vapor density was estimated to be 2.5% in HIBALL-I. If we claim from the measured values that the cross section for charge changing collisions is always less than a fourth of the BASR value, we find that 3.2×10^{11} Pb atoms/cm^3 is a better estimate of the density which will lead to a 2.5% beam loss. Figure 2.14 shows that if we require that the cavity vapor density is 3.2×10^{11} for beam propagation, the recovery time decreases from 0.31 sec to 0.27 sec. If we allow that 5.0% of the beam is lost, we can have 6×10^{11} Pb atoms/cm^3 in the target chamber and the rep rate could be 4 Hz.

Another thing that can be done to increase the rep rate is to increase the beam particle energy. Alonso's(13) semi-classical model predicts that the charge changing cross section scales as β^{-2}. So if our estimate of the cross section is correct, we can have a 5 Hz rep rate with 5.0% beam loss by increasing the beam energy by a factor of 10, which would allow us to increase the cavity vapor density to 6×10^{12} cm^{-3}. This would obviously be a major change in the driver design and in the target design so maybe it would be better to stay with the 4 Hz rep rate.

The experiments that the above discussion is based on have certain limitations that we should be careful to note. The most important is that the target atoms for these experiments are nitrogen while they are lead in HIBALL-I. It is not known for certain if the discrepancies in the BASR can be carried over to Pb target ions. Also the experiments were done for highly ionized beam ions while HIBALL-I has Bi^{2+} ions and we cannot say with certainty that the results for the BASR would still hold.

If we cannot increase the beam energy and if we cannot increase the rep rate above 4 Hz for each cavity by any other means, we might consider prepa-

Fig. 2.14

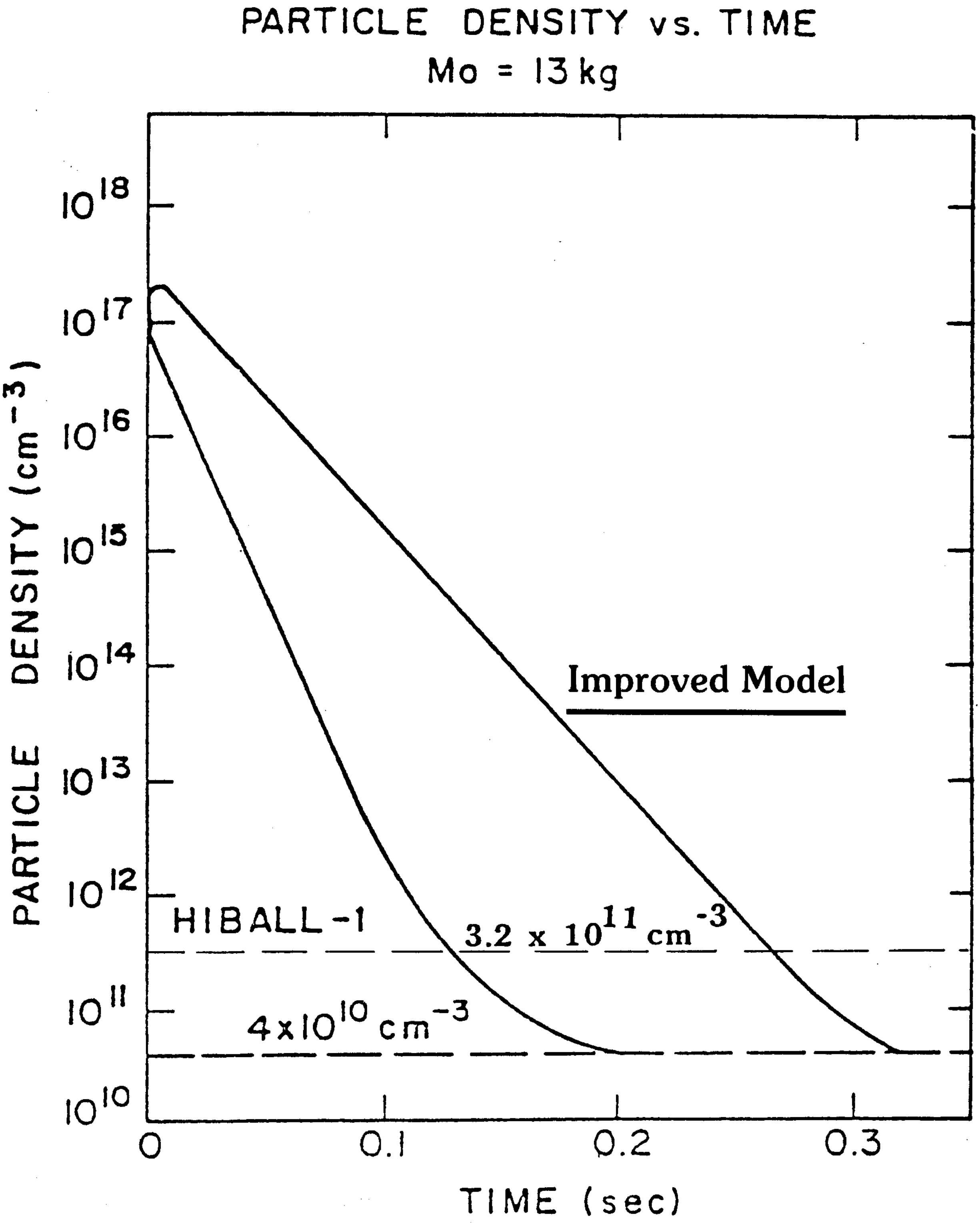
PARTICLE DENSITY vs. TIME
Mo = 13 kg
PARTICLE DENSITY (cm^{-3})
10^{18}
10^{17}
10^{16}
10^{15}
10^{14}
10^{13}
10^{12}
10^{11}
10^{10}
Improved Model
HIBALL-1
3.2×10^{11} cm^{-3}
4×10^{10} cm^{-3}
0
0.1
0.2
0.3
TIME (sec)

ration mechanisms other than ballistic focusing. There is the possiblity of propagating beams through much higher densities in pre-formed channels or in the self-pinched mode. We will not address these further here but will make the point that if we cannot get the rep rate up in an acceptable manner for ballistic focusing, these options do exist.

References for Chapter 2

1. B. Badger et al., "HIBALL - A Conceptual Heavy Ion Beam Driven Fusion Reactor Study," KfK-3202/1, UWFDM-450 (December 1981).
2. G.A. Moses and R.R. Peterson, "FIRE - A Computer Code to Simulate Cavity Gas Response to Inertial Confinement Target Explosions," University of Wisconsin Fusion Engineering Program Report UWFDM-336 (January 1980).
3. L.C. Pong, D.K. Sze, R.R. Peterson and G.A. Moses, "Progress on Modelling $Pb_{83}Li_{17}$ Recondensation on INPORT Units," Fusion Power Associates Report FPA-82-5 (July 1982).
4. R.R. Peterson et al., "Gas Dynamics in Liquid Metal ICF Reactor First Wall Surfaces," University of Wisconsin Fusion Engineering Program Report UWFDM-443 (October 1981).
5. D. Mikalas, Stellar Atmospheres, W.H. Freeman and Co., San Francisco, 1978.
6. D. Mosher, Naval Research Laboratory Memorandum Report 2563 (March 1979).
7. Ya B. Zel'dovich and Yu P. Raizer, Physics of Shock Waves and High Temperature Hydrodynamic Phenomena, Chap. III, Academic Press, New York, 1967.
8. Newstein, Solimene and Hammer, "Kinetic Theory Treatment of Metal Evaporation Front."
9. Takeo Soga, "Kinetic Analysis of Evaporation and Condensation in a Vapor-Gas Mixture," Phys. Fluids 21, 1978 (1982).
10. Tadashi Matsushita, "Evaporation and Condensation in a Vapor-Gas Mixture," Rarefied Gas Dynamics 51, Part II, p. 1213.
11. Y.P. Pao, Phys. Fluids 14, 1340 (1971).
12. Labuntsov and Kryukov, "Analysis of Intensive Evaporation and Condensation," Int. J. Heat Mass Transfer 22, 989-1002 (1979).

13. J.A. Alonso and H. Gould, "Charge-Changing Cross Sections for Pb and Xe Ions at Velocities Up To 4 x 10^9 cm/sec," Phys. Rev. A 26, 1134 (1982).

14. G.H. Gillespie, K.T. Cheng and Y.K. Kim, Argonne National Laboratory Report ANL-79-41, p.175.

3. Heating of Target and Sabot During Injections

The cryogenic fusion target must be injected into the target chamber in such a way that the cryogenic D-T fuel in the target remains solid. As in the past,(1) we require that the inside boundary of the target fuel remains colder than the sublimation temperature of 11.3 K and that no part of the fuel becomes hotter than the melting temperature of 19.7 K. In this section we describe improvements that have been made to the target heating calculations presented in the HIBALL-I report.

The target that we have always considered in our target heating considerations is shown in Fig. 3.1. This is a cryogenic target which has a layer of D-T fuel frozen onto the inside surface of a solid hollow spherical shell. In order for the target to be driven to ignition by the ion beam, this fuel must remain solid until the pressure caused by the absorption of the ion beam in the outer layers implodes it to ignition.

The baseline scheme for injection of the target is shown schematically in Fig. 3.2. This method was described in detail in the HIBALL-I report and uses a pneumatic gun to accelerate the target while it is encased in a sabot assembly. The sabot protects the target from frictional heat due to contact with the gun barrel and separates from the target after the assembly leaves the gun barrel but before it reaches the target chamber. Since the publication of the HIBALL-I report, alternative methods of target injection have been investigated but for the work presented in this section we will only consider the baseline pneumatic scenario.

There are two periods of time during which we have considered heating of the target fuel: while the target and sabot assembly are in the gun barrel and while the target is in the target chamber. The latter was considered in

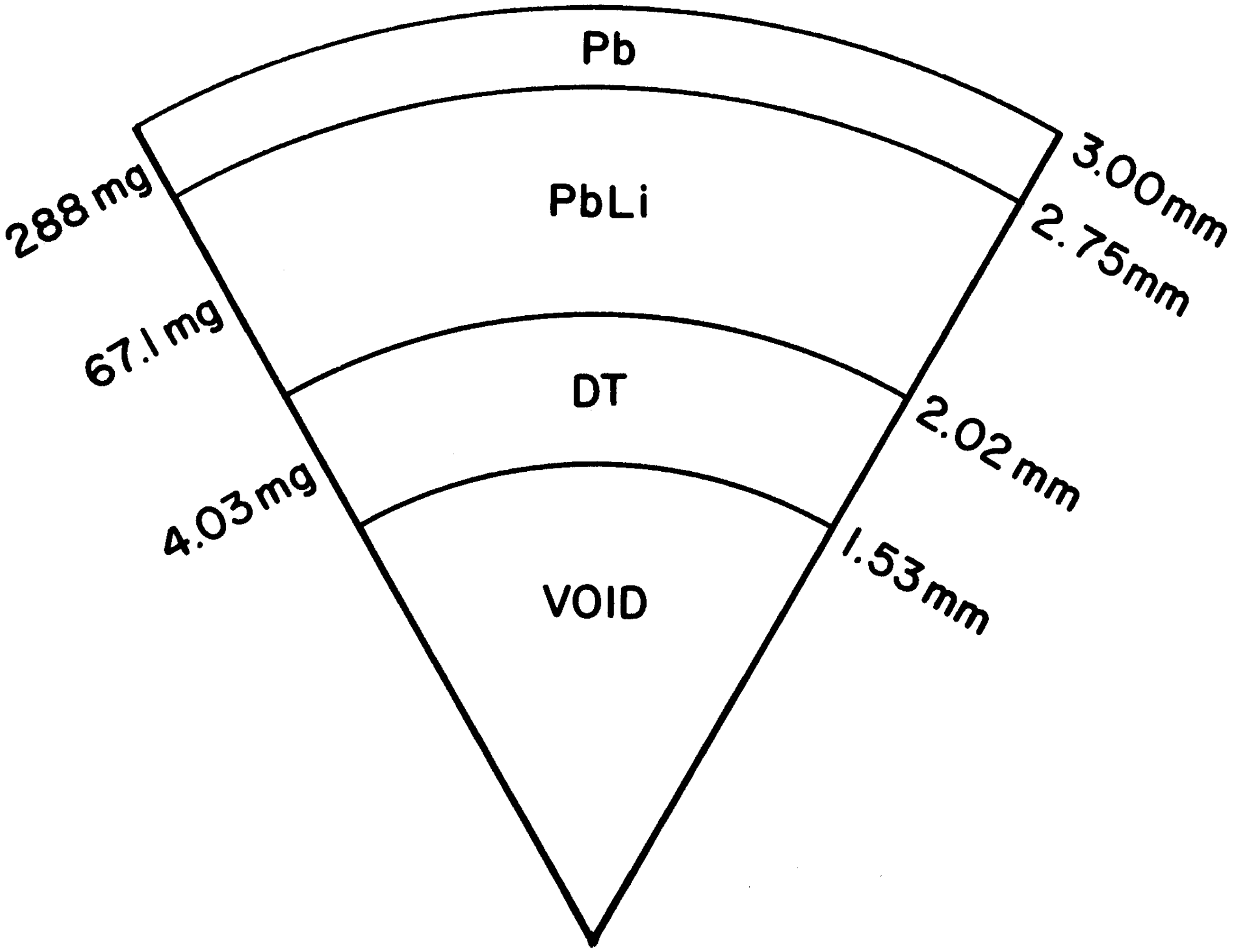

Fig. 3.1 HIBALL cryogenic target.

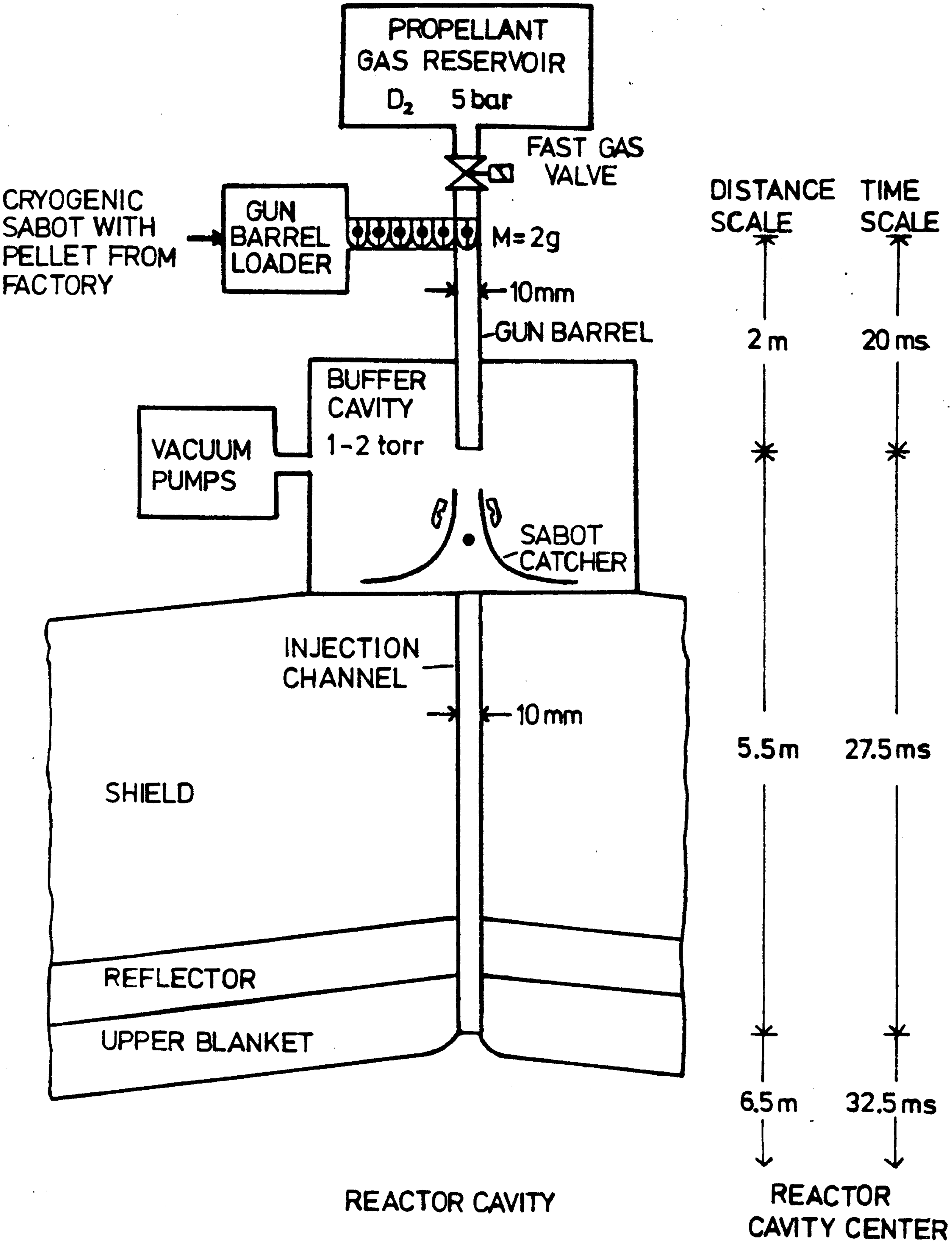

Fig. 3-2 Scheme of HIBALL-I pneumatic injection system and design paramter values. Pellet velocity = 200 m/s.

the HIBALL-I report and temperature profiles in target were obtained for various periods of time in the cavity. These are shown in Fig. 3.3 and were obtained through the use of the temperature diffusion computer code PELLET, which simulates the time dependent heating of a material with temperature-dependent thermal properties under the influence of a time-dependent surface heat load. A surface heat load, due to 500°C blackbody radiation in the target chamber, of 2.02 W/cm^2 has been assumed for the target in Fig. 3.1. It is seen in Fig. 3.3 that the maximum temperature in the fuel at 32.5 ms after the target enters the target chamber, the time at which a target moving at 200 m/s would intersect the ion beams, is slightly less than 14 K. This occurs at the DT-PbLi interface and is still below the melting temperature of DT so that a slight lowering of the injection velocity will not lead to melting of the fuel. Futhermore, the temperature at the inside boundary of the fuel is below the sublimation temperature. This calculation was based on an assumption that the target enters the cavity with a uniform temperature of 4 K. Since the fuel is only slightly below the melting and sublimation conditions, if the injection velocity is to be kept at 200 m/s the target must not be heated to any significant degree while it is in the gun barrel.

A sabot has been designed at Interatom(2) which is shown in Fig. 3.4 with a pellet inside. The sabot is heated by friction with the gun barrel at annular contact areas A_1 and A_2. Heat is conducted to the target through contact areas A_1, A_2 and A_3. The sabot material is taken to be Teflon and the gun barrel material is steel, giving a coefficient of friction of 0.0513. The frictional heat load on the surface of the sabot is

$$\dot{q}_f = f\ A\ P\ \nabla$$

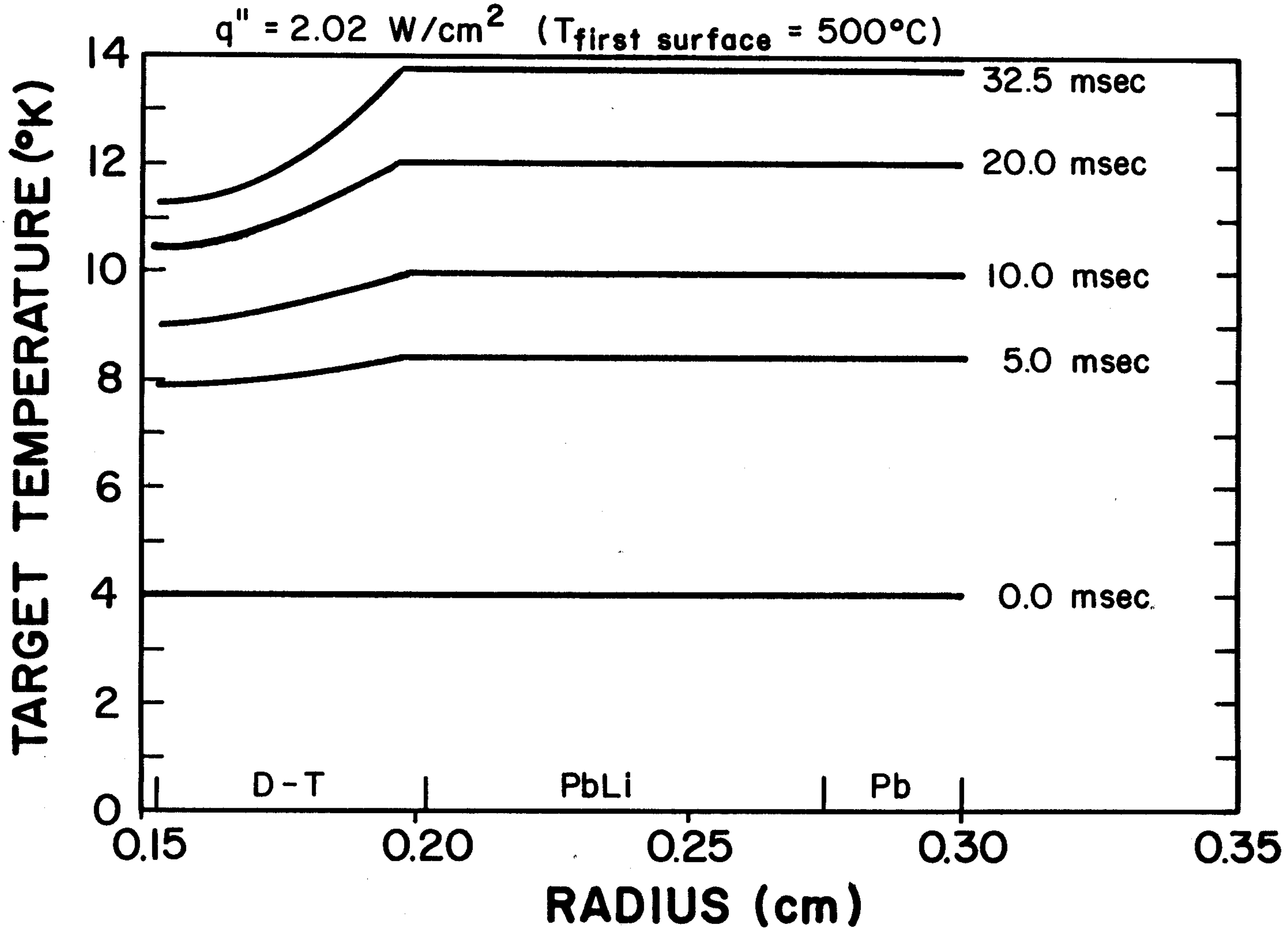

Fig. 3-3 Target temperature profiles due to heat in target chamber.

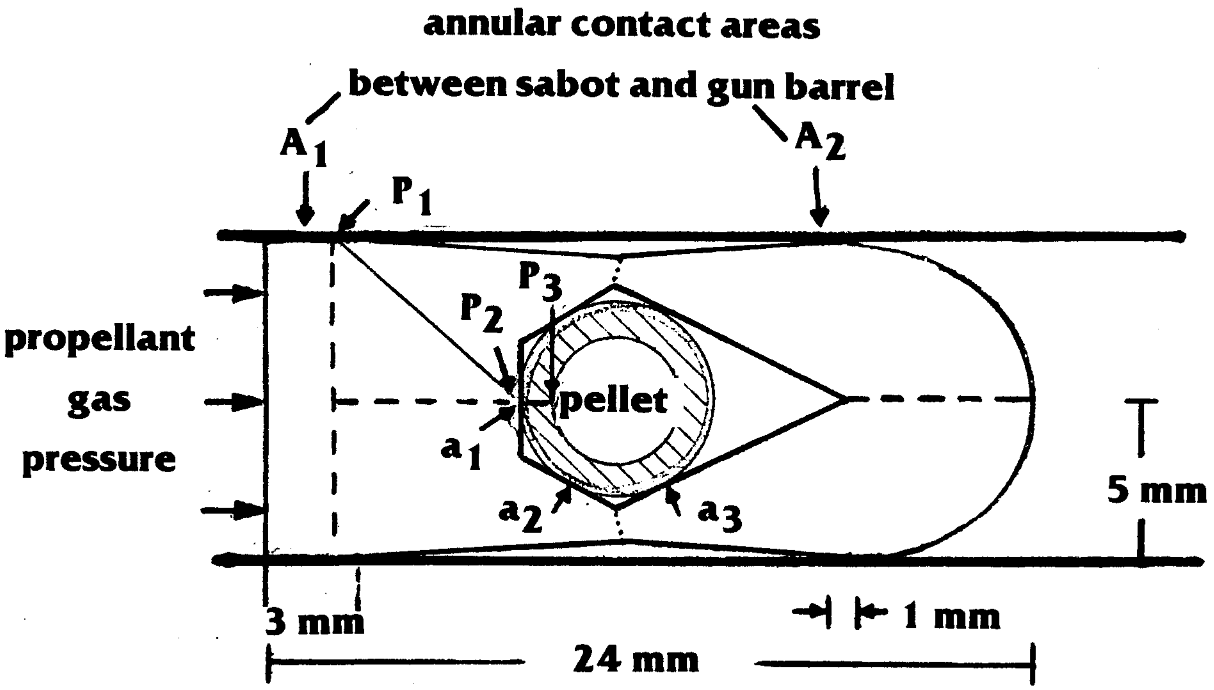

Fig. 3.4 HIBALL target and sabot.

where f is the coefficient of friction, A is the contact area, P is the force per unit area exerted on the sabot by the gun barrel and $\bar{V}$ is the average velocity of the sabot in the gun barrel. With $\bar{V} = 100$ m/s and $P = 10^5$ N/m^2, the frictional heat load is 51.3 W/cm^2.

The greatest conduction of heat from the contact between the sabot and gun barrel and the target fuel will occur along the path shown as $P_1P_2P_3$ in Fig. 3.4. Point P_1 is at the forward-most edge of contact area A_1, which is the largest contact area at 0.78 cm^2. Point P_2 is at contact area a_1 between the target and the sabot which is 0.03 cm^2 and is both much larger and closer to A_1 than either A_2 or A_3. Point P_3 is at the inside edge of the solid D-T fuel, at the point closest to P_2.

We have used the PELLET code to calculate the heating of the target by frictional heat from contact area A_1. PELLET is a one-dimensional computer code which we have applied to heat transfer along the line $P_1P_2P_3$. Heat transfer is actually a three-dimensional problem in the sabot assembly so that our one-dimensional analysis will overestimate the heat transferred to the target. Because the one-dimensional heat transfer is an overestimate and because we are considering the path of greatest heat transfer, we feel that our method is conservative.

The temperature profiles predicted by PELLET are shown in Fig. 3.5. Profiles are shown at the time that the acceleration starts and 20 ms later, when the target leaves the gun barrel. Notice that the target is not heated at all and that most of the sabot is not heated either. Thus the target enters the cavity at a uniform temperature of 4 K, where we have still neglected heating during storage due to tritium decay and heating while the target is moving from the gun barrel to the target chamber.

Fig. 3.5 Target and sabot temperature profiles due to heating in gun barrel.

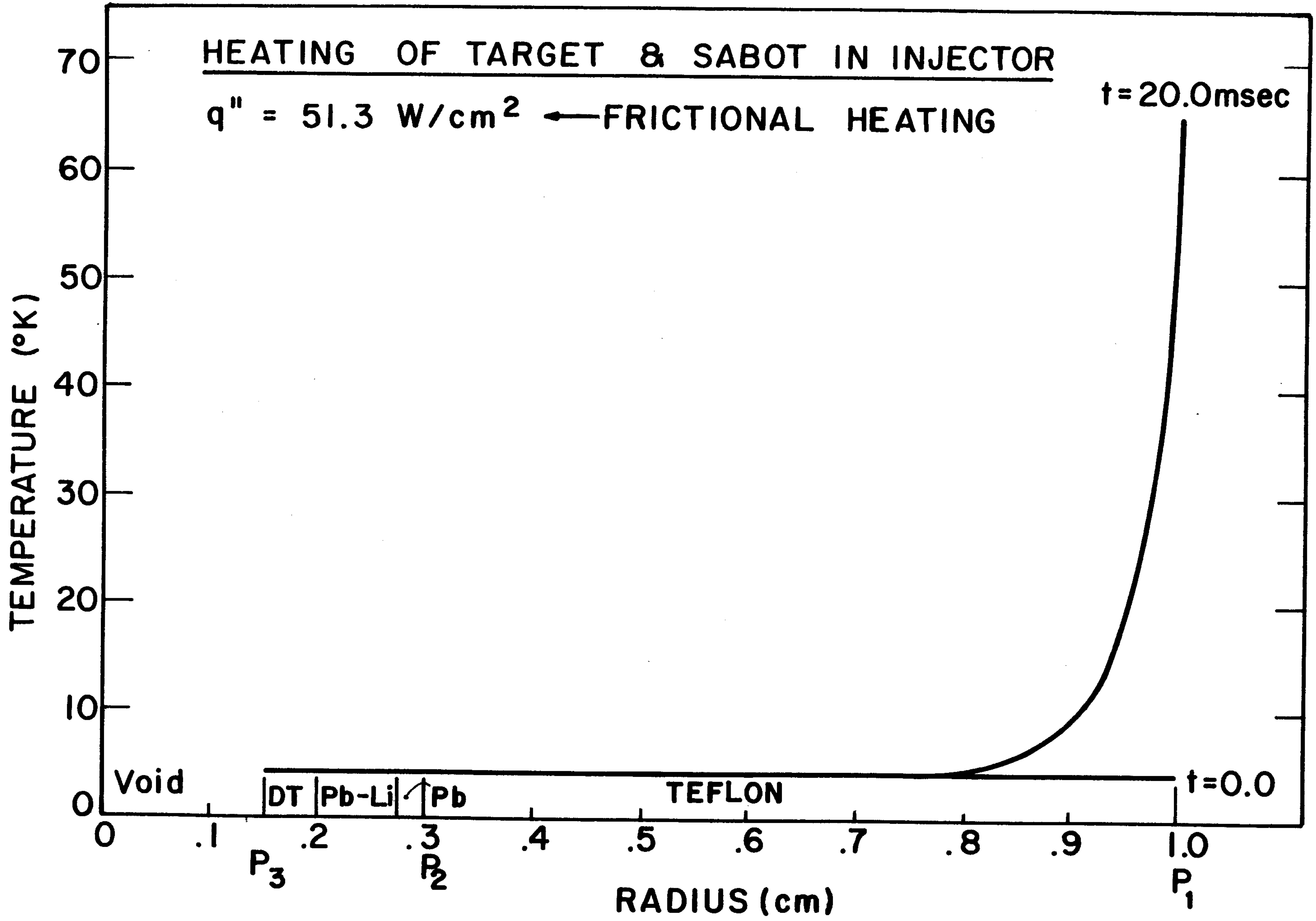

Thus we have shown that the heating due to friction during acceleration and due to blackbody radiation in the target chamber of HIBALL do not damage the target.

References for Chapter 3

1. B. Badger et al., "HIBALL - A Conceptual Heavy Ion Beam Driven Fusion Reactor Study," University of Wisconsin Fusion Engineering Program Report UWFDM-450, Kernforschungszentrum Karlsruhe Report KfK-3202 (1981).
2. R. Kreutz, private communication.

4. Cavity Upper Blanket

4.1 Overall Design Description

The design of the upper part of the cylindrical cavity had to conform to several basic requirements which are:

1. The provision of a wetted surface similar to the INPORT units.
2. A design which gives easy access to the inside of the cavity.
3. Incorporation of removable modules for maintenance.

To this end, the upper part of the cavity was divided into 30 identical modules which is equal to the number of modules in the radial blanket. The modules are wedge shaped as shown in Fig. 4.1, 680 cm long and 140 cm wide at the rear. The radial and the upper modules coincide vertically, such that when an upper module is removed, the radial module immediately below it can be taken out through the empty space thus provided.

In the original design, the module consisted of a skeletal frame made of rigidized SiC over which was stretched a porous braid of SiC cloth. The coolant came in at the back of the module, flowed radially toward the center of the cavity through the upper channels shown in Fig. 4.1, then passed through holes into the lower part of the module and flowed radially outward. Some of the coolant permeated the porous SiC cloth and provided the needed wetted surface. The bulk of the coolant, however, remained within the module finally exiting it at the back and merging with coolant flowing through the rear tubes of the radial modules.

At the time the original HIBALL report was issued, the mechanical properties of SiC fibers were still not well characterized. The design called for a single lobe of material to be stretched across the bottom of the module. Since then we have determined that a much lower design stress must be used for

Fig. 4.1

DESIGN OF AN UPPER BLANKET SEGMENT

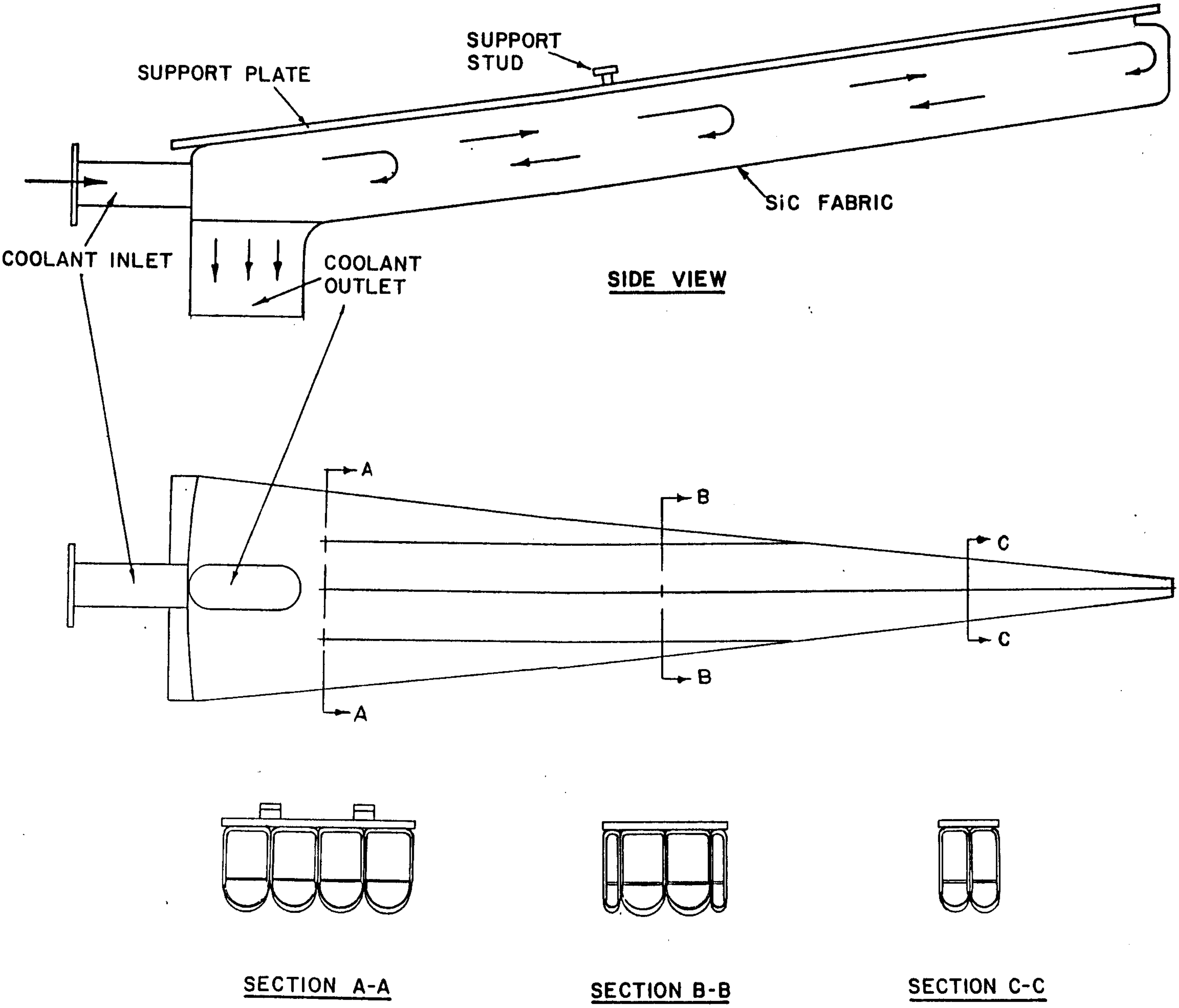

the SiC fibers. Accordingly, the modules have been redesigned to permit a multilobe construction which reduces the span of the stretched fabric making the radius of curvature of the lobe much smaller, thus substantially reducing the principal stresses.

In the present design, each module is made up of four skeletal frames of rigidized SiC, each covered with a porous braid of SiC cloth. The maximum radius of curvature of each lobe at the rear is 16.3 cm. Each segment is bolted to a single support plate which in turn is used to attach the module to the roof structure. The skeletal frames have thin perforated semicircular lower membranes which serve two functions: they prevent the SiC fabric from excessive deflection and also provide damping of shock waves transmitted through the coolant. The four segments terminate in a single rear exit which funnels the coolant into the back tubes of the radial module. Cross sections at several locations in Fig. 4.1 show how the segments are assembled into a module.

Construction of the modules seems to be straightforward considering the complex shape of aerospace components manufactured at the present time. The skeletal frames will be made of braided SiC fibers which are stretched over collapsible frames and rigidized with SiC. Any place which calls for the braided flexible cloth to be attached to the rigidized frame, the two are effectively glued together with SiC. Alternatively, they can be clamped and glued. What has to be kept in mind, is that a certain amount of coolant leakage at these joints is tolerable provided it does not drip profusely into the cavity. Since these joints are in the outer periphery of the cavity, any leakage there would not drip any place where it could be intercepted by beam ions.

Support of the upper modules is difficult for several reasons. The 50 cm column of LiPb in the modules is quite heavy; furthermore, the maintenance scheme assumes that the upper reflector/shield can be rotated during routine replacement of cavity components. We believe that the original support method outlined in the HIBALL report is consistent with these requirements and should be retained. In this method, the inner end of the support plate to which the blanket modules are attached rests on a hub which can be rotated with respect to the reflector/shield assembly. Thus, when the reflector/shield assembly is rotated for maintenance, the hub remains stationary. The rear end of the support plate rests on a ledge which is an extension of the cylindrical reflector. Along the length of the module, the support plate is attached to the upper reflector at several appropriate radial locations. Figure 4.1 shows only one support stud; however, there can be as many as needed. These support studs are mechanically latched to the upper reflector during reactor operation, or whenever the coolant load on the upper blanket is present. During reactor maintenance, when the coolant is drained out of the whole cavity, the mechanical latches are uncoupled, such that the upper reflector/shield assembly can be rotated, while the upper blanket modules remain stationary. For additional details of reactor maintenance, the reader is referred to Chapter IX of the initial HIBALL report. Table 4.1 gives the parameters of the upper blanket modules.

4.2 Stress Analysis of Upper Blanket Covering

The upper blanket modules are composed of a rigid structural frame and a covering of woven SiC fabric. The original design for the fabric configuration was a partial conical shell with an internal pressure which varied linearly from 2 psi (0.0138 MPa) at the vertex to 20.18 psi (0.139 MPa) at the

Table 4.1 Upper Blanket Design Parameters

Module Structural Material	SiC
Number of Modules	30
Length of Module (cm)	680
Length of Porous Cloth (cm)	610
Maximum Width of Module (cm)	140
Width of Porous Cloth Termination (cm)	130
Maximum Radius of Lobe (cm)	16.3
Number of Lobes/Module	4
Effective Thickness of Porous Fabric (cm)	0.1
Maximum Pressure on Fabric (MPa)	0.139
Maximum Hoop Stress on Fabric (MPa)	22.7

base as indicated in Fig. 4.2. The inclined length along the frame is 610 cm and the horizontal base width (chord) is 130 cm.

The most highly stressed area is at the bottom center (base) of the conical shall. The circumferential and axial stresses are denoted by σ_ϕ and σ_x, the former being the larger of these two principal values. The magnitude of σ_ϕ is strongly influenced by the local radius of curvature at the point under examination. For example a relatively shallow conical section with a drop of 25 cm has a radius of curvature of 97.1 cm and corresponding stress of 135.1 MPa. While the geometry is acceptable, the stress is too high for this application. The stress can be lowered by reducing the radius of curvature with the best configuration being semicircular. However, since the drop equals the radius of curvature for semicircular lobes (65 cm), this does not

Fig. 4.2

UPPER BLANKET MODULE SiC SHELL

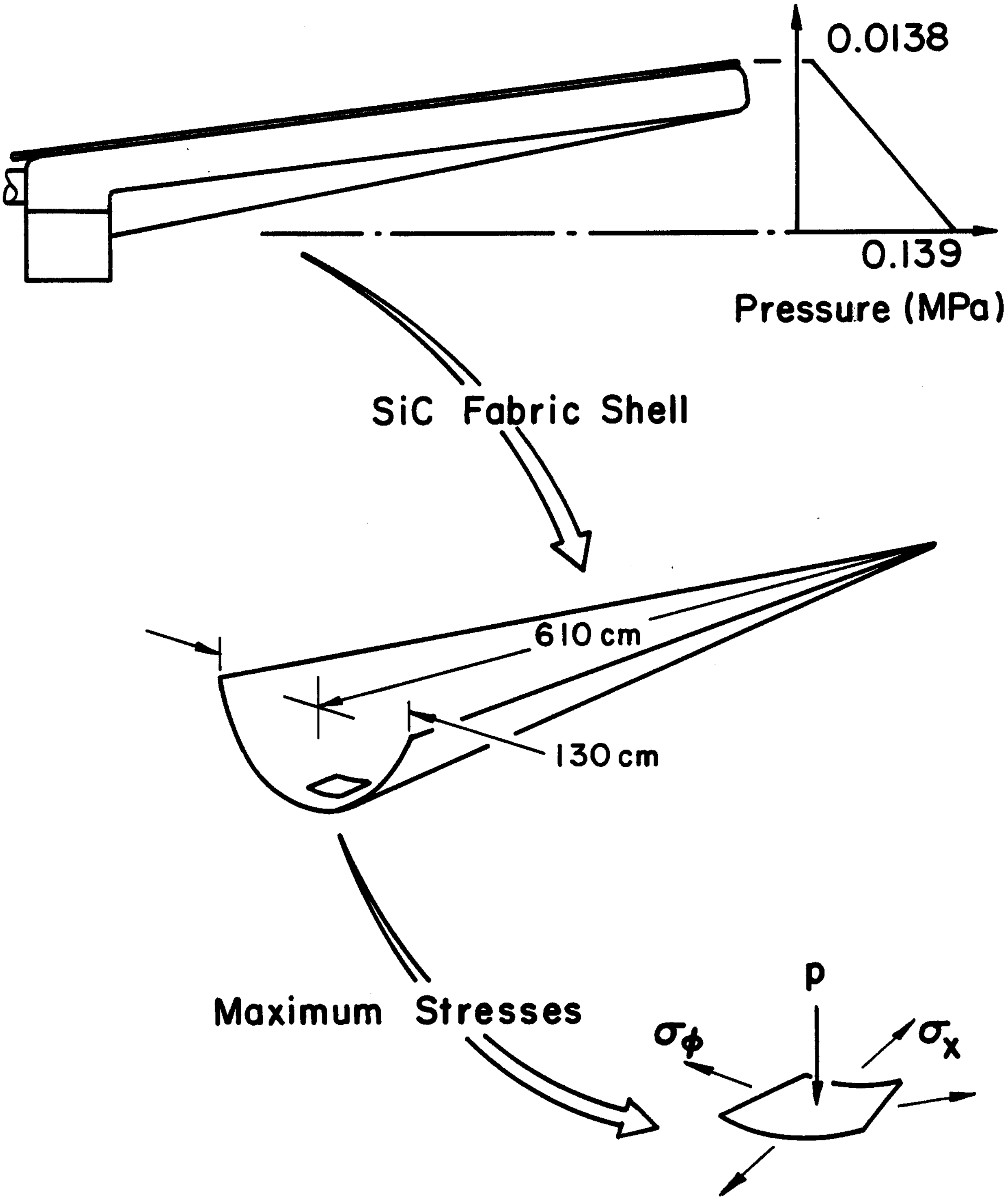

Table 4.2. Stresses In Multilobed Upper Blanket Modules

No. of Lobes - N		1	2	3	4
Radius	cm	65.0	32.5	21.7	16.3
	in	25.59	12.80	8.53	6.40
Stress	MPa	91.0	45.3	30.2	22.7
	ksi	13.20	6.57	4.37	3.29

produce a practical design. A compromise to limit both stresses and the drop distance is a multilobe design. Results are shown in Fig. 4.3 for a fixed chord (130 cm), pressure (0.139 MPa) and material thickness (1 mm). The numerical values are listed in Table 4.2. From this data the four lobe configuration was selected and a more detailed mechanical design is based upon this geometric configuration.

4.3 Maintenance and Response of Li-Pb Coating

The structure on the top of the HIBALL cavity has to be protected from the fireball by a layer of $Li_{17}Pb_{83}$. This LiPb has to be leaking through the main coolant channel to the inside surface. It is important to calculate the maximum protection layer without having the LiPb form droplets. The seepage rate corresponds to the required thickness needed so that the tightness of the SiC structure could be determined.

The formation of the droplets is determined by the balance of the gravitational force and adhesive force as shown in Fig. 4.4. Assuming a half

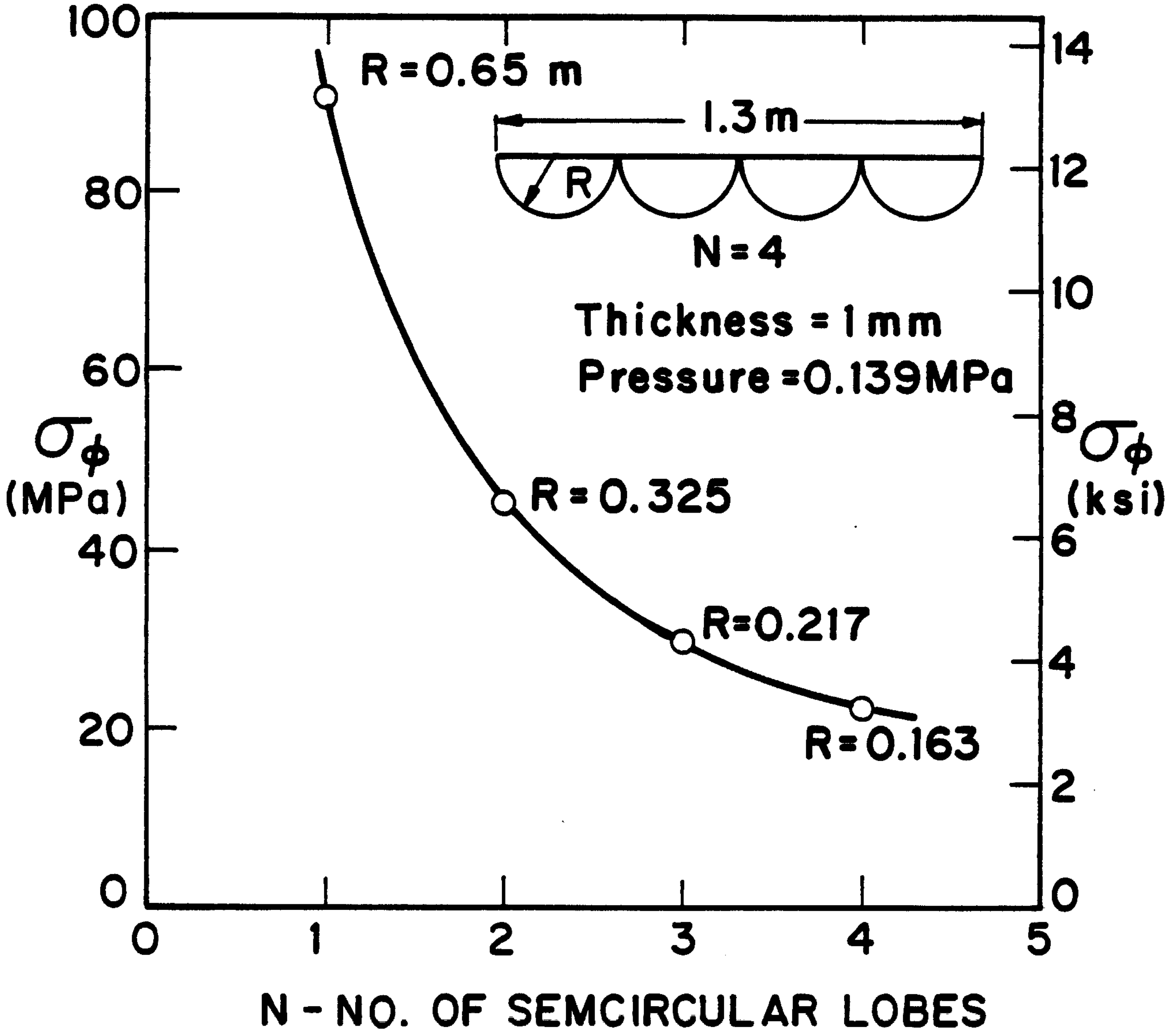

Fig. 4.3

MAXIMUM STRESS IN MULTILOBED UPPER BLANKET MODULE

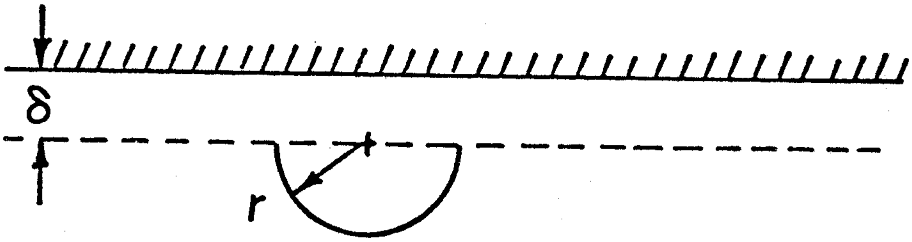

Fig. 4.4 Schematic configuration of drop formation.

droplet of radius r is formed on the LiPb film, the forces are

$$\text{Gravitation force } F_g = \frac{4}{6}\pi r^3 \rho g \qquad (4.1)$$

$$\text{Adhesive force } F_a = \Gamma\, 2\pi r \qquad (4.2)$$

where Γ is the surface tension. For Pb, Γ = 450 dynes/cm.

If

$$F_g = F_a \qquad (4.3)$$

$$r = 0.38 \text{ cm.}$$

If $\delta < r$, a half drop of radius r cannot form, therefore $\delta = 0.1 \sim 0.3$ cm.

The allowable seepage rate can be calculated by reference to Fig. 4.5. The acceleration force of the film is

$$F_{ac} = \rho g x \sin\theta \ . \qquad (4.4)$$

The viscous force is

$$F_v = -\mu \frac{dv}{dx} \ . \qquad (4.5)$$

By equating $F_v = F_{ac}$, the velocity profile can be calculated as

$$V(x) = \frac{\rho g \delta^2}{2\mu}\left[1 - \left(\frac{x}{\delta}\right)^2\right] \sin\theta \ . \qquad (4.6)$$

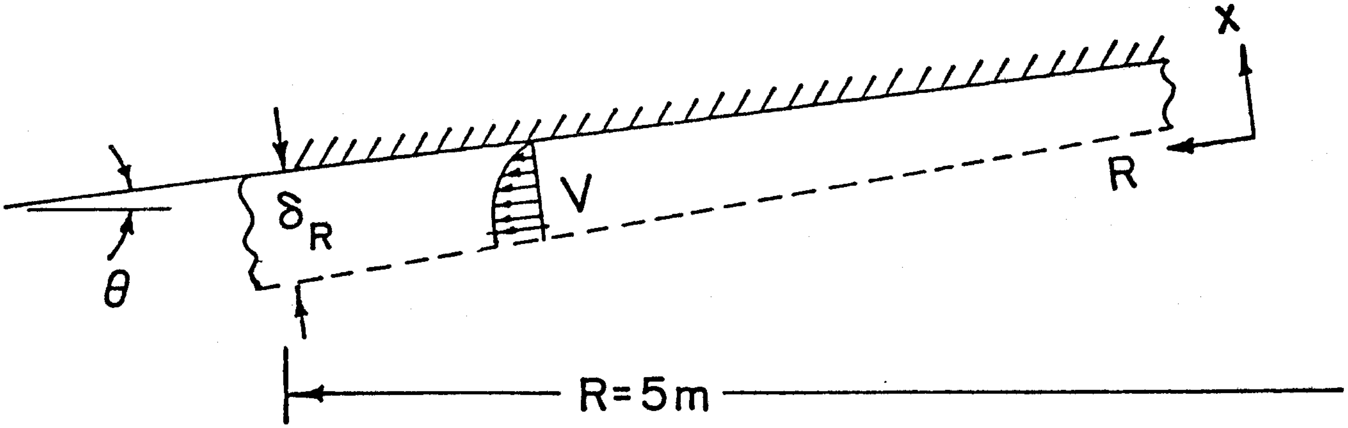

Fig. 4.5 Force balance of LiPb film.

The volumetric flow rate at any radius r is

$$Q(r) = \rho g \delta^3 \sin\theta \, (2\pi r)/(3\mu) \ .$$

The volumetric LiPb flow rate and required seepage rate at R = 500 cm, with $\theta = 7°$ and $\mu = 0.017$ g/s-cm, are tabulated in Table 4.3.

Table 4.3. Volumetric Flow Rate and Seepage Rate of the LiPb Film

δ_R (cm)	Q (cm^3/s)	Q/A ($cm^3/s\text{-}cm^2$)
0.1	0.7×10^5	0.09
0.2	5.6×10^5	0.71
0.3	18.9×10^5	2.4

5. Mechanical Testing of Silicon Carbide

5.1 Static Tensile Tests of Fibers

The purpose of these tests is to determine the tensile strength and elastic modulus and to qualitatively identify failure characteristics. Tests were carried out on cords (tow) composed of 500 untwisted continuous SiC fibers. A scanning electron microscope (SEM) photograph of fibers which have failed in tension is shown in Fig. 5.1. The horizontal bar scale corresponds to 100 μ. In Fig. 5.2 the magnification is increased with the bar scale equivalent to 10 μ. The mean diameter can be obtained by scanning along the filaments and was found to be 12.6 μ. The uniformity of the individual fibers is apparent in these photographs.

Tensile loads were applied with a MTS T5002 universal testing machine equipped with a 100 N load cell and a Hewlett-Packard recorder (Fig. 5.3); a single tow under load appears in Fig. 5.4. The grips were specifically designed for fibers and stranded materials. Cords are wound around stationary cylinders and the ends are clamped at the top and bottom. Figure 5.5 shows the test fixtures more clearly and a typical failure pattern. The "brooming" characteristic of the failure is evident in Fig. 5.6 in which half of a specimen appears on a grid background (20 x 20/inch). Such a result might lead one to expect predominately sequential fiber failure and a definite knee on the stress-strain diagrams. However, this is not the case and the dominant failure mode is simultaneous fracture of the majority of fibers as implied by Fig. 5.7. This diagram is representative of the tests performed.

Quantitative results for ten specimens are listed in Table 5.1. In general the consistency was very good. The average tensile strength and modulus were 1.346 GPa and 90.04 GPa, respectively. These values are approximate-

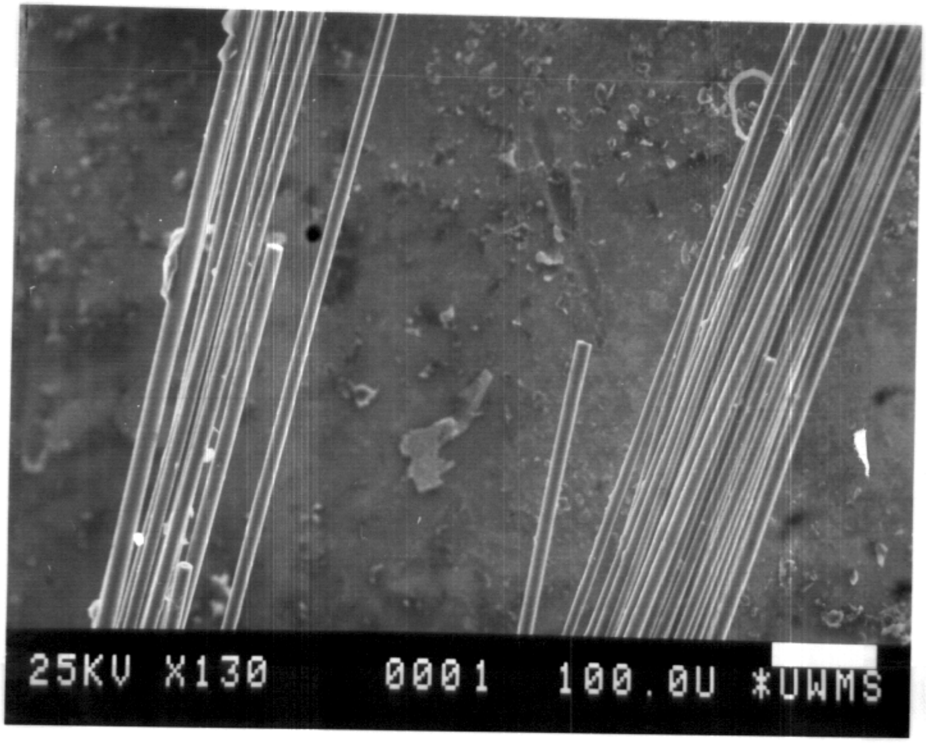

Fig. 5.1 Static tensile fracture of SiC fibers.
Bar scale = 100 microns.

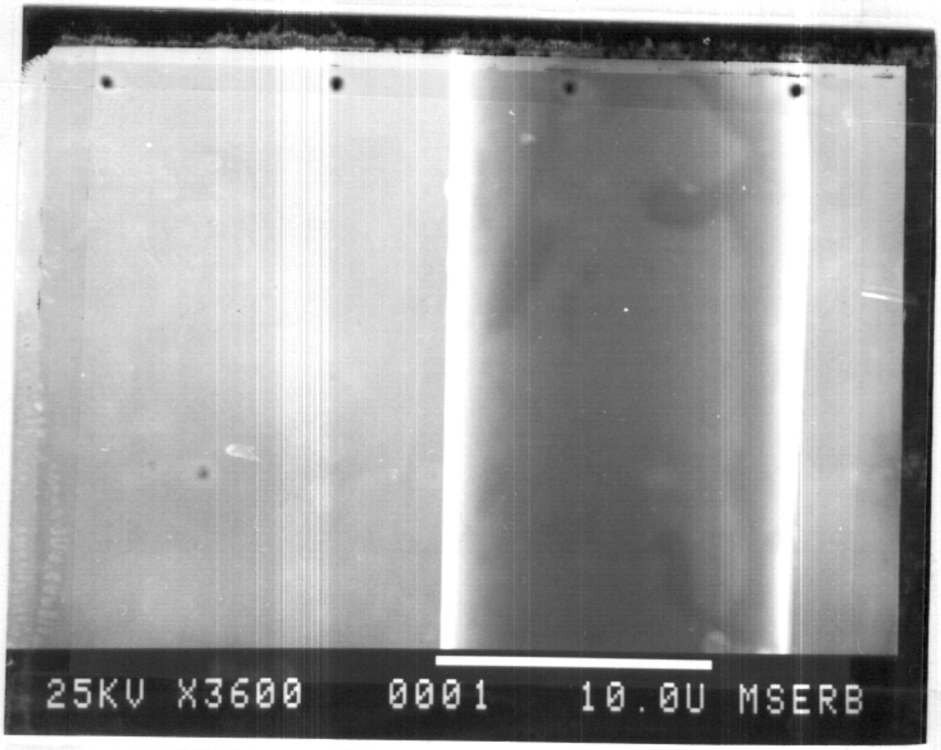

Fig. 5.2 SEM photograph of single fiber.
Bar scale = 100 microns.

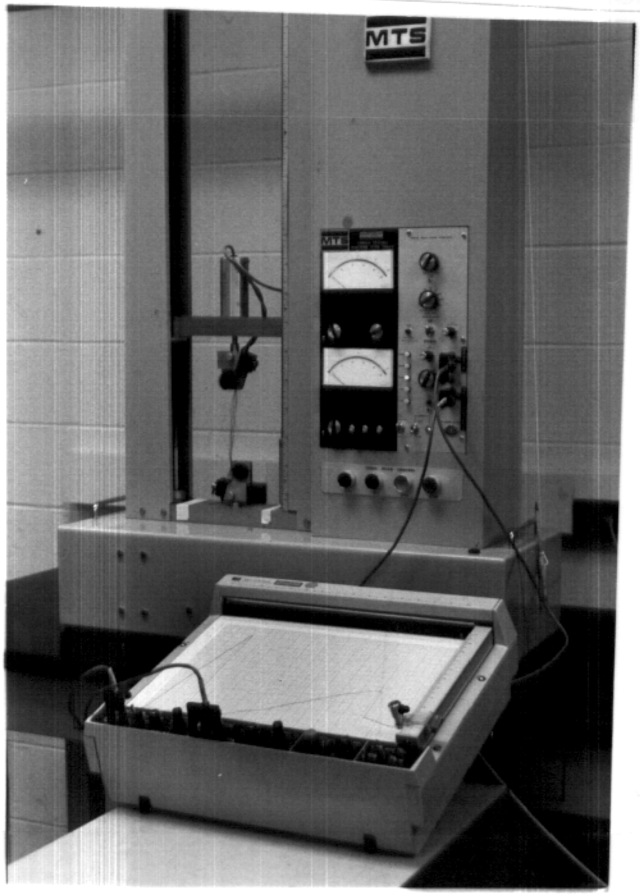

Fig. 5.3 Universal testing machine, load cell and recorder.

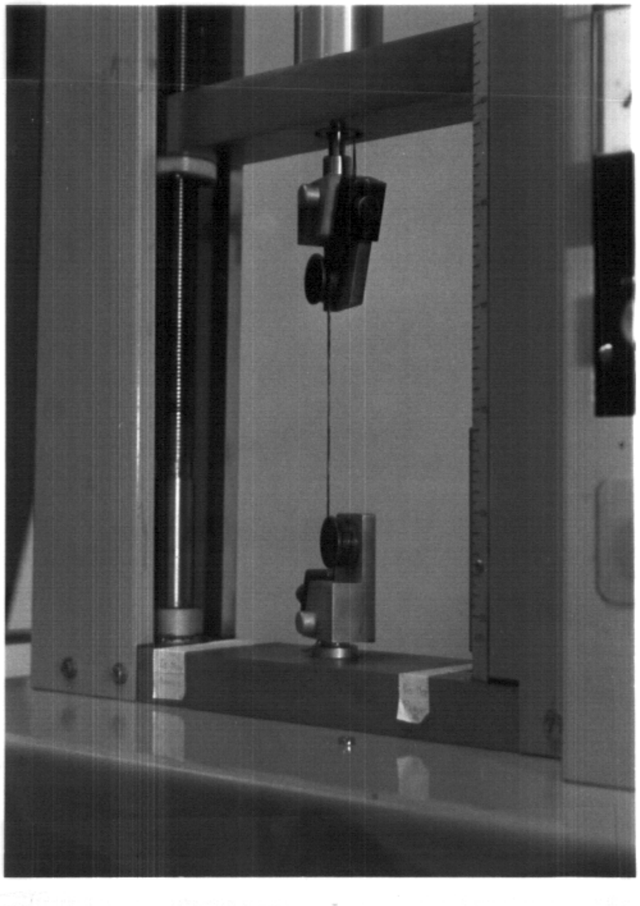

Fig. 5.4 SiC in fiber testing grips.

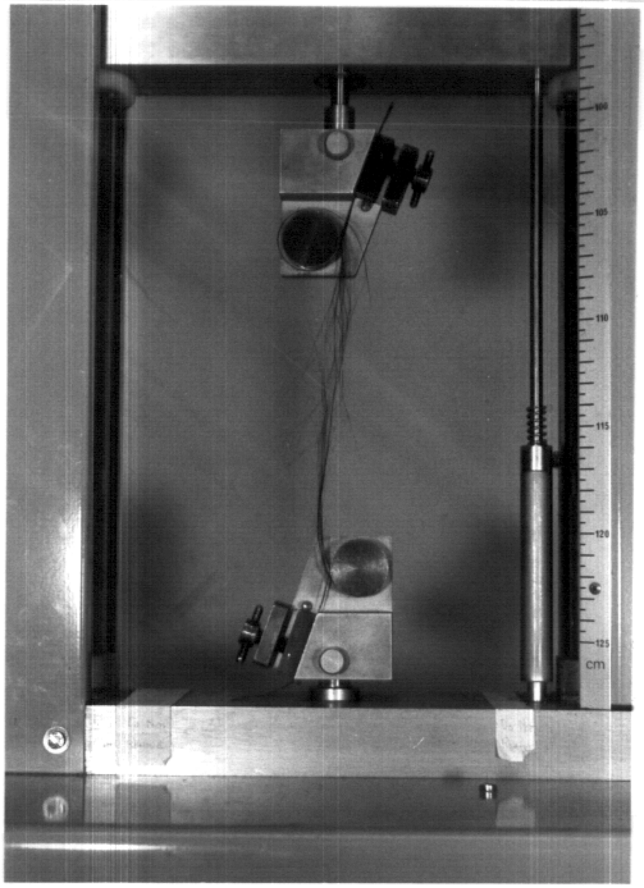

Fig. 5.5 Tensile failure of SiC fibers.

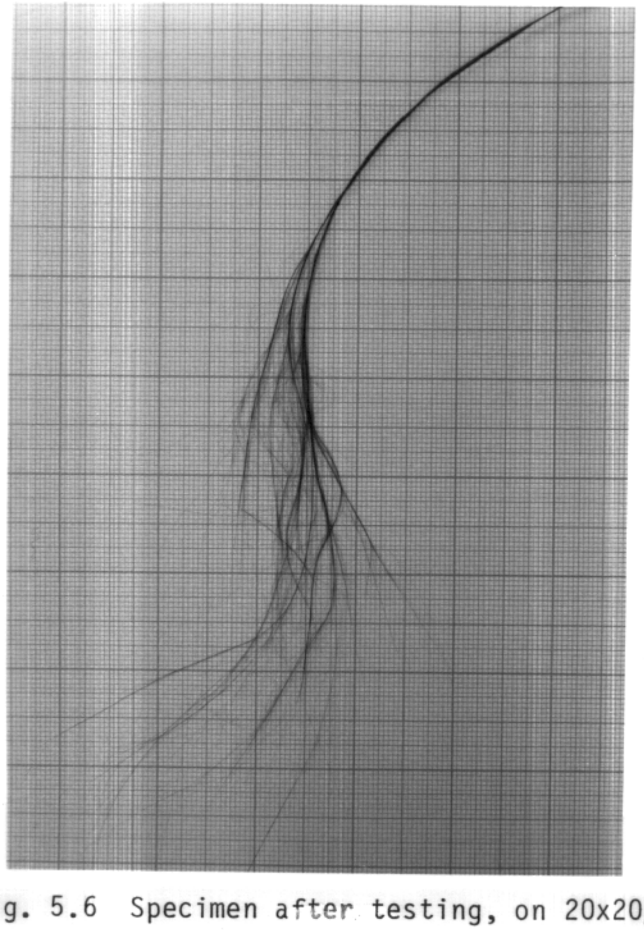

Fig. 5.6 Specimen after testing, on 20x20/inch grid.

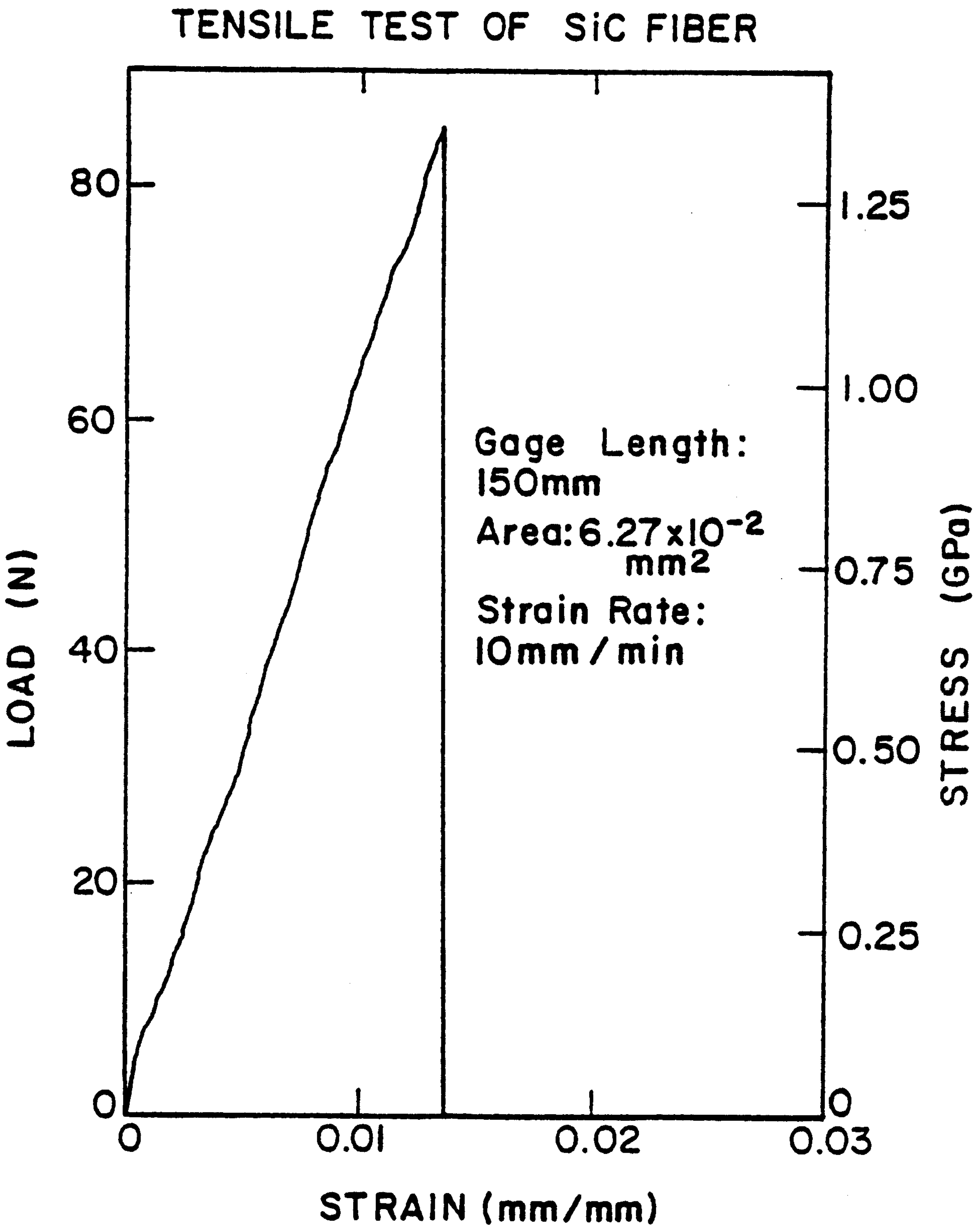

Fig. 5.7 Tensile test of SiC fiber.

Table 5.1. Silicon Carbide Cord Tension Test Data

U.W. Madison 1982

Filament Diameter - 12.6 μ
Number of Filaments - 500
Cross Section Area - 6.27×10^{-2} mm^2
Specimen Length - 150 mm
Strain Rate - 10 mm/min

Specimen Number	Maximum Load (N)	Failure Stress (GPa)	Elastic Modulus (GPa)
1	86.0	1.371	86.57
2	84.5	1.347	88.80
3	85.0	1.354	94.41
4	83.3	1.328	88.19
5	88.0	1.403	94.16
6	75.8	1.208	93.18
7	89.5	1.427	93.18
8	96.5	1.538	81.91
9	84.3	1.344	89.26
10	71.2	1.135	90.69
Avg.	84.4 N (19.0 lb)	1.346 GPa (195.2 ksi)	90.04 GPa (13.06×10^6 psi)

ly one half of those reported for single fibers, a result attributable to unequal load sharing by fibers in the tow.

5.2 Fatigue Tests

Since the proposed application of the INPORT units involves repetitive loading, it is important to initiate tests to provide data for an understanding of dynamic mechanical behavior. For the first tests, the range of loads was limited but a sufficient number of specimens was used to generate a fatigue life curve. In addition, considerable experience was gained which will be important for future work.

The same apparatus was used for static and dynamic testing. The gauge length for all samples was 15 cm and the maximum load frequency was 0.25 Hz. The mean stress was 50% of the fracture stress (1.35 GPa) while alternating stress amplitudes were 10, 20, 30 and 40% of the static fracture stress. Six tests were carried out at each of these four alternating amplitudes.

Results are shown in Fig. 5.8 in which the average number of cycles to failure is plotted at the various stress levels. A least squares fit to the data produced a fatigue life curve

$$\sigma_a/\sigma_f = -0.113 \log N_F + 0.49 \ .$$

Here σ_a, σ_f and N_F denote the alternating stress amplitude, fracture stress and cycles to failure, respectively. Note that the single cycle test extrapolation is very close to the 50% value. It is also noteworthy that the plot is similar to results for fatigue of many metals and alloys. SEM photography of the fractured ends is shown in Figs. 5.9 and 5.10. Static tensile failure is characterized by a clean sharp break, typical of a brittle material. However, it can be seen that cyclic failure produces permanent deformation more characteristic of ductile materials. Inclined slip surfaces and the corresponding platelets are evident at the ends of the fibers.

A number of additional observations should be noted. Dynamic stress-strain curves for loading and unloading are not coincident. A loop is

Fig. 5.8

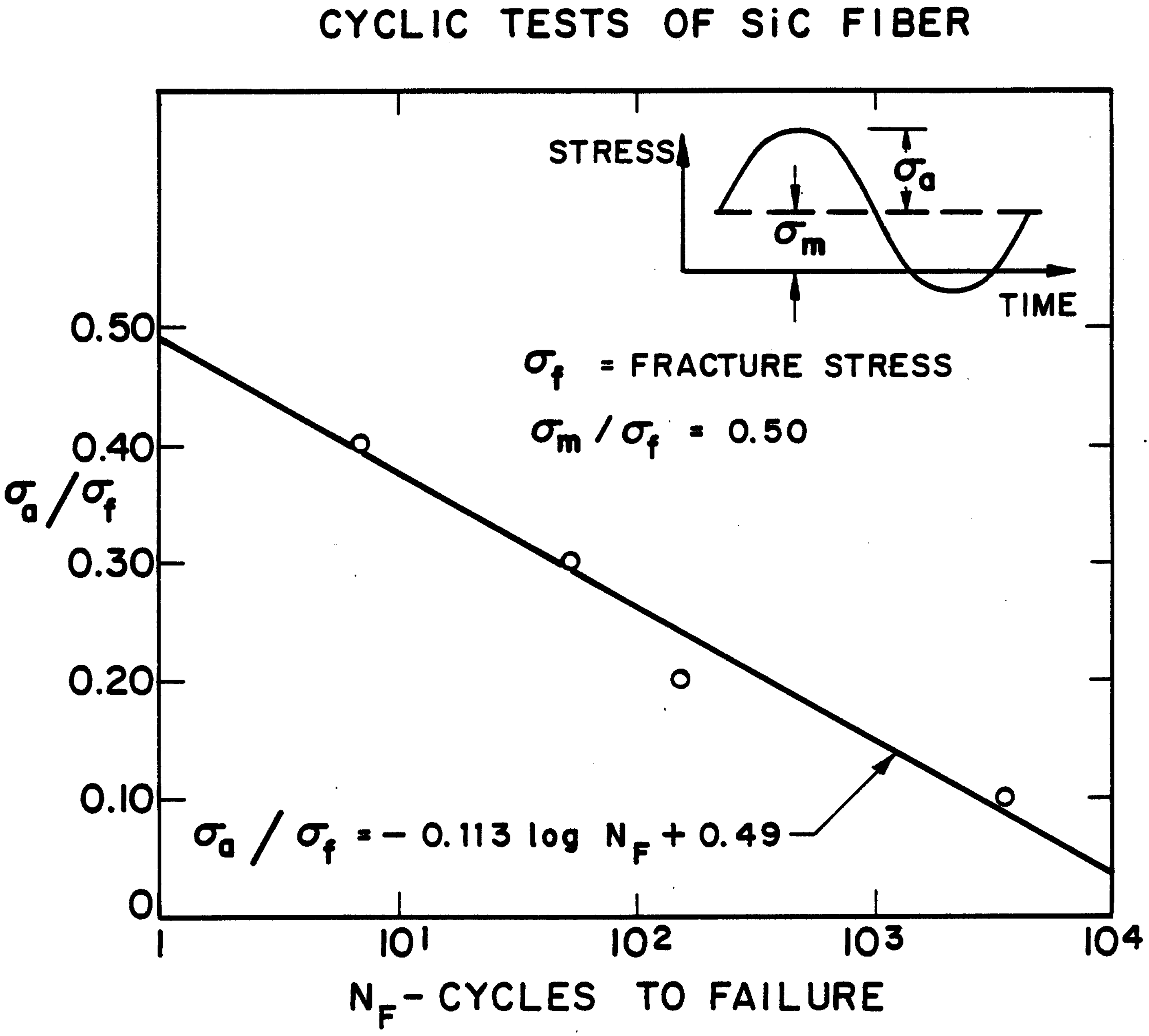
CYCLIC TESTS OF SiC FIBER
STRESS
σ_a
σ_m
TIME
σ_f = FRACTURE STRESS
σ_m / σ_f = 0.50
σ_a / σ_f
0.50
0.40
0.30
0.20
0.10
0
$\sigma_a / \sigma_f = -0.113 \log N_F + 0.49$
1
10^1
10^2
10^3
10^4
N_F - CYCLES TO FAILURE

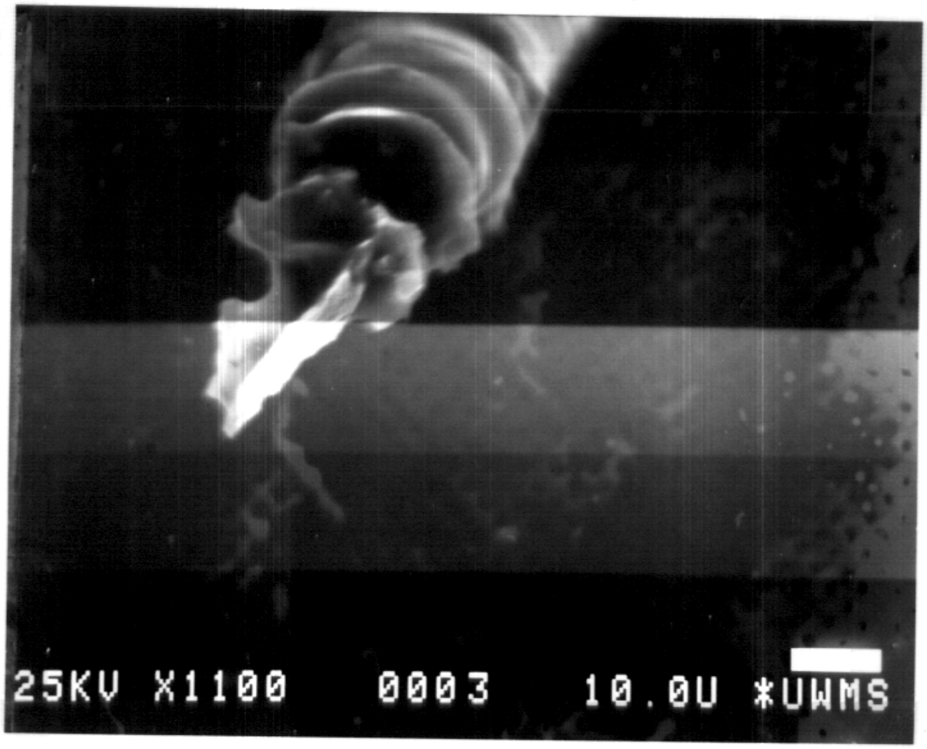

Fig. 5.9 Fatigue fracture of single SiC fiber.

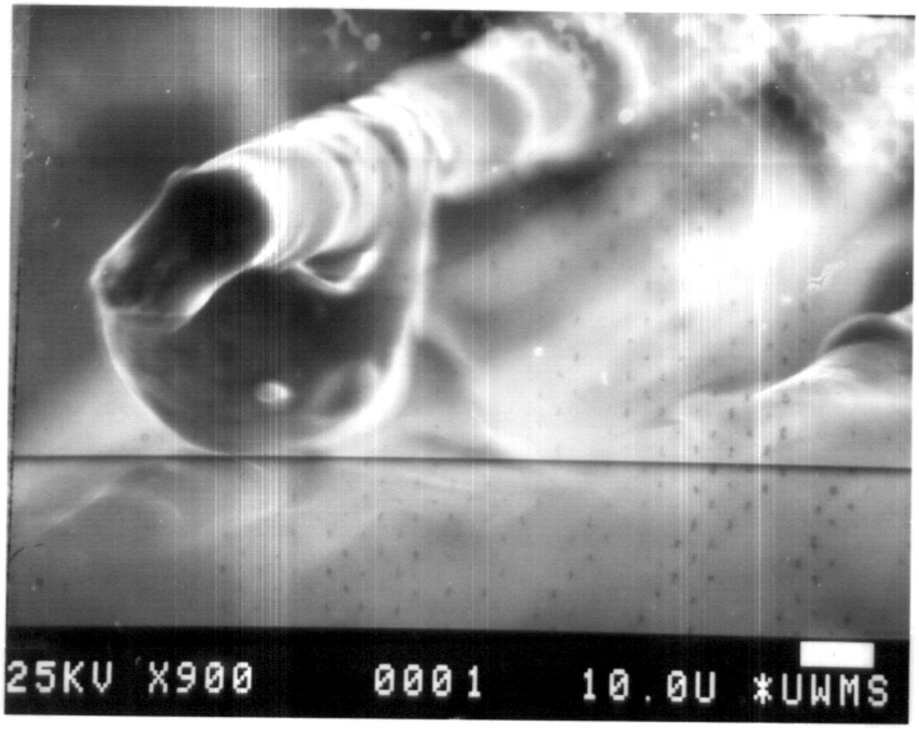

Fig. 5.10 Fatigue fracture of fiber with SEM conductant.

developed in which the unloading curve is the lower of the two. The loop width decreases with increasing number of cycles. The process is generally associated with material energy absorption. Also, after many cycles an apparent cross-section reduction was observed. Fibers were simply closer together near midspan than either end. One speculation is that this may have been caused by one or more fibers that had encircled the bundle and essentially produced a knot which migrated to this region. Rather large apparent strains (e.g., 1%) were also recorded prior to failure. This may include effects of fiber realignment, small movement within grips and permanent slip near the fractured ends.

5.3 McDonnell-Douglas INPORT Tests

McDonnell-Douglas Corp., St. Louis, fabricated seven woven SiC tubes and tested six to failure in static tension. Three were made with axial tows. Two tubes with axials and two without received a SiC chemical vapor deposition (CVD) treatment. Tests were carried out at two temperatures: 350 and 550°C.

Results are summarized in Table 5.2. It can be seen that the CVD process substantially increases the tensile strength. This improves load sharing of the fibers but produces a brittle tube. Axial cords in untreated tubes fail prematurely since they're carrying the total tensile load. Without axial members, the elongation is excessive for untreated INPORTs. The tested units are shown in Fig. 5.11 with identification numbers corresponding to Table 5.2.

5.4 Conclusions and Recommendations

Procedures developed for static testing of SiC tow have produced consistent results. The tensile strength of fiber bundles is very high although less than that reported for individual fibers. Fatigue tests have been performed at only one mean stress level. Additional data should be developed for other

Fig. 5.11 INPORT units after static tensile testing.

Table 5.2. INPORT Tension Data

McDonnell-Douglas Corporation

Braided Tube Thickness	0.38 mm
SiC/CVD Tube Thickness	0.69
Mandrel Diameter	2.86 cm
Braiding angle	30°
No. of Braiding Tows	48
No. of Filaments/Tow	500
No. of Axial Tows	0/9

Failure Load - lb. (psi) [I.D. No.]

Test Temperature	Axial Tows	Untreated Inports	CVD INPORTS
350° C	0	---	155 [2] (1624)
350°C	9	---	249 [6] (2607)
550°C	0	75 [3] (786)	130 [1] (1362)
550°C	9	37 [7] (Failure of Axials)	248 [5] (2599)

mean stresses particularly at low levels to seek an endurance limit. The effect of CVD on individual tow in fatigue and simple tension should be identified. In addition, fatigue tests should be carried out at elevated temperatures.

The data generated with INPORT tests has been limited. Second generation designs should be developed incorporating a greater number of axial cords with provisions to insure load sharing. An attempt should be made to include advantages of both CVD treated and untreated INPORTs. For all applications a larger number of filaments per tow is recommended (e.g., 2000).

Analytical studies are important as well for dynamic response calculations, the identification of potential instabilities and nonplanar motion.

6. Beam Line Neutronics Analysis

6.1 Introduction

Fusion reactors are required to accommodate a variety of penetrations. The purpose and size of these penetrations vary depending on the reactor type.(1-3) However, in all cases proper shielding is required to protect vital components in the penetration from excessive radiation damage caused by the streaming radiation. A major penetration in a heavy ion beam fusion reactor is the ion beam line penetration. A large number of these penetrations (~ 20) is required to provide uniform illumination of the target.

The HIBALL-II reactor utilizes twenty 10 GeV Bi^+ ion beams to bring the target to ignition. Each beam port is rectangular in shape with a height of 0.216 m and a width of 0.166 m at the reactor cavity wall of radius 7 m. The twenty beam ports occupy 0.12% of the 4π solid angle at the target. A number of magnets are arranged along the beam line to focus the ion beam to a spot 7 mm in diameter at the target. Adequate shielding is required to reduce the radiation effects in the magnets below the design limits. In a previous work(4) it was shown that radiation effects in the magnets can be reduced significantly by tapering the inner surface of shield along the direct line-of-sight of source neutrons in both the quadrupole and drift sections leading to a number of neutron dumps along the beam penetration. A similar shield configuration is used to protect the final focusing magnets of HIBALL-II.

The final focusing system in HIBALL-II utilizes two deflection sectors resulting in two vertical bends in the beam line penetration. These bends result in significant reduction in the amount of radiation streaming to the periodic transport system as compared to HIBALL-I where a straight beam line was used.

In this section the neutronic analysis for the beam line penetration is presented. Radiation effects in the magnets are determined and neutron streaming along the penetration is assessed. Neutron spectra in different shield zones along the beam line are determined. These are useful in calculating the dose outside the final focusing system.

6.2 Magnet and Shield Configuration

The final focusing system in HIBALL-II focuses the Bi^+ ion beam from the periodic transport line onto the target. The system consists of six quadrupole lenses and two deflection magnetic sectors. Two deflecting sector fields are required to obtain achromatic focusing. Figure 6.1 shows the variation of the vertical and horizontal width of the beam along the optic axis as it is transported from the periodic transport line to the target. The position of the six quadrupole lenses and two magnetic sectors is also shown. The square line represents the relative focusing strength (field gradient) of the quadrupoles. The deflection radii and angles for the two deflecting sectors are also indicated. A description of the overall geometry is given in Table 6.1. The lengths of the different magnetic elements as well as the field free drift sections are given. The aperture radii as well as the pole tip field strengths and field gradients are also included. Only quadrupoles with magnetic flux densities below 2 tesla are used such that iron dominated quadrupole lenses can be used. Quadrupole Q6 is driven with normal coils while all other quadrupoles are driven with superconducting coils.

The inner dimensions of the magnet shield along the beam lines were determined using the beam envelopes shown in Fig. 6.1. A minimum clearance of 1 cm is maintained between the shield and the ion beam. In order to minimize the radiation effects in the magnets the inner surface of the shield is

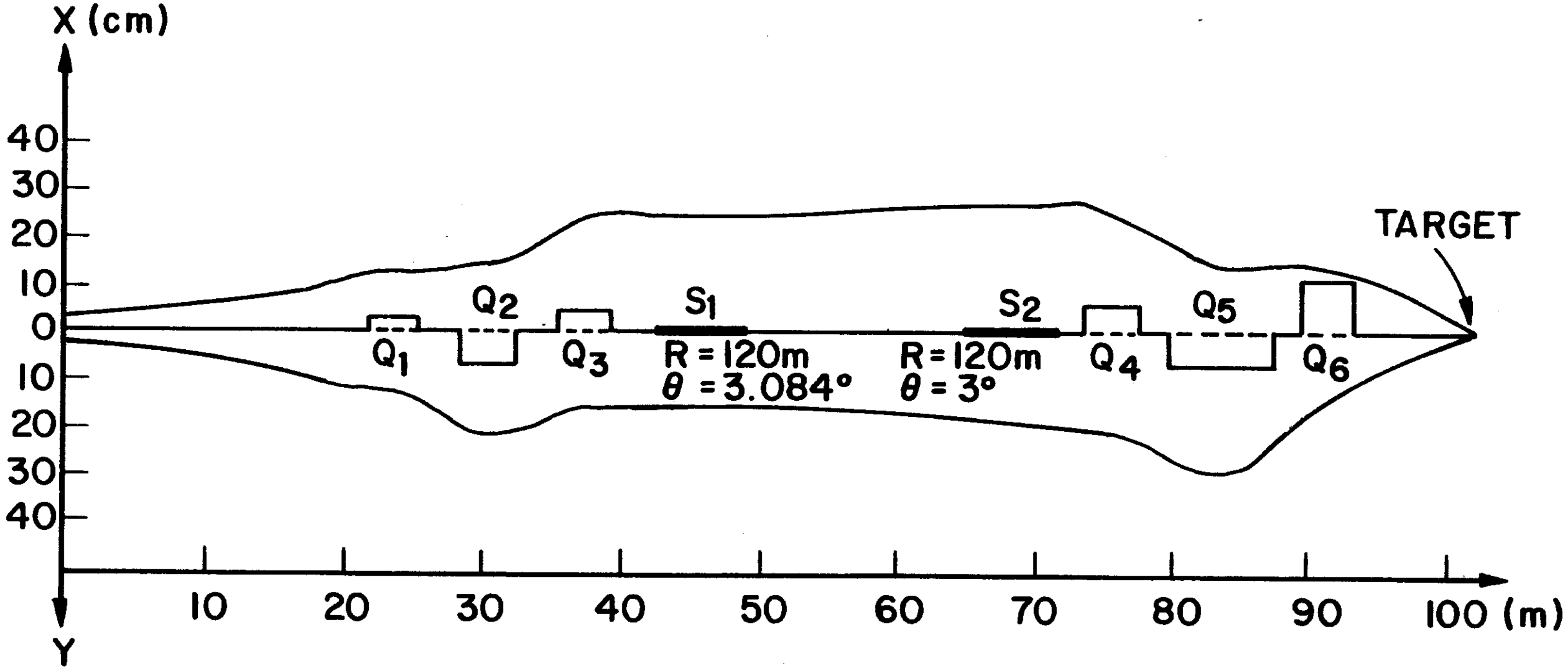

Fig. 6.1 Vertical and horizontal envelopes of the ion beam.

Table 6.1 Description of the Final Focusing System

Element	Length (m)	Field Strength (T)	Aperture Radius (m)	Field Gradient (T/m)
Q1	22	0	0	0
	4	0.65	0.20	2.6
	3	0	0	0
Q2	4	-1.55	0.25	-6.2
	3	0	0	0
Q3	4	1.15	0.25	3.833
	3	0	0	0
S1	6.469	1.757	0.20	[R=120m, θ=3.840°]
	16	0	0	0
S2	6.283	1.757	0.25	[R=120m, θ=3°]
	2	0	0	0
Q4	4	1.45	0.32	4.531
	2	0	0	0
Q5	7.173	-1.7	0.32	-5.313
	2	0	0	0
Q6	3.508	1.8	0.20	9.0
	8.5	0	0	0

tapered along the direct line-of-sight of source neutrons generated at the target such that no direct source neutrons will impinge on the shield in the magnet sections. The shield is tapered also in the drift sections between magnets leading to vertical neutron dumps in these sections. Since scattering is forward peaked for high energy neutrons, the position of the neutron dump in the drift section is chosen to be closer to the target. This shield configuration was found to increase the shielding effectivenss considerably.(4) Figures 6.2, 6.3, 6.4 and 6.5 show vertical and horizontal cross sections of the final focusing system. These cross sections are given for four axial zones covering the 100 m long system. The shield configuration and the locations of the neutron dumps are illustrated. Since no direct source neutrons will stream past the neutron dump between S1 and S2, tapering the inner surface of shield beyond this point is not required and no neutron dumps are needed. The coils used to drive the iron dominated magnets are also shown. The shield in front of the coils was required to have a minimum thickness of 0.3 m.

The final focusing system in HIBALL-II has several attractive features. Table 6.2 gives a comparison between some of the general features that impact the neutronics characteristics of the final focusing systems in HIBALL-I and HIBALL-II. The phase space volume for the ion beams in HIBALL-II is reduced as compared to HIBALL-I. This results in reduced quadrupole apertures. Consequently, the beam port size at the vacuum wall of radius 7 m is reduced by a factor of ~ 10. This leads to significant reduction in radiation streaming into the final focusing system. Furthermore, the reduced aperture allows for use of smaller magnets. A normal coil driven final focusing magnet (Q6) with 1.6 m outside diameter yoke is used. This allows for reduction of the

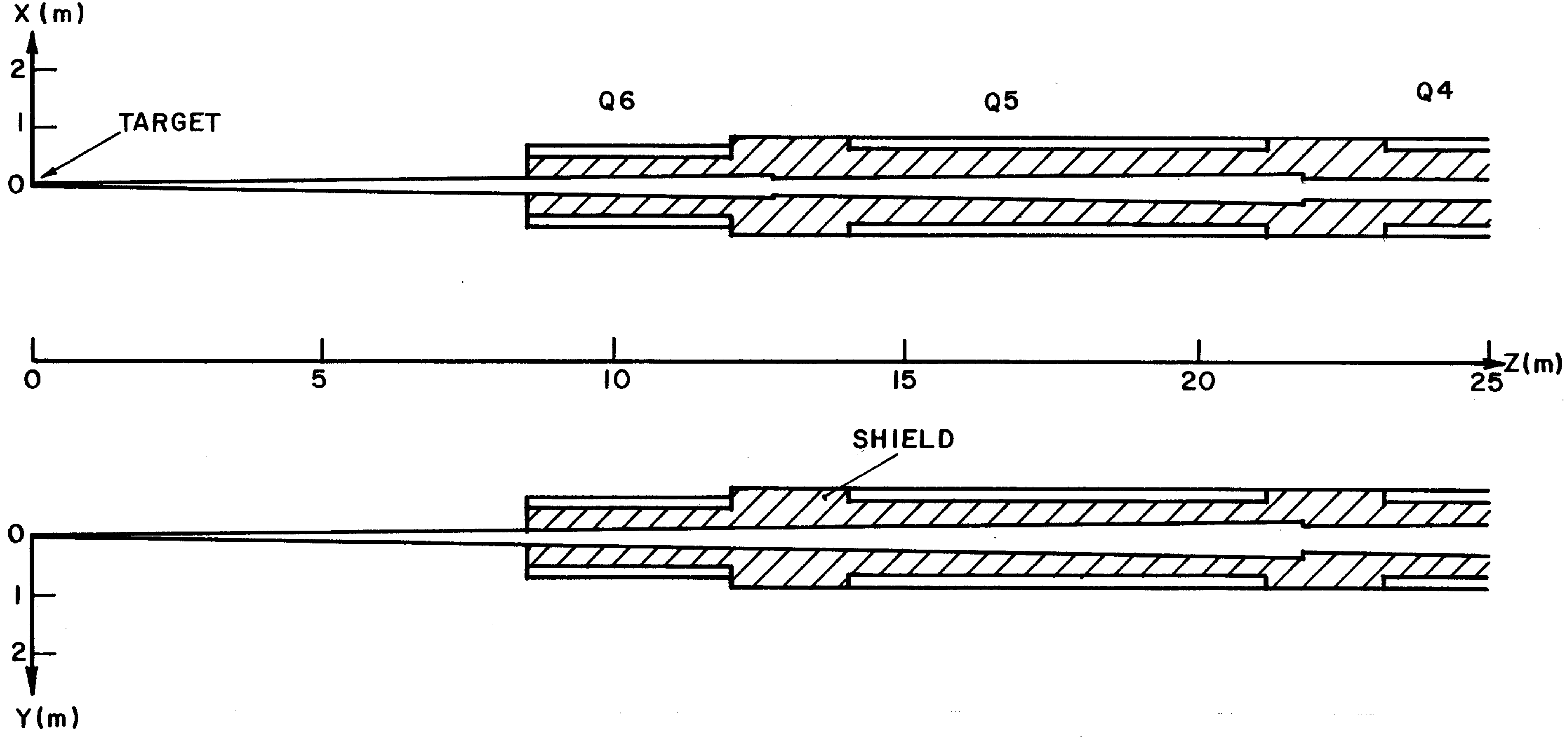

Fig. 6.2 Vertical and horizontal cross sections of the final focusing system in the zone $0 \leq z \leq 25$ m from the target.

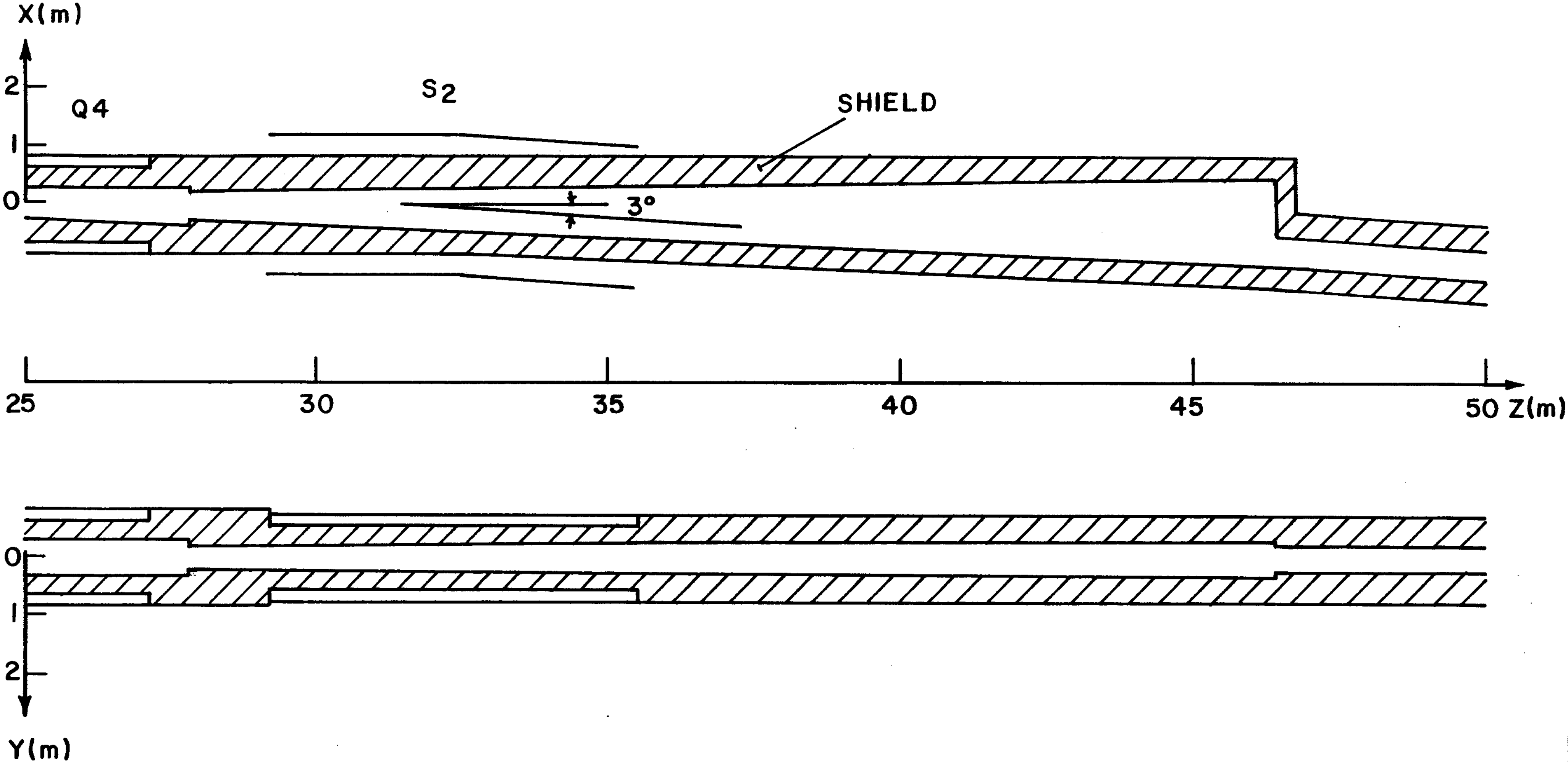

Fig. 6.3 Vertical and horizontal cross sections of the final focusing system in the zone 25 ≤ z ≤ 50 m from the target.

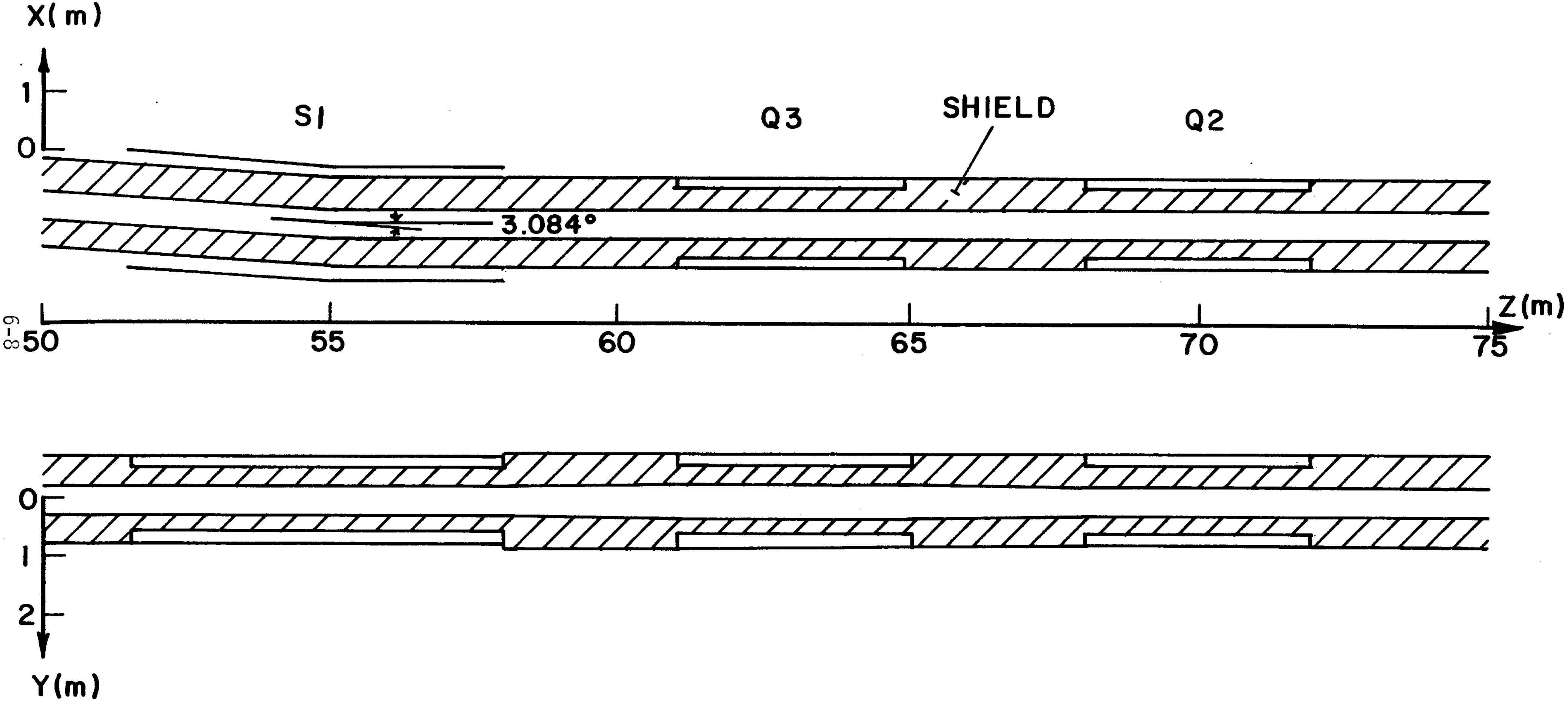

Fig. 6.4 Vertical and horizontal cross sections of the final focusing system in the zone $50 \leq z \leq 75$ m from the target.

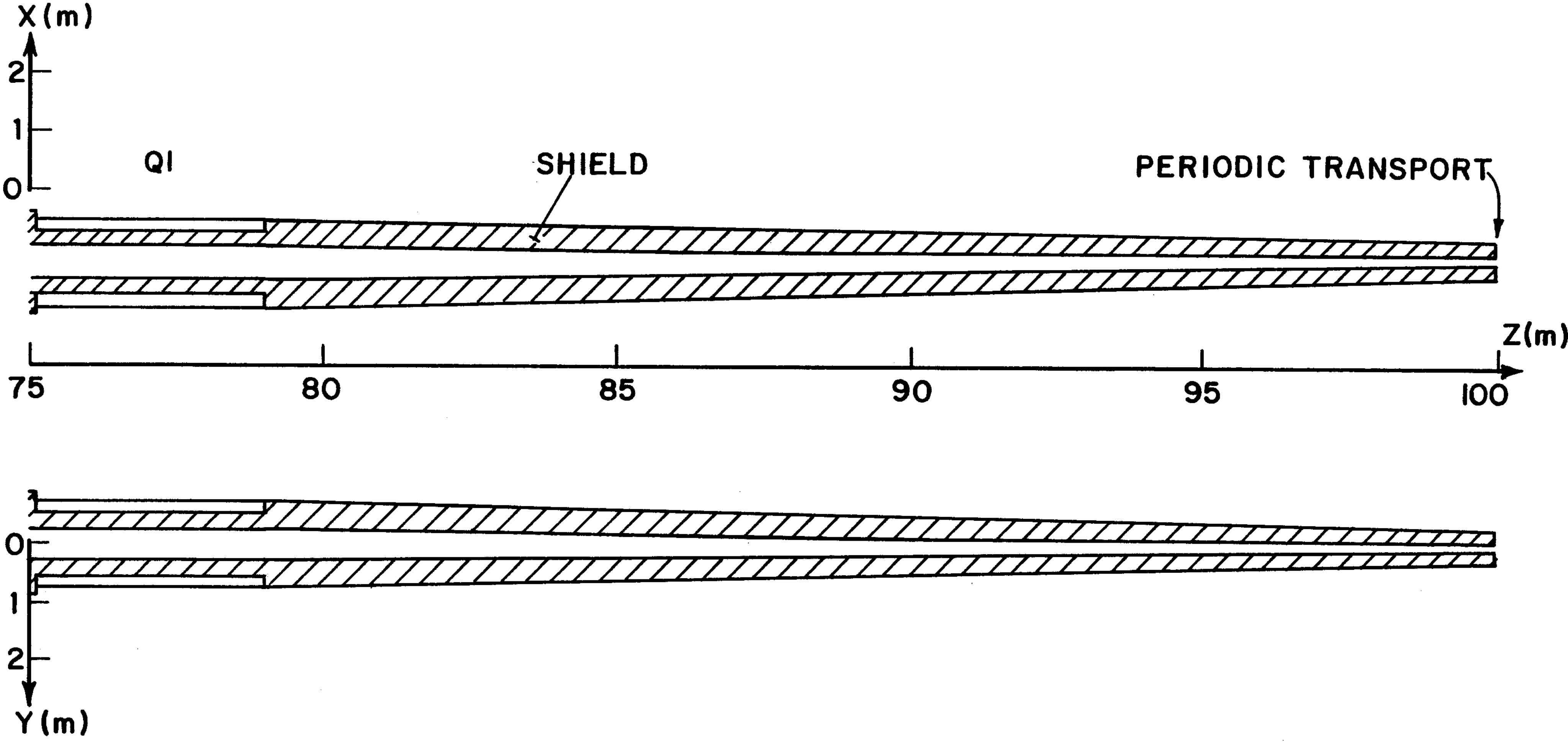

Fig. 6.5 Vertical and horizontal cross sections of the final focusing system in the zone $z \geq 75$ m from the target.

Table 6.2. General Features of the Final Focusing Sytems in HIBALL-I and HIBALL-II

	HIBALL-I	HIBALL-II
Number of quadrupole lenses	8	6
Number of deflection sectors	0	2
Total system length (m)	60	100
Beam port size at vacuum wall (cm x cm)	102.8 x 34.3	21.6 x 16.6
Angle between beams (degrees)	32	16
Largest beam elevation above reactor midplane (m)	16.6	13.0
Number of neutron dumps in the system	8	4

angle between beams to 16°. Together with the beam line bending in the vertical plane, this results in a reduced beam elevation above the center of the reactor chamber even though a longer system is used here. The beam bending allows also for dumping all direct streaming source neutrons ($E_n \sim 12$ MeV) in the system with the periodic transport system being completely concealed from the direct line-of-sight of source neutrons. Four neutron dumps are used along the beam line with most of the source neutrons being dumped in the large final dump 46.5 m from the target. Only slowed down neutrons with a much softer spectrum will stream past this final dump. This results in significant reduction in the amount of radiation streaming into the periodic transport as compared to HIBALL-I which utilizes straight beam lines.

6.3 Calculational Model

HIBALL-II utilizes a 2 m thick blanket consisting of SiC tubes through which the $Li_{17}Pb_{83}$ liquid metal eutectic flows. The tubes occupy 33% of the blanket region. A cylindrical vacuum wall 7 m in radius is used. The first wall is made of HT-9 and is 1 cm thick. A 0.4 m thick reflector composed of 90 v/o HT-9 structure and 10 v/o $Li_{17}Pb_{83}$ coolant is used and followed by a 2.9 m thick reinforced concrete biological shield. Because of its small thickness and negligible effect on radiation streaming, the first wall is not included in the present analysis. The results presented here are based on a DT yield of 400 MJ and a repetition rate of 5 Hz yielding 7.1×10^{20} fusion neutrons per second. Neutron multiplication, spectrum softening and gamma production in the target have been taken into account by performing one-dimensional neutronics and photonics calculations(5) in the spherical target using the discrete ordinates code ANISN.(6)

The twenty beam ports are arranged in two rows which are symmetric about the reactor midplane ($Z = 0$). The beam ports are 2 m apart vertically at the vacuum wall. Because of symmetry only half a penetration is modeled in the present analysis with reflecting albedo boundaries at the planes of symmetry. Hence, only 1/40 of the reactor is modeled. This corresponds to a "pie slice" of the upper half of the reactor with an azimuthal angle of 18°. The angle between the centerline of the beam line penetration and the reactor midplane is 8°. The axes are rotated by 8° around the y axis for the penetration centerline to coincide with the x axis of the calculational model. This simplifies the description of the penetration geometry. The magnet shield is considered to consist of 63 v/o type 316 stainless steel, 15 v/o lead, 17 v/o B_4C and 5 v/o H_2O.

The neutronics and photonics calculations were performed using the three-dimensional Monte Carlo code MORSE.(7) A coupled 25 neutron-21 gamma group cross section library was used. The library consists of the RSIC DLC-41B VITAMIN-C data library(8) and the DLC-60/MACKLIB-IV response data library.(9) The spectra of neutrons and gammas emitted from the target are used to represent the source which is considered to be a point isotropic source at the origin. To get statistically adequate estimates for the flux along the beam line penetration with a reasonable number of histories an angular source biasing technique was used. The biasing technique is similar to that used previously for the analysis of the beam line penetration in HIBALL-I.(10)

This neutronic analysis has several goals. The first goal is to assess the shielding requirements for the superconducting and normal coils. The radiation effects are to be calculated in these coils and compared to the design limits to determine whether the shield used will provide adequate protection to the coils. Because of the $1/R^2$ geometrical attenuation, the largest radiation effects occur in the magnets closer to the source. For this reason and to reduce the computing time, only the final two quadrupoles Q5 and Q6 are modeled. Vertical and horizontal cross sections of the geometry used in the computational model are given in Figs. 6.6 and 6.7. Zone 1 represents the biological shield and zones 2 and 3 represent the reflector and blanket, respectively. The inner vacuum region (zone 14) is extended to the region outside the biological shield and focusing magnets. This allows the neutrons leaking out of the biological shield to have additional collisions in the focusing magnets instead of being discarded as they would be if an outer vacuum region is used. The peak radiation effects are expected to occur in zones 5 and 7 for Q6 and Q5, respectively. Forty thousand histories were used

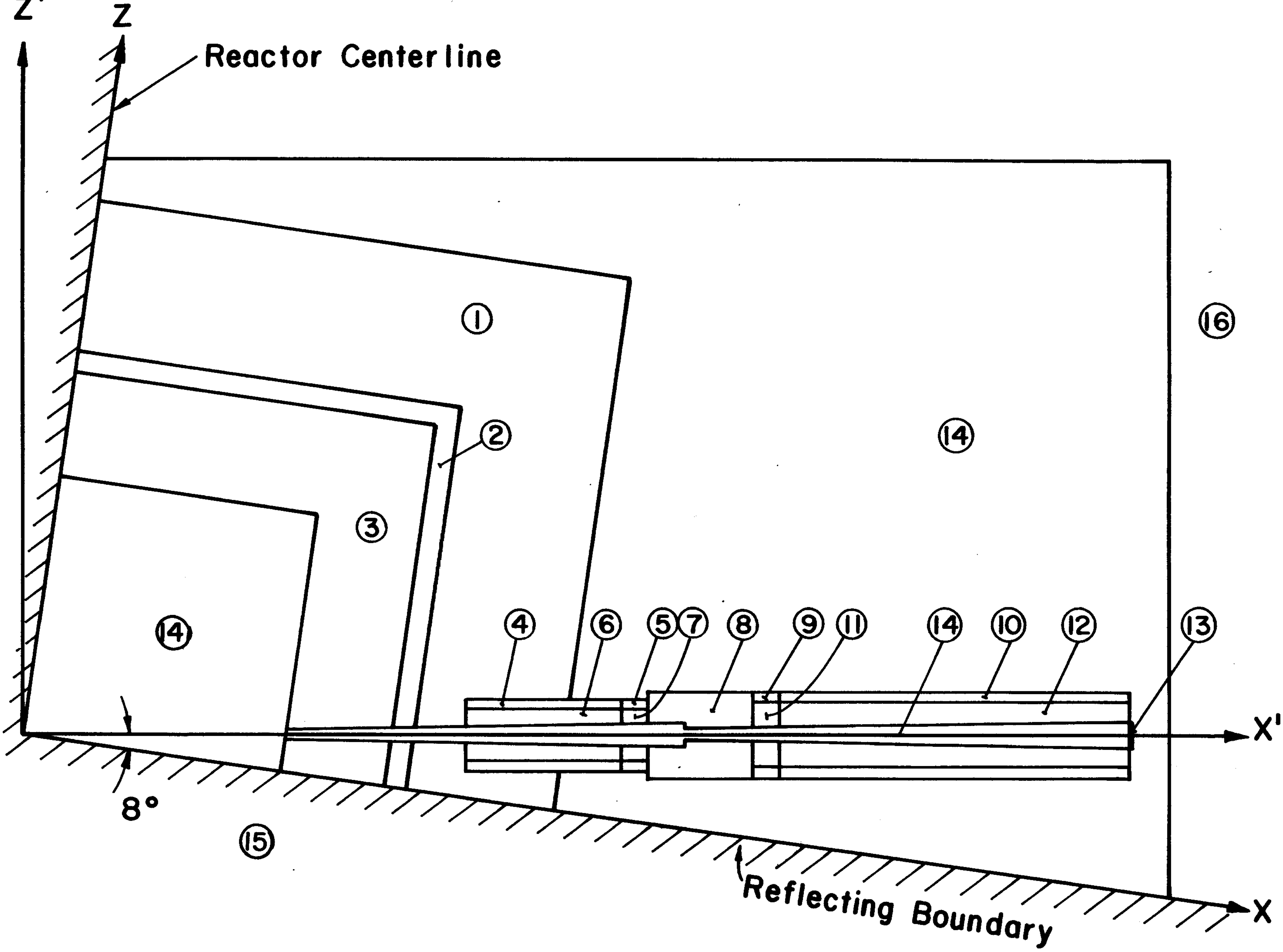

VERTICAL CROSS SECTION PLANE Y = 0

Fig. 6.6 Vertical cross section of computational model.

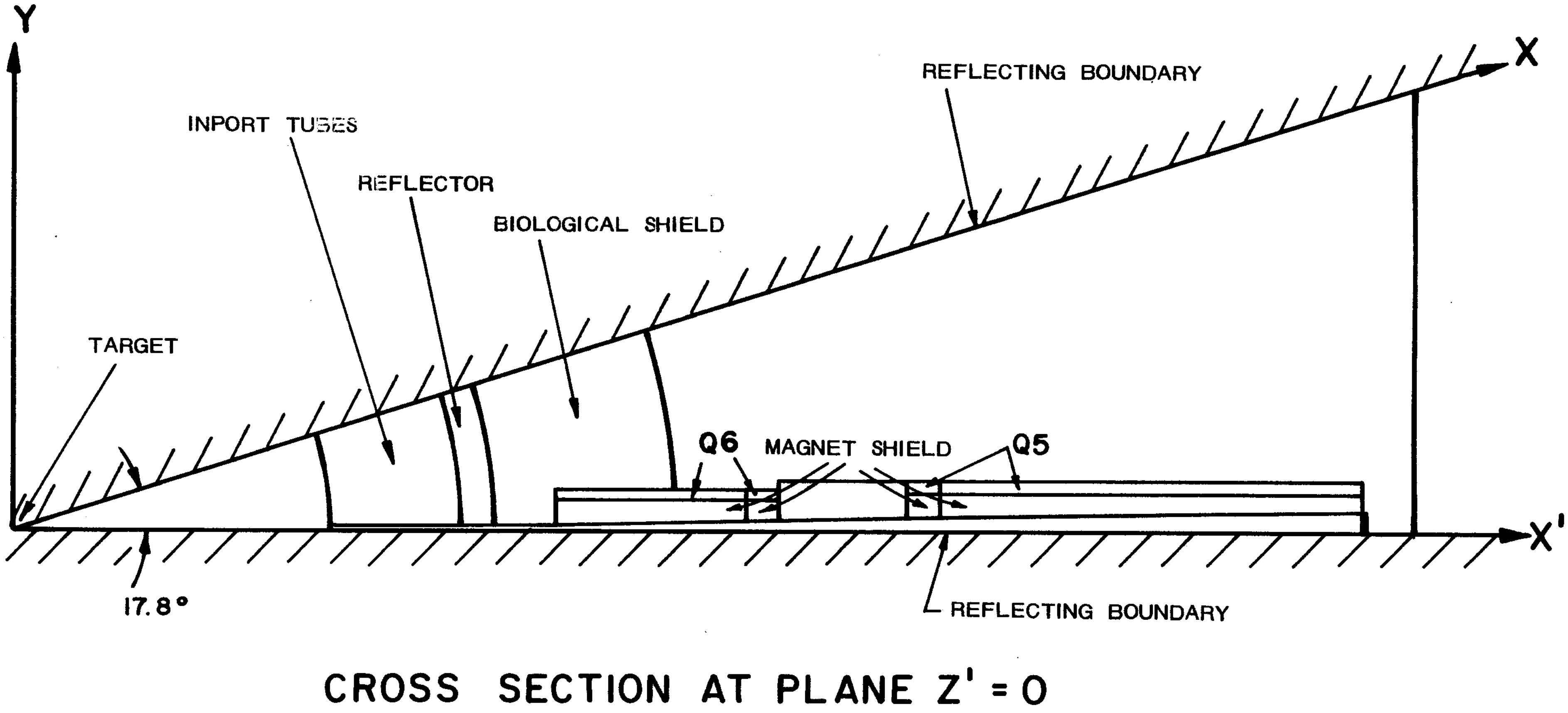

Fig. 6.7 Cross section at plane z'=0 for the computational model.

in the Monte Carlo calculation leading to statistical uncertainties of less than 40% in the coil regions.

Another goal of this analysis is to quantify radiation streaming along the beam line penetration and determine the neutron flux in the neutron dumps and different shield sections for activity and dose calculations. For this purpose, the geometrical model shown in Figs. 6.6 and 6.7 was extended to model the beam line up to the final neutron dump 46.5 m away from the target. Since no direct source neutrons will stream past this dump, only negligible activation will occur in the remainder of the beam line. Hence the beam line is modeled only up to the final neutron dump. To quantify the streaming past this dump, a trapping surface was used at the duct opening at this final dump. Twenty thousand histories were used in this Monte Carlo calculation.

6.4 Radiation Effects in the Coils

The limits on the radiation effects in superconducting and normal coils are design dependent. Since no final magnet design was available at the time this anaylsis was performed, the most conservative limits were picked. The design criteria are also different for superconducting and normal coils.

For superconducting coils, the dpa (displacements per atom) limit in the copper stabilizer is determined by the field at the coil and the total resistivity limit allowed by the magnet designer. The dpa limit decreases as the resistivity limit decreases because of the decreased allowable radiation induced resistivity. The magnetic field at the coils is less than 1 tesla. For oxygen free high conductivity (OFHC) copper with a residual resistivity ratio of 107, the atomic displacements should not exceed 2×10^{-4} dpa for the resistivity not to exceed 5×10^{-8} Ωcm in a 1 tesla field.(11) However, 80% of the radiation induced defects can be removed by room temperature annealing. Several magnet anneals can be performed during the reactor life. A minimum period of 5 full power years (FPY) is required before the first magnet anneal which results in a period of 1 FPY between the final two anneals for an estimated reactor life of 21 FPY. Therefore, the limit on the dpa rate is $4. \times 10^{-5}$ dpa/FPY.

The dose limit for the electrical insulator depends on the insulator type. For epoxies the dose should not exceed 4×10^{8} rad after 21 FPY of reactor life while the limit for polyimides is 5×10^{9} rad for the same period.(12) This implies that the dose rates should not exceed 1.9×10^{7} and 2.4×10^{8} rad/FPY for epoxies and polyimides, respectively. Irradiation of the superconducting material (NbTi) results in degradation of the critical current density. In this work, we require that the peak neutron fluence ($E >$ 0.1 MeV) not exceed 3×10^{22} n/m^2 which corresponds to a 10% decrease in the critical current density.(13) The limit on the peak magnet heat load is considered to be 0.1 mW/cm^3.

For normal coils a fluence limit of 1.1×10^{26} n/m^2 ($E > 0.1$ MeV), which corresponds to 3% swelling of polycrystalline solid MgO insulators, is considered.(14) The fluence limit will be about an order of magnitude higher if compacted MgO powder is used. Ceramic resistivity degradation due to instantaneous dose rates were determined to be significant only for very high does rates ($\geq 10^4$ rad/s) in conjuction with the high voltage gradients across the insulator ($\geq 10^4$ V/cm).(15) In this work, the limit on the instantaneous dose rate in the MgO insulator is taken to be 10^4 rad/s.

Although the final focusing magnets Q6 and Q5 are to be driven by normal and superconducting coils, respectively, the radiation effects in zones 4, 5, 9 and 10 were calculated for both normal and superconducting coils to investigate the possibility of replacing one coil type by the other. Table 6.3 gives the radiation effects in the coils of Q5 and Q6 if they are designed to be superconducting. It is clear that the peak heat load and the peak neutron fluence are well below the design limits for both magnets. After an estimated reactor life of 21 FPY peak dpa values of 3.78×10^{-4} and 6.5×10^{-5} are obtained in the coils of Q6 and Q5, respectively. This implies that no magnet annealing is required for Q5, while if Q6 is driven by superconducting coils it will require two anneals. The total dose in the insulator after 21 FPY is 6.3×10^8 rad in Q6 and 1.3×10^8 rad in Q5. This suggests that epoxies can be used as electrical insulators in the coils of Q5 while if Q6 is driven by superconducting coils the more radiation resistant polyimides have to be used.

The radiation effects in the coils of Q5 and Q6 if they are designed to be normal are given in Table 6.4. It is clear that these values are much lower than the specified design limits. This suggests that a reduced shield thickness can be used with normal coils. The fluence in zone 7 after 21 FPY is 7.9×10^{24} n/m^2 ($E > 0.1$ MeV) which is still well below the design limit of 1.1×10^{36} n/m^2. The instantaneous dose rate in MgO if it were used in this zone is 250 rad/s which is also well below the design limit of 10^4 rad/s. This implies that if normal conductors are used to drive the quadrupole lenses, no shielding is required provided that the inner surfaces of the coils ae tapered along the direct line-of-sight of source neutrons. This results in further reduction of magnet size.

6.5 Radiation Streaming Along the Beam Line

To quantify radiation streaming along the beam line penetration, a computational model for the penetration up to the final neutron dump was used. Particles crossing the trapping surface at the 65 cm x 42 cm duct opening

Table 6.3. Radiation Effects in Superconducting Coils

Quadrupole Lens	Zone Number	DPA Rate in Cu (dpa/FPY)	Dose Rate in Insulator (rad/FPY)	Power Density in Coil (mW/cm^3)	Neutron Fluence (E > 0.1 MeV) (n/m^2/FPY)
Q6	4	9.8×10^{-7}	2.4×10^{7}	0.0023	1.6×10^{19}
	5	1.8×10^{-5}	3.0×10^{7}	0.0076	3.2×10^{20}
Q5	9	3.1×10^{-6}	6.3×10^{6}	0.0018	5.0×10^{19}
	10	3.2×10^{-7}	5.6×10^{5}	0.0002	6.2×10^{18}

Table 6.4. Radiation Effects in Normal Coils

Quadrupole Lens	Zone Number	Neutron Fluence (E > 0.1 MeV) after 21 FPY (n/m^2)	Instantaneous Dose Rate in MgO (rad/s)
Q6	4	3.36×10^{20}	0.50
	5	6.72×10^{21}	1.00
Q5	9	1.05×10^{21}	0.16
	10	1.30×10^{20}	0.02

46.5 m from the target were counted according to energy bins to determine the amount and spectrum of streaming radiation. The neutron and gamma streaming currents are 6.68 x 10^{11} n/cm^{2}s and 1.13 x 10^{11} γ/cm^{2}s, respectively. It is interesting to note that the neutron and gamma streaming currents at the periodic transport (end of final focusing system) in HIBALL-I were 4.4 x 10^{12} n/cm^{2}s and 1.7 x 10^{11} γ/cm^{2}s, respectively. A smaller streaming current is obtained in HIBALL-II as a result of the beam line penetration bending at S2. The reduction in gamma streaming is less pronounced than that for neutron streaming because most of the gamma photons are produced along the beam line duct. Figure 6.8 shows the spectra of neutrons and gammas streaming past the final dump in HIBALL-II. The average energies of streaming neutrons and gammas are 0.77 and 1.52 MeV, respectively. The corresponding values for neutrons and gammas streaming into the periodic transport in HIBALL-I were 11.7 and 1.5 MeV, respectively. Since only slowed down neutrons will stream past the final dump in HIBALL-II, the neutron spectrum is much softer than that in HIBALL-I.

Further reduction in both streaming current and average energy will result as the neutrons travel further up the beam line penetration to the periodic transport 100 m from the target. The neutron streaming current through the duct opening at the vacuum wall of radius 7 m is 8.26 x 10^{14} n/cm^{2}s with an average energy of 12 MeV. This implies that the neutron streaming current is reduced by about three orders of magnitude and the average energy is reduced by about an order of magnitude as the neutrons travel a distance of ~ 40 m in the duct with its 3° bend. The gamma streaming current is reduced by about an order of magnitude in this part of the duct. Since the neutrons streaming past the final neutron dump will travel ~ 54 m in a duct with a

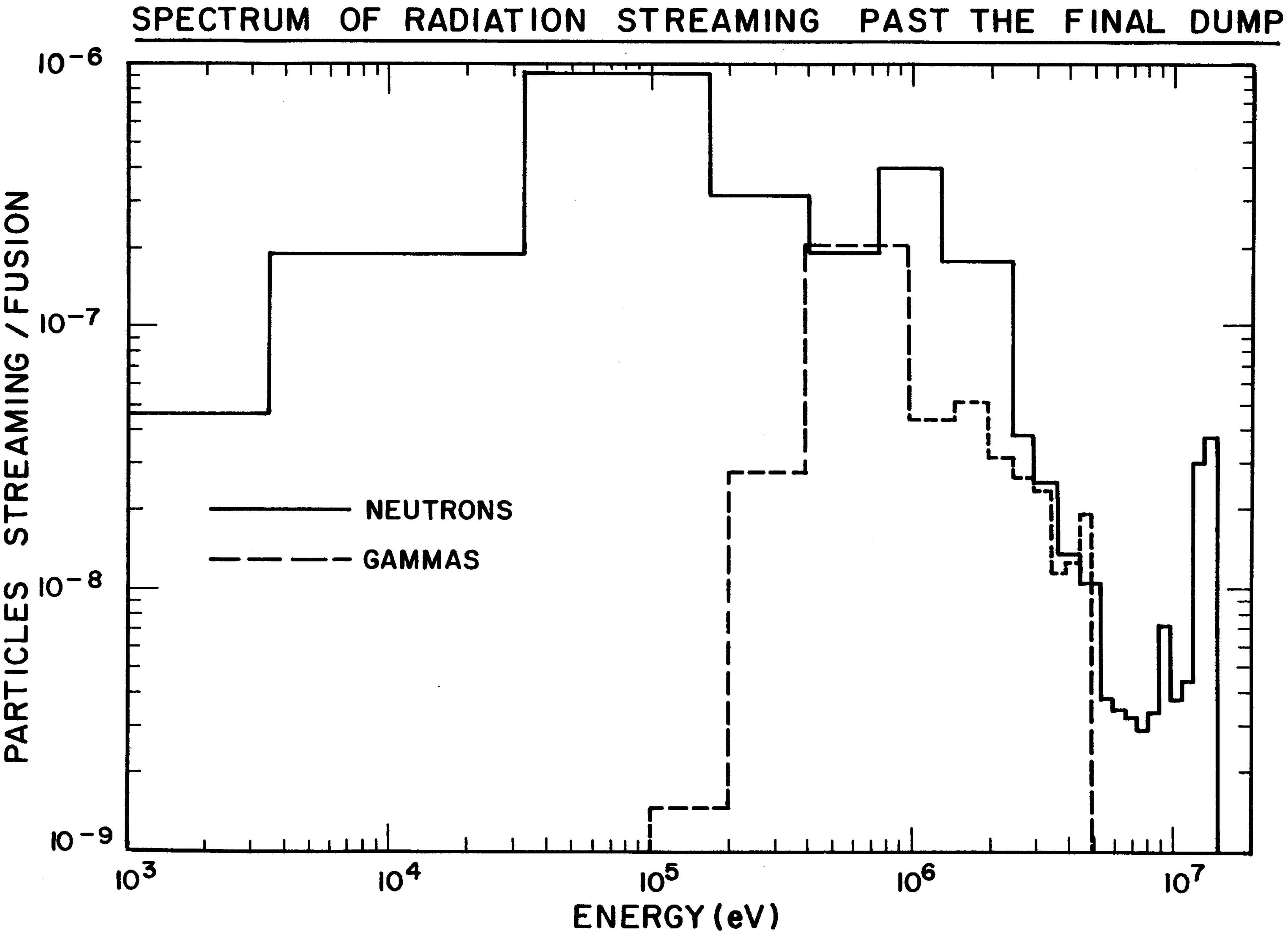

Fig. 6.8 Spectra of radiation streaming past the final dump.

3.084° bend before reaching the periodic transport system, it is expected that the neutron streaming current will be reduced by at least another three orders of magnitude with further spectrum softening. Even more reduction is expected because scattering becomes more isotropic as the neutron energy goes down. Therefore, the final focusing system designed for HIBALL-II results in much less radiation streaming into the periodic transport as compared to that in HIBALL-I.

The neutron spectra were calculated in different sections of the shield along the beam line duct for activation and dose calculations. The total (energy integrated) neutron and gamma fluxes averaged over zones with a 0.5 m thickness are given in Table 6.5. The last zone represents the final neutron dump. It is clear that the largest neutron activation will occur in this dump. If necessary extra shielding can be used behind this dump to reduce the dose after shutdown to permissible levels. The detailed radioactivity results are given in section 7.4.

6.6 Summary

A shield configuration was developed for the final focusing system of HIBALL-II. The inner surface of the shield is tapered along the direct line-of-sight of source neutrons with a number of neutron dumps used in the drift sections between the magnetic elements. Using a minimum shield thickness of 0.3 m it was found that the superconducting coils will be well protected. The radiation effects in the normal coil which drives the final focusing magnet are several orders of magnitude lower than the design limits. No shielding is required in front of the normal coils. A superconducting coil can be used to drive the final quadrupole lens. However, polyimides should be used for electrical insulation and magnet annealing will be required twice during the reactor life. As a result of using two deflection sectors in the system, the periodic transport system is completely concealed from the direct line-of-sight source neutrons. Consequently, neutron streaming into the periodic transport is more than four orders of magnitude less than that in HIBALL-I where a straight beam line was used. Furthermore, the spectrum of streaming neutrons is much softer.

Table 6.5. Neutron and Gamma Fluxes in Different Shield Zones Along the Beam Duct

Distance from Target (m)	Neutron Flux (n/cm^{2}s)	Gamma Flux (γ/cm^{2}s)
8.5-12	8.34E10* (0.12)**	1.81E10 (0.13)
12-14	5.26E11 (0.13)	1.34E11 (0.18)
14-21.2	1.11E10 (0.16)	1.32E9 (0.27)
21.2-23.2	2.16E11 (0.22)	5.06E10 (0.26)
23.2-27.2	1.67E10 (0.54)	5.66E9 (0.56)
27.2-29.2	6.23E11 (0.16)	1.81E11 (0.18)
29.2-35.5	1.44E10 (0.40)	1.59E9 (0.58)
35.5-46.5	3.32E10 (0.10)	5.15E9 (0.09)
46.5-47	1.77E12 (0.10)	5.32E11 (0.11)

---

* Reads 8.34×10^{10}

** Fractional standard deviation

References for Chapter 6

1. J. Jung and M.A. Abdou, Nuclear Technology 41, 71 (1978).
2. M. Ragheb, A. Klein, and C.W. Maynard, Nuclear Technology/Fusion 1, 99 (1981).
3. L. El-Guebaly and C. Maynard, Trans. American Nuclear Society 43, 612 (1982).
4. M.E. Sawan, W.F. Vogelsang, and D.K. Sze, Trans. American Nuclear Society 39, 777 (1981).
5. M.E. Sawan, W.F. Vogelsang, and G.A. Moses, Trans. American Nuclear Society 38, 575 (1981).
6. RSIC Code Package CCC-254, "ANISN-ORNL," Radiation Shielding Information Center, ORNL.
7. RSIC Code Package CCC-203, "MORSE-CG," Radiation Shielding Information Center, ORNL.
8. RSIC Data Library Collection, "VITAMIN-C, 171 Neutron, 36 Gamma-Ray Group Cross Sections Library in AMPX Interface Format for Fusion Neutronics Studies," DLC-41, ORNL.
9. RSIC Data Library Collections, "MACKLIB-IV, 171 Neutron, 36 Gamma-Ray Group Kerma Factor Library," DLC-60, ORNL.
10. B. Badger et al., "HIBALL - A Conceptual Heavy Ion Beam Driven Fusion Reactor Study," University of Wisconsin Fusion Engineering Program Report UWFDM-450, Kernforschungszentrum Karlsruhe Report KfK-3202 (1981).
11. M.E. Sawan, "Radiation Limits in Copper Stablizer of Superconducting Magnets," MARS Project Memo WIS-MARS-82-029 (1982).
12. R. Coltman, Jr. and C. Klabunde, J. Nuclear Materials 103 & 104, 717 (1981).
13. M. Soll, J. Nuclear Materials 72, 168 (1978).
14. L.J. Perkins, "Recommendations for Fluence/Dose Limits for Ceramic Insulators in Normal Conducting Magnets," MARS Project Memo WIS-MARS-82-012 (1982).
15. L.J. Perkins, "Radiation Dose-Rate Resistivity Degradation in Ceramic Insulators and Assessment of the Consequences in Fusion Reactor Applications," University of Wisconsin Fusion Engineering Program Report UWFDM-469 (1982).

7. Radioactivity

The HIBALL report(1) summarized the results of the activity calculated to be present in the structure of a cavity of the reactor. In this section the detailed results of those calculations will be presented along with analyses of the activity present in the coolant and the cavity gas. A preliminary analysis of activity and post shutdown doses in the beam lines is also reported.

7.1 Activity in Structure

The activity in the structure, i.e. the INPORT tubes, first wall, reflector, and shield as well as the activity induced by the reference constituents in the coolant have been summarized in Section VI.3.5 of the HIBALL report. This activity was calculated assuming a two year operating time and was done using a one-dimensional spherical model for the reactor. The fluxes were determined using the ANISN code with the degraded 14 MeV neutron source from the target calculations. The code DKR was then used to determine the activity. While the one-dimensional calculation does not give a true representation of the flux in the HIBALL reactor nevertheless the activity per unit volume calculated from it should give a reasonable estimate of the total inventory of radioactivity in the reactor.

While the DKR code is set up to calculate isotopes produced by more than one neutron capture, the flux levels in the structure of HIBALL are low enough that only single neutron captures are important, consequently the activities presented below may be corrected for other operating times and for decay after shutdown using the first order equations for the generation and decay of radioactivity. The only caveat is when the decay involves more than one radioactive isotope as in the $^{99}\mathrm{Mo} \rightarrow {}^{99}\mathrm{Tc}^{m}$ decay.

7.1.1 Blanket Activity

The activity induced in the blanket region is shown in Table 7.1. The activity of the heavy isotopes comes from the lead in the blanket coolant. This activity was calculated on the basis of the lead being static in the blanket for two years. To get the activity in the coolant itself, corrections will have to be made for the volume fraction of coolant in the blanket and for dilution by coolant not in the reactor cavity. Since most of the activity in the coolant is expected to be generated in the blanket region because of the higher flux in this region, this should provide a good estimate. To this activity must be added the activity due to the bred tritium and activity due to impurities and corrosion products. The latter are considered in Section 7.2 below. The activity due to impurities has not been determined since the nature and levels of impurities are not known. However, it may be anticipated that bismuth is one of these impurities which is important for radioactivity since it can lead to the formation of ^{210}Po. The estimates in the HIBALL report suggested that ~ 600 Ci of ^{210}Po could be present in the system.

7.1.2 First Wall Material

The first wall is HT-9 and as a result the activity of this region involved different materials than in the blanket region. These calculations and subsequent calculations in which HT-9 is involved are based on an HT-9 composition as follows:

Table 7.1. Blanket Activity at Shutdown After Two Years of Full Power Operation

Isotope	Activity (Ci/cm^3)	Half Life	Decay Mode
C^{14}	1.9×10^{-9}	5730 y	β^- (no γ)
Mg^{27}	2.84×10^{-4}	9.45 m	β^-, γ
Al^{28}	0.759	2.24 m	β^-, γ
Al^{29}	9.44×10^{-4}	6.52 m	β^-, γ
Al^{30}	1.11×10^{-3}	3.3 s	β^-, γ
Si^{31}	4.74×10^{-4}	2.62 h	β^-, γ
Hg^{203}	4.90×10^{-3}	46.6 d	β^-, γ
Hg^{205}	4.63×10^{-3}	5.2 m	β^-, γ
Tl^{204}	1.75×10^{-4}	3.78 y	β^-
Pb^{203}	0.258	52.1 h	E.C.
Pb^{205}	1.85×10^{-7}	1.4×10^{7} y	E.C.

Element	w/o
Fe	balance
Cr	11.5
Mo	1
Ni	0.5
W	0.5
Mn	0.5
V	0.3
Si	0.25
C	0.2

The results are summarized in Table 7.2.

7.1.3 Reflector

As stated in the HIBALL report these calculations are based on a reflector composition of 88 w/o HT-9 and 12 w/o $Li_{17}Pb_{83}$. The results are summarized in Table 7.3.

7.1.4 Shield

The activity generated in the shield depends on the detailed specifications of the concrete used. Concrete composition can be quite variable depending on the type and source of the aggregate used. The nature and amount of reinforcement will also contribute to the induced activity. None of these quantities have been precisely specified for HIBALL. Consequently a generic composition has been selected having been taken from various sources. These calculations are based on a shield composition of 13 w/o Fe, 28 w/o Si, 0.5 w/o H, 44 w/o O, 7 w/o Ca, 4 w/o Al, plus 3.5 w/o of other minor constituents. The results are presented in Table 7.4.

Table 7.2. First Wall Activity at Shutdown After Two Years of Full Power Operation

Isotope	Activity (Ci/cm^3)	Half Life	Decay Mode
Mg^{27}	3.6×10^{-6}	9.45 m	β^-, γ
Al^{28}	1.4×10^{-3}	2.24 m	β^-, γ
Al^{29}	1.2×10^{-5}	6.52 m	β^-, γ
Al^{30}	1.4×10^{-5}	3.3 s	β^-, γ
Sc^{31}	3.8×10^{-4}	2.62 h	β^-, γ
Sc^{46}	1.4×10^{-9}	83.8 d	β^-, γ
Sc^{47}	7.6×10^{-7}	3.41 d	β^-, γ
Si^{48}	5.8×10^{-5}	43.7 h	β^-, γ
V^{49}	3.3×10^{-4}	331 d	E.C. (no γ)
V^{52}	0.54	3.755 m	β^-, γ
Ti^{51}	3.4×10^{-4}	5.76 m	β^-, γ
Cr^{49}	1.1×10^{-4}	42.0 m	β^+, γ
Cr^{51}	1.56	27.71 d	E.C.
Cr^{55}	5.9×10^{-3}	3.56 m	β^-, γ
Mn^{53}	1.7×10^{-9}	3.7×10^{6} y	E.C. (no γ)
Mn^{54}	0.014	312.5 d	E.C, γ
Mn^{56}	7.61	2.582 h	β^-, γ
Mn^{57}	8.3×10^{-4}	1.59 m	β^-, γ
Fe^{53}	2.4×10^{-4}	8.53 m	β^+, γ
Fe^{55}	0.25	2.7 y	E.C. (no γ)
Fe^{59}	0.014	44.6 d	β^-, γ
Co^{57}	4.0×10^{-4}	271 d	E.C., γ
Co^{58}	2.0×10^{-3}	71.3 d	E.C., β^+, γ
Co^{60}	8.3×10^{-5}	5.272 y	β^-, γ
Co^{60m}	1.7×10^{-4}	10.5 m	I.T.
Co^{61}	9.1×10^{-6}	1.65 h	β^-, γ
Ni^{57}	1.5×10^{-4}	36 h	E.C., β^+, γ
Ni^{59}	1.7×10^{-7}	8×10^{4} y	E.C. (no γ)
Ni^{63}	2.5×10^{-4}	100 y	β^-, (no γ)
Ni^{65}	6.2×10^{-4}	2.52 h	β^-, γ

Table 7.2. (cont.)

Isotope	Activity (Ci/cm^3)	Half Life	Decay Mode
Zr^{89}	3.1 x 10^{-5}	78.5 h	E.C., β^+, γ
Zr^{93}	4.7 x 10^{-11}	9.5 x 10^5 y	β^-, γ
Zr^{95}	2.2 x 10^{-5}	65.5 d	β^-, γ
Zr^{97}	4.8 x 10^{-6}	16.8 h	β^-, γ
Nb^{92}	6.3 x 10^{-14}	2.7 x 10^7 y	E.C., γ
Nb^{92m}	7.3 x 10^{-5}	10.13 d	E.C., β^+, γ
Nb^{93m}	4.8 x 10^{-5}	12 y	I.T.
Nb^{94}	1.9 x 10^{-9}	2.0 x 10^4 y	β^-, γ
Nb^{95}	3.8 x 10^{-5}	35.1 d	β^-, γ
Nb^{95m}	9.9 x 10^{-6}	3.61 d	I.T.
Nb^{96}	5.2 x 10^{-5}	23.4 h	β^-, γ
Nb^{97}	5.0 x 10^{-5}	73.6 m	β^-, γ
Nb^{97m}	3.2 x 10^{-6}	54 s	I.T.
Nb^{98}	2.8 x 10^{-5}	51 m	β^-, γ
Nb^{100}	5.1 x 10^{-6}	2.9 m	β^-, γ
Mo^{91}	2.0 x 10^{-4}	15.5 m	β^+, γ
Mo^{93}	1.1 x 10^{-3}	3 x 10^3 y	E.C., γ
Mo^{99}	1.01	66.02 h	β^-, γ
Mo^{101}	0.43	14.6 m	β^-, γ
Tc^{99}	6.6 x 10^{-6}	2.13 x 10^5 y	β^-, γ
Tc^{99m}	1.01	6.02 h	I.T.
Tc^{101}	0.43	14.2 m	β^-, γ

Table 7.3. Reflector Activity at Shutdown After Two Years of Full Power Operation

Isotope	Activity (Ci/cm^3)	Half Life	Decay Mode
Mg^{27}	4.0×10^{-7}	9.45 m	β^-, γ
Al^{28}	1.7×10^{-4}	2.24 m	β^-, γ
Al^{29}	1.4×10^{-6}	6.52 m	β^-, γ
Al^{30}	1.6×10^{-6}	3.3 s	β^-, γ
Si^{31}	1.1×10^{-4}	2.62 h	β^-, γ
Sc^{46}	1.6×10^{-10}	83.8 d	β^-, γ
Sc^{47}	1.1×10^{-7}	3.41 d	β^-, γ
Sc^{48}	8.4×10^{-6}	43.7 h	β^-, γ
Ti^{51}	5.4×10^{-5}	331 d	β^-, γ
V^{49}	3.8×10^{-5}	3.755 m	β^-, γ
V^{52}	0.14	5.76 m	E.C. (no γ)
Cr^{49}	1.3×10^{-5}	42.0 m	β^+, γ
Cr^{51}	0.38	27.71 d	E.C., γ
Cr^{55}	2.4×10^{-3}	3.56 m	β^-, γ
Mn^{53}	2.0×10^{-10}	3.7×10^6 y	E.C. (no γ)
Mn^{54}	1.7×10^{-3}	312.5 d	E.C., γ
Mn^{56}	1.93	2.582 h	β^-, γ
Mn^{57}	1.0×10^{-4}	1.59 m	β^-, γ
Fe^{53}	2.7×10^{-5}	8.53 m	β^+, γ
Fe^{55}	0.082	2.7 y	E.C. (no γ)
Fe^{59}	5.3×10^{-3}	44.6 d	β^-, γ
Co^{57}	5.4×10^{-5}	271 d	E.C., γ
Co^{58}	2.4×10^{-4}	71.3 d	E.C., β^+, γ
Co^{60}	1.0×10^{-5}	5.272 y	β^-, γ
Co^{60m}	2.0×10^{-5}	10.5 m	E.T.
Co^{61}	1.3×10^{-6}	1.65 h	β^-, γ
Ni^{57}	2.6×10^{-5}	36 h	E.C., β^+, γ
Ni^{59}	6.7×10^{-8}	8×10^4 y	E.C. (no γ)
Ni^{63}	9.6×10^{-5}	100 y	β^-, (no γ)
Ni^{65}	2.2×10^{-4}	2.52 h	β^-, γ

Table 7.3. (cont.)

Isotope	Activity (Ci/cm^3)	Half Life	Decay Mode
Zr^{89}	3.9×10^{-6}	78.5 h	E.C., β^+
Zr^{93}	9.1×10^{-12}	9.5×10^5 y	β^-, γ
Zr^{95}	4.0×10^{-6}	65.5 d	β^-, γ
Zr^{97}	8.8×10^{-7}	16.8 h	β^-, γ
Nb^{92}	1.1×10^{-14}	2.7×10^7	E.C., γ
Nb^{92m}	9.3×10^{-6}	10.13 d	E.C., β^+, γ
Nb^{93m}	1.1×10^{-5}	12 y	E.T.
Nb^{94}	2.6×10^{-10}	2.0×10^4 y	β^-, γ
Nb^{95}	6.0×10^{-6}	35.1 d	β^-, γ
Nb^{95m}	1.2×10^{-6}	3.61 d	I.T.
Nb^{96}	9.7×10^{-6}	23.4 h	β^-, γ
Nb^{97}	9.8×10^{-6}	73.6 m	β^-, γ
Nb^{97m}	3.7×10^{-7}	54 s	I.T.
Nb^{98}	5.4×10^{-6}	51 m	β^-, γ
Nb^{100}	9.9×10^{-7}	2.9 m	β^-, γ
Mo^{91}	2.3×10^{-5}	15.5 m	β^+, γ
Mo^{93}	2.5×10^{-4}	3×10^3 y	E.C., γ
Mo^{99}	0.22	66.02 h	β^-, γ
Mo^{101}	0.094	14.6 m	β^-, γ
Tc^{99}	1.4×10^{-6}	2.13×10^5 y	β^-, γ
Tc^{99m}	0.22	6.02 h	I.T., γ
Tc^{101}	0.094	14.2 m	β^-, γ
Hg^{203}	6.9×10^{-5}	46.6 d	β^-, γ
Hg^{205}	6.0×10^{-5}	5.2 m	β^-, γ
Tl^{204}	2.8×10^{-6}	3.78 y	β^-, γ
Pb^{203}	7.5×10^{-5}	52.1 h	E.C., γ
Pb^{205}	5.4×10^{-11}	1.4×10^7 y	E.C., γ

Table 7.4. Shield Activity at Shutdown After Two Years of Full Power Operation

Isotope	Activity (Ci/cm^3)	Half Life	Decay Mode
C^{14}	1.3×10^{-13}	5730 y	β^-
N^{16}	3.0×10^{-7}	7.11 s	β^-, γ
Na^{24}	7.7×10^{-8}	15.02 h	β^-, γ
Mg^{27}	8.8×10^{-8}	9.45 m	β^-, γ
Al^{26}	8.8×10^{-15}	7.3×10^5 y	β^+, γ
Al^{28}	2.3×10^{-3}	2.24 m	β^-, γ
Al^{29}	6.3×10^{-9}	6.52 m	β^-, γ
Al^{30}	7.3×10^{-9}	3.3 s	β^-, γ
Si^{31}	5.0×10^{-4}	2.62 h	β^-, γ
Cl^{36}	2.0×10^{-11}	3.0×10^5 y	β^-, (no γ)
Cl^{38}	4.8×10^{-11}	37.2 m	β^-, γ
Ar^{39}	2.1×10^{-7}	269 y	β^-, (no γ)
Ar^{41}	3.2×10^{-10}	1.83 h	β^-, γ
K^{38}	2.1×10^{-10}	7.63 m	β^+, γ
Cr^{51}	9.7×10^{-9}	27.71 d	E.C., γ
Cr^{55}	1.1×10^{-10}	3.56 m	β^-, γ
Mn^{53}	2.9×10^{-15}	3.7×10^6 y	E.C. (no γ)
Mn^{54}	2.9×10^{-8}	312.5 d	E.C., γ
Mn^{56}	1.2×10^{-7}	2.582 h	β^-, γ
Mn^{57}	2.2×10^{-9}	1.59 m	β^-, γ
Fe^{53}	2.9×10^{-10}	8.53 m	β^+, γ
Fe^{55}	5.5×10^{-4}	2.7 y	E.C. (no γ)
Fe^{59}	4.0×10^{-5}	44.6 d	β^-, γ
Co^{57}	9.0×10^{-10}	271 d	E.C., γ
Co^{58}	3.5×10^{-9}	71.3 d	E.C., β^+
Co^{60}	1.2×10^{-10}	5.27 y	β^-, γ
Co^{60m}	1.5×10^{-10}	10.48 m	I.T.
Co^{61}	2.5×10^{-11}	1.65 h	β^-, γ
Ni^{57}	6.7×10^{-10}	36.0 h	E.C., β^+, γ
Ni^{59}	3.6×10^{-10}	8×10^4 y	E.C. (no γ)

Table 7.4. (cont.)

Isotope	Activity (Ci/cm^3)	Half Life	Decay Mode
Ni^{63}	5.2×10^{-7}	100 y	β^-, (no γ)
Ni^{65}	1.1×10^{-6}	2.52 h	β^-, γ

7.2 Activity in the LiPb Coolant

To calculate the activity present in the coolant of the HIBALL reactor three separate source terms must be considered. They are the activation of the reference coolant itself, the transport of activated material into the coolant by corrosion processes, and the activation of non-radioactive material which enters the coolant by the same corrosion processes.

The activity generated in the lithium lead can be found by first calculating the activity of the coolant in a static system to get the total inventory, then distributing this activity over the total mass of coolant. The activity per unit volume for the static case was presented in Sections 7.1.1 and 7.1.2 above. The total activity per chamber is presented in Table 7.5 below. To find the activity per unit volume of the coolant the total coolant volume must be known. However, a detailed design of the heat exchangers and the piping layout was not performed for HIBALL. Until this is done it is not possible to find the specific activity levels in the coolant.

Tritium is also present in the coolant, however, the amount of tritium present is determined by the characteristics of the tritium removal system. Previously the tritium inventory in HIBALL was calculated to be 0.0033 kg (33,000 Ci) in the coolant present in the blanket and reflector regions of the cavity.

To find the activity in the coolant due to corrosion products, the following parameters must be known: the coolant mass and flow rate, the corrosion rate throughout the coolant system, and the corrosion product removal rate through both redeposition and any cleanup system present. Very little information exists on the corrosion of lithium lead and HT-9. Even less information is available on redeposition mechanisms and no corrosion product

Table 7.5. Total Inventory of Radioactivity in Cavity Due to Activation of Lead

Isotope	Total Activity (Ci)	Half Life
Hg^{203}	4.5×10^6	46.6 d
Hg^{205}	4.2×10^6	5.2 m
Tl^{204}	1.6×10^5	3.78 y
Pb^{203}	2.4×10^8	52.1 h
Pb^{205}	1.7×10^2	1.4×10^7 y

removal system has been designed. Consequently insufficient information is available for the calculation. To provide some data on the activation of corrosion products a calculation was made of the activity expected if one gram of each element present in HT-9 were distributed throughout the blanket. The results of this calculation are shown in Table 7.6. Shown is the activity after two years of operation as well as the saturated activity. With this information the activity present in the coolant may be found once the other parameters are known.

7.3 Activity in the Cavity Gas

The activity in the cavity gas is due to the activation of the target materials and to the activated material in the coolant itself. In general, it is expected that the target materials will interact with the lithium lead surface layer and condense into the coolant along with the lithium lead vapor. The exceptions are the non-condensibles.

There are two important radioactive noncondensibles in the cavity: tritium and ^6He. The latter is characterized by a decay constant of 0.864/s

Table 7.6

Average Specific Saturation Activity of Corrosion Products in HIBALL Blanket

Per Gram of Element

Isotope	Saturation Activity Ci/g	$T_{1/2}$	Activity After Two Years Operation Ci/g
Silicon			
^{28}Al	5.11	2.24 m	5.11
^{29}Al	6.41×10^{-2}	6.5 m	6.41×10^{-2}
^{31}Si	3.20×10^{-2}	2.62 h	3.20×10^{-2}
^{30}Al	7.47×10^{-2}	3.6 s	7.47×10^{-2}
Vanadium			
^{47}Sc	4.16×10^{-1}	3.14 d	4.16×10^{-1}
^{49}V	6.51	331 d	5.10
^{48}Sc	3.82×10^{-4}	43.7 h	3.82×10^{-4}
^{51}Ti	1.24×10^{-3}	5.75 m	1.24×10^{-3}
^{52}V	6.36×10^{-2}	3.76 m	6.36×10^{-2}
^{51}Cr	2.04×10^{1}	27.71 d	2.04×10^{1}
Iron			
^{53}Mn	5.84×10^{-2}	3.8×10^{6} y	2.13×10^{-8}
^{54}Mn	2.51×10^{-1}	312.5 d	2.01×10^{-1}
^{55}Fe	3.49	2.7 y	1.40
^{53}Fe	6.11×10^{-3}	8.53 m	6.11×10^{-3}
^{56}Mn	1.02	2.58 h	1.02
^{57}Mn	1.51×10^{-2}	1.59 m	1.51×10^{-2}
^{55}Cr	4.11×10^{-4}	3.55 m	4.11×10^{-4}
^{59}Fe	2.18×10^{-3}	44.6 d	2.18×10^{-3}

Table 7.6. (cont.)

Corrosion Product Activity (cntd.)

Tungsten Isotope	Saturation Activity Ci/g	$T_{1/2}$	Activity After Two Years Operation Ci/g
^{182}Ta	1.76×10^{-3}	115 d	1.74×10^{-3}
^{181}W	1.14	121 d	1.12
^{183}Ta	2.12×10^{-3}	5.0 d	2.12×10^{-3}
^{181}Hf	7.75×10^{-4}	42.4 d	7.73×10^{-4}
^{184}Ta	1.73×10^{-3}	8.7 h	1.73×10^{-3}
^{185}W	3.91×10^{1}	75.1 d	3.91×10^{1}
^{186}Ta	6.43×10^{-4}	10.5 m	6.43×10^{-4}
^{187}W	1.01×10^{2}	23.9 h	1.01×10^{2}
^{183}Hf	5.03×10^{-3}	64 m	5.03×10^{-3}
^{185}Ta	3.48×10^{-5}	49 m	3.48×10^{-5}
Chromium			
^{49}V	3.54×10^{-2}	331 d	2.77×10^{-2}
^{51}Cr	4.45	27.7 d	4.45
^{49}Cr	1.29×10^{-2}	42.0 m	1.29×10^{-2}
^{52}V	8.31×10^{-1}	3.76 m	8.31×10^{-1}
^{51}Ti	2.79×10^{-3}	5.75 m	2.79×10^{-3}
^{55}Cr	3.46×10^{-3}	3.55 m	3.46×10^{-3}
Carbon			
^{14}C	2.52×10^{-5}	5.73×10^{3} y	6.11×10^{-9}

Table 7.6. (cont.)

Corrosion Product Activity (contd.)

Nickel

Isotope	Saturation Activity Ci/g	$T_{1/2}$	Activity After Two Years Operation Ci/g
^{55}Fe	$9.8\text{x}10^{-1}$	2.7 y	$3.91\text{x}10^{-1}$
^{57}Co	$9.17\text{x}10^{-1}$	271 d	$7.76\text{x}10^{-1}$
^{58}Co	3.12	70.8 d	3.12
^{59}Ni	2.61	$8\text{x}10^{4}$ y	$4.52\text{x}10^{-5}$
^{57}Ni	$1.58\text{x}10^{-1}$	36.1 h	$1.58\text{x}10^{-1}$
^{60}Co	$8.17\text{x}10^{-1}$	5.27 y	$1.89\text{x}10^{-1}$
^{60}Co^{m}	$4.64\text{x}10^{-1}$	10.48 m	$4.64\text{x}10^{-1}$
^{61}Co	$1.43\text{x}10^{-2}$	1.65 h	$1.43\text{x}10^{-2}$
^{59}Fe	$5.42\text{x}10^{-3}$	44.6 d	$5.42\text{x}10^{-3}$
^{63}Ni	$3.91\text{x}10^{-1}$	100 y	$5.42\text{x}10^{-3}$
^{65}Ni	$1.85\text{x}10^{-2}$	2.52 h	$1.85\text{x}10^{-2}$
Manganese			
^{52}V	$2.72\text{x}10^{-1}$	3.76 m	$2.72\text{x}10^{-1}$
^{55}Cr	$4.91\text{x}10^{-1}$	3.55 m	$4.91 \text{ x } 10^{-1}$
^{54}Mn	5.89	312.5 d	4.72
^{56}Mn	$2.00\text{x}10^{2}$	2.58 h	$2.00\text{x}10^{2}$

Table 7.6. (cont.)

Corrosion Product Activity (contd.)

Molybdenum

Isotope	Saturation Activity Ci/g	$T_{1/2}$	Activity After Two Years Operation Ci/g
$^{92}\mathrm{Nb}^{m}$	$6.58x10^{-2}$	10.13 d	$6.58x10^{-2}$
$^{91}\mathrm{Mo}$	$2.52x10^{-1}$	15.5 m	$2.52x10^{-1}$
$^{93}\mathrm{Mo}$	$8.38x10^{1}$	$3.5x10^{3}$ y	$3.32x10^{-2}$
$^{93}\mathrm{Nb}^{m}$	$1.38x10^{-1}$	13.6 y	$1.40x10^{-3}$
$^{92}\mathrm{Nb}$	$3.12x10^{-3}$	$1.6x10^{8}$ y	$2.70x10^{-11}$
$^{94}\mathrm{Nb}$	$2.26x10^{-1}$	$2.0x10^{4}$ y	$1.57x10^{-5}$
$^{95}\mathrm{Nb}$	$2.03x10^{-2}$	3.5 d	$2.03x10^{-2}$
$^{95}\mathrm{Nb}^{m}$	$7.04x10^{-3}$	3.61 d	$7.04x10^{-3}$
$^{93}\mathrm{Zr}$	$1.22x10^{-2}$	$1.5x10^{6}$ y	$1.12x10^{-8}$
$^{96}\mathrm{Nb}$	$1.68x10^{-2}$	23.4 h	$1.68x10^{-2}$
$^{97}\mathrm{Nb}$	$8.72x10^{-3}$	73.6 m	$8.72x10^{-3}$
$^{97}\mathrm{Nb}^{m}$	$3.25x10^{-3}$	54 s	$3.25x10^{-3}$
$^{98}\mathrm{Nb}$	$7.76x10^{-3}$	51.1 m	$7.76x10^{-3}$
$^{95}\mathrm{Zr}$	$8.29x10^{-3}$	64.0 d	$8.29x10^{-3}$
$^{99}\mathrm{Mo}$	$2.09x10^{1}$	66.0 h	$2.09x10^{1}$
$^{99}\mathrm{Tc}^{m}$	$2.09x10^{1}$	6.02 h	$2.09x10^{1}$
$^{99}\mathrm{Tc}$	$2.13x10^{1}$	$2.13x10^{5}$ y	$1.39x10^{-4}$
$^{100}\mathrm{Nb}$	$1.02x10^{-3}$	3.1 s	$1.02x10^{-3}$
$^{97}\mathrm{Zr}$	$1.69x10^{-3}$	16.8 h	$1.69x10^{-3}$
$^{101}\mathrm{Mo}$	7.41	14.6 m	7.41
$^{101}\mathrm{Tc}$	7.41	14.2 m	7.41

($T_{1/2}$ = 0.802 s) and an average beta energy of 1.75 MeV. The HIBALL report gives the hydrogen pressure immediately before a shot as 1.5×10^{-4} torr of D_2 and T_2 at 400°C. When the relative fractions of both isotopes are considered the tritium inventory is 113 Ci. The average over the complete time between shots is 127 Ci.

The ^{6}He is pumped from the cavity along with the ^{4}He produced in the target. Since the ^{4}He concentration is very much greater than the ^{6}He concentration, the He pumping speed is determined by the ^{4}He. The helium pressure before a shot as calculated in the HIBALL report is 1.3×10^{-4} torr. The helium pumping speed is 8.7×10^5 ℓ/s which when combined with a cavity volume of 1.14×10^6 ℓ yields a helium pumping removal constant $\lambda_p = 0.763/\text{s}$. At the reference power level there are $S = 5.13 \times 10^{16}$ ^{6}He nuclei produced per shot. The average number of ^{6}He nuclei in the system is then $\overline{N}_{^6\text{He}} = S/\lambda_{^6\text{He}} T$, where T is the time between shots. Thus

$$\overline{N}_{^6\text{He}} = \frac{5.13 \times 10^{16}}{0.864 \times 0.2} = 2.97 \times 10^{17} \ .$$

The average number of ^{6}He in the cavity itself is given by

$$\overline{N}_{^6\text{He cavity}} = \frac{S}{(\lambda_{^6\text{He}} + \lambda_p)T} = \frac{5.13 \times 10^{16}}{(0.864 + 0.763)0.2} = 1.59 \times 10^{17}$$

and the corresponding activity

$$\overline{A}_{^6\text{He cavity}} = 3.71 \times 10^6 \text{ Ci} \ .$$

The average number of ^{6}He nuclei in the pumping system is

$$\overline{N}_{^6\text{He pump}} = \overline{N}_{^6\text{He}} - \overline{N}_{^6\text{He cavity}} = (2.97 - 1.59) \times 10^{17} = 1.38 \times 10^{17} .$$

The corresponding activity is

$$\overline{A}_{^6\text{He pump}} = 3.22 \times 10^{6} \text{ Ci} .$$

While this activity level is high the corresponding radiological consequences are small because of the short half life. However, the decay energy may not be insignificant as a heat load on the cryopanels of the pumping system.

The power produced in the pumps is given by

$$P_{^6\text{He}} = \lambda_{^6\text{He}} N_{^6\text{He pump}} \overline{E}$$

$$= 0.864/\text{s} \times 1.38 \times 10^{17} \times 1.75 \text{ MeV} \times 1.6 \times 10^{-13} \text{ J/MeV}$$

$$= 3.34 \times 10^{4} \text{ W} = 33 \text{ kW}.$$

7.4 Beam Line Activity and Dose Levels

A determination of the activity generated in a beam line of HIBALL is of interest both to arrive at an estimate of the inventory of radioactivity and to estimate dose levels outside the beam line shielding. However, the calculation is complicated by several factors. The beam line geometry is too complicated for a simple one-dimensional analysis and therefore Monte Carlo techniques must be used. The cross sections for reactions leading to radioactive nuclei are only a small part of the total cross section and consequently most histories will not result in reactions of interest. Furthermore the beam line is quite long and a very large number of histories would have to be used to obtain a detailed spatial resolution of the activity generated. In addition only a schematic design of the magnets and shielding for the beam line has been made so that the calculations are only indicative of activity and dose levels which would be present in an actual engineering design. Even after activity levels have been calculated the dose calculations are difficult because of the geometry and lack of a detailed design.

Consequently a simplifed model of the beam line has been used to endeavor to obtain some information on activity and dose levels. The model used has been described in Chapter 6 of the report and shown in Fig. 7.1. The beam line out to the primary beam dump has been broken up into twelve cylindrical regions. The regions correspond to the last four magnet windings (regions 10-13), the shielding between these magnets and the beam line (regions 1, 3, 5, 7) and the drift spaces between the magnets (regions 2, 4, 6, 8). The magnet windings are assumed to be 20 cm thick and of the generic magnet composition discussed in Chapter 6. The 30 cm shielding between the magnet windings and line and the 50 cm shield in the drift regions were taken to be 316 stainless steel. An additional region (region 9) was used to model the beam dump which was also taken to be 316 stainless steel. The neutron fluxes from the Monte Carlo calculations were then used in the DKR code to calculate the activities in each of these regions. The results of these calculations are presented in Table 7.7. The activity levels as calculated are quite low: 65.6 curies at shutdown for the entire beam line. Furthermore a large part of this activity is due to ^{56}Mn ($T_{1/2}$ = 2.58 hr) which will decay out within the first day after shutdown. It should be noted that the uncertainty in the numbers is

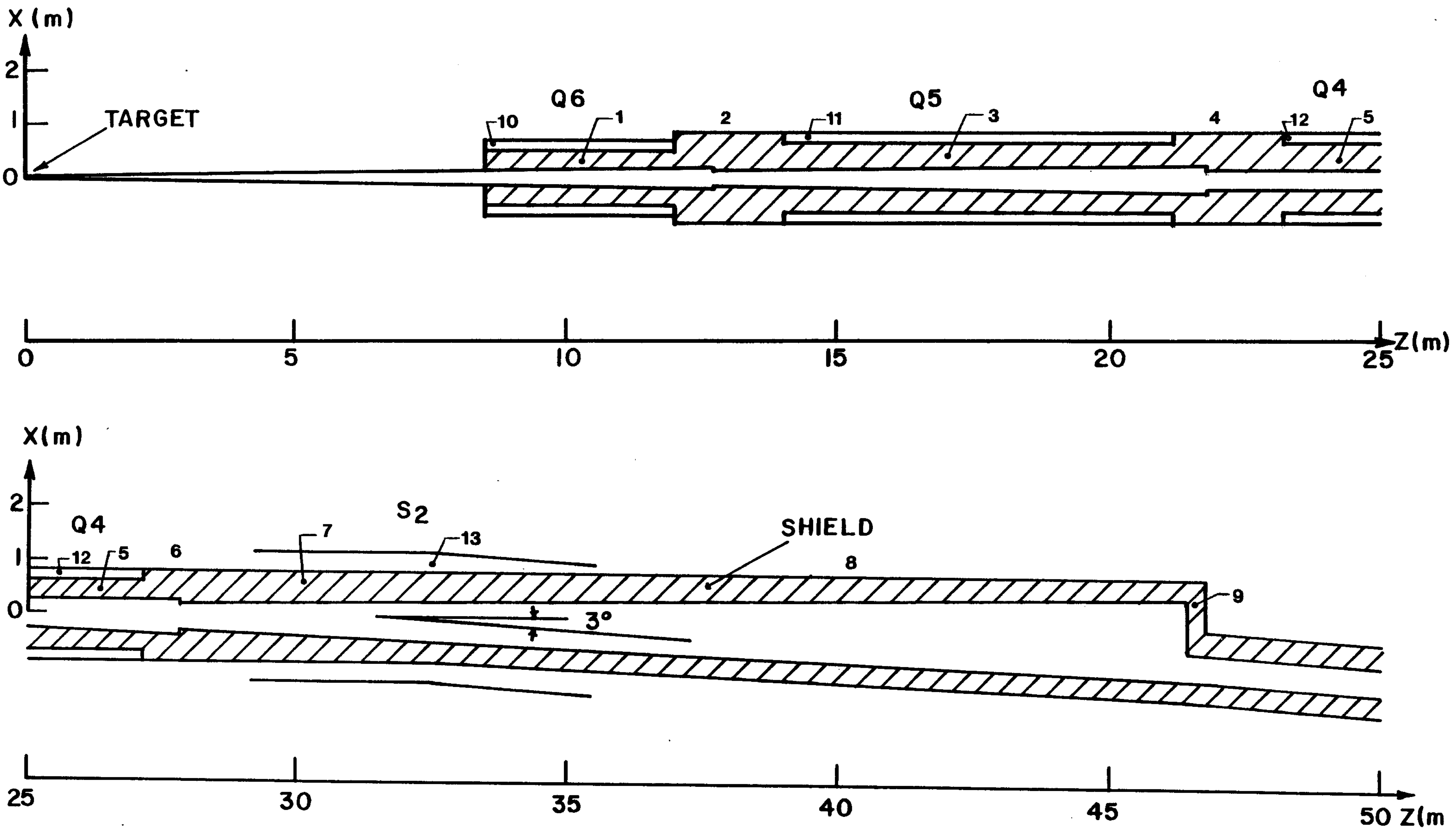

Figure 7.1 Beam line model for radioactivity and dose calculations.

Table 7.7. Beam Line Activity at Shutdown

Isotope	1	2	3	4
(Volume)	(1.55x10^{6} cm^{3})	(2.531x10^{6} cm^{3})	(4.65x10^{6} cm^{3})	(2.42x10^{6} cm^{3})
	Ci/cm^{3}	Ci/cm^{3}	Ci/cm^{3}	Ci/cm^{3}
V^{52}	2.5x10^{-11}	9.5x10^{-10}	3.5x10^{-12}	3.7x10^{-10}
Cr^{51}	3.4x10^{-8}	1.2x10^{-6}	3.0x10^{-9}	5.3x10^{-8}
Mn^{54}	6.5x10^{-11}	1.2x10^{-9}	4.0x10^{-12}	4.8x10^{-10}
Mn^{56}	3.7x10^{-7}	2.4x10^{-6}	3.0x10^{-8}	6.4x10^{-7}
Fe^{55}	2.0x10^{-8}	3.8x10^{-7}	1.4x10^{-9}	2.7x10^{-8}
Ni^{59}	3.9x10^{-13}	7.4x10^{-12}	2.8x10^{-14}	5.1x10^{-13}
Ni^{63}	5.7x10^{-10}	1.1x10^{-8}	4.1x10^{-11}	7.3x10^{-10}
Mo^{93}	3.5x10^{-12}	2.2x10^{-11}	3.3x10^{-13}	8.2x10^{-12}
Mo^{99}	1.71x10^{-8}	9.2x10^{-8}	1.6x10^{-9}	3.4x10^{-8}
Mo^{101}	8.8x10^{-9}	4.6x10^{-8}	7.7x10^{-10}	1.7x10^{-8}
Tc^{99}	1.1x10^{-13}	6.0x10^{-13}	1.0x10^{-14}	2.2x10^{-13}
Total Region Activity (curies)	0.75	21.8	0.18	4.0

Isotope	5	6	7	8	9
(Volume)	(4.754x10^{6} cm^{3})	(2.44x10^{6} cm^{3})	(8.575x10^{6} cm^{3})	(1.837x10^{7} cm^{3})	(9.568x10^{5} cm^{3})
	Ci/cm^{3}	Ci/cm^{3}	Ci/cm^{3}	Ci/cm^{3}	Ci/cm^{3}
V^{52}	1.1x10^{-11}	1.4x10^{-9}	7.6x10^{-12}	1.3x10^{-11}	4.1x10^{-9}Ci/cm^{3}
Cr^{51}	2.8x10^{-9}	5.1x10^{-7}	2.8x10^{-9}	3.1x10^{-8}	4.3x10^{-7}
Mn^{54}	1.4x10^{-11}	1.9x10^{-9}	1.1x10^{-11}	1.2x10^{-11}	5.7x10^{-9}
Mn^{56}	6.2x10^{-8}	2.3x10^{-6}	5.7x10^{-8}	1.7x10^{-7}	5.6x10^{-6}
Fe^{55}	2.2x10^{-9}	1.9x10^{-7}	8.1X10^{-10}	1.2x10^{-8}	3.7x10^{-7}
Ni^{59}	4.4x10^{-14}	3.8x10^{-12}	1.6x10^{-14}	2.4x10^{-13}	6.9x10^{-12}
Ni^{63}	6.4x10^{-11}	5.4x10^{-9}	2.3x10^{-11}	3.4x10^{-10}	1.0x10^{-8}
Mo^{93}	8.0x10^{-13}	2.5x10^{-11}	1.0x10^{-12}	2.2x10^{-12}	6.8x10^{-11}
Mo^{99}	3.2x10^{-9}	1.1x10^{-11}	3.6x10^{-9}	8.6x10^{-9}	2.6x10^{-7}
Mo^{101}	1.6x10^{-9}	5.4x10^{-8}	1.9x10^{-9}	4.4x10^{-9}	1.3x10^{-7}
Tc^{99}	2.1x10^{-14}	6.9x10^{-13}	2.3x10^{-14}	5.6x10^{-14}	1.7x10^{-12}
Total Region Activity (curies)	0.37	16.3	0.62	8.9	7.0

Table 7.7. (cont.)

Isotope	10	11	12	13
(Volume)	(1.55×10^{6} cm^3)	(2.531×10^{6} cm^3)	(4.65×10^{6} cm^3)	(2.42×10^{6} cm^3)
	Ci/cm^3	Ci/cm^3	Ci/cm^3	Ci/cm^3
V^{52}	2.2×10^{-11}	3.0×10^{-12}	9.5×10^{-12}	6.5×10^{-12}
Cr^{51}	2.9×10^{-8}	2.6×10^{-9}	2.4×10^{-9}	2.4×10^{-9}
Mn^{54}	5.6×10^{-11}	3.4×10^{-12}	1.2×10^{-11}	9.8×10^{-12}
Mn^{56}	3.2×10^{-7}	2.5×10^{-8}	5.3×10^{-8}	4.9×10^{-8}
Fe^{55}	1.7×10^{-8}	1.2×10^{-9}	1.9×10^{-9}	6.9×10^{-10}
Ni^{59}	3.4×10^{-13}	2.4×10^{-14}	3.8×10^{-14}	1.4×10^{-14}
Ni^{63}	5.0×10^{-10}	3.5×10^{-11}	5.6×10^{-11}	2.1×10^{-11}
Cu^{64}	8.8×10^{-7}	7.2×10^{-8}	1.5×10^{-7}	1.5×10^{-7}
Cu^{66}	9.4×10^{-8}	7.0×10^{-9}	8.5×10^{-9}	2.9×10^{-9}
Mo^{93}	3.0×10^{-12}	2.8×10^{-13}	6.8×10^{-13}	8.9×10^{-13}
Mo^{99}	1.5×10^{-8}	1.3×10^{-9}	2.7×10^{-9}	3.1×10^{-9}
Mo^{101}	7.5×10^{-9}	6.6×10^{-10}	1.4×10^{-9}	1.6×10^{-9}
Tc^{99}	9.7×10^{-14}	8.7×10^{-15}	1.8×10^{-14}	2.0×10^{-14}
Total Regions Activity (curies)				
	2.2	0.53	1.1	1.9

expected to be quite large because of the limited number of histories used in the flux determination.

While the activity levels in the beam line are low relative to those in the vicinity of the cavity they are high enough to produce an unacceptable biological dose level. An estimate of the dose levels expected behind the beam dump and outside the shield in the drift space before the final magnet is made in the following section.

7.4.1 Beam Dump (Region 9)

In the previous calculation the total activity in the beam dump was calculated. To perform the shielding calculation the spatial distribution of the gamma sources in the dump must be known. The simplest approach would be to assume a uniform distribution throughout the 50 cm thickness. This approach, however, would not be realistic since the neutrons producing the sources are attenuated passing through the dump. The resulting dose levels would be artificially high and probably unacceptable. To obtain a more realistic source distribution the source was redistributed as an exponential with a 5 cm relaxation length. This behavior is in approximate agreement with the behavior of neutrons in shielding systems. The dump then was approximated as an infinite slab with the volumetric source. The resulting dose rate at the back of the shield at shutdown is 2.6 mrem/hr while one day after shutdown it has fallen to only 0.03 mrem/hr. This rapid falloff is due to the decay of the short lived ^{56}Mn. While these calculations are rather crude they do indicate that acceptable dose levels can be obtained even allowing for changes in the source distribution.

7.4.2 Drift Shield (Region 2)

Similar comments may be made about the spatial source distribution in this region as were made for the beam dump as the activity was redistributed using the same model as for the beam dump. Here, however, this is an even more conservative approach. In this region, because of the direction of the incident neutrons down the beam line, most of the activity will be near the inner surface and in the secondary beam dump between the magnets. Additionally this is a cylindrical region and no credit was taken for the 1/r term expected in this geometry. The resulting dose at shutdown calculated using cylindrical geometry was found to be 1.1 mrem/hr while one day after shutdown it was reduced to 0.02 mrem/hr due to the decay of ^{56}Mn.

These quite conservative calculations indicate that the shielding as presented for the beam line is adequate and in fact may be reduced significantly (10-20 cm) in regions such as the drift spaces between the magnets if a more detailed design is made, the calculation refined, and more precise criteria established for allowable dose rates.

Reference for Chapter 7

1. B. Badger et al., "HIBALL - A Conceptual Heavy Ion Beam Driven Fusion Reactor Study," University of Wisconsin Fusion Design Memo UWFDM-450, Chapter VI, (June 1981).

8. Current Status of Li-Pb Corrosion

The results of recent capsule test performed by P. Tortorelli(1) are summarized in Table 8.1. These capsule test results were compared to the previously measured capsule corrosion data of Li on steel, as shown in Fig. 8.1. It appears that $Li_{17}Pb_{83}$ is two orders of magnitude more corrosive than Li. This raises the question of using $Li_{17}Pb_{83}$ as the coolant and breeding material for a fusion reactor. However, the previously measured Pb corrosion on steel in a loop system did not show a factor of 100 more severe corrosion than Li on steel,(2) as shown later in Fig. 8.8 of this chapter. Therefore, the results of the capsule tests are not consistent with the loop test results.

The capsule and specimen are shown on Fig. 8.2. For the $Li_{17}Pb_{83}$ system, a wire loop ties the specimen to the top of the capsule. The capsule is turned upside down and put into the oven. The wire loop prevents the specimen from floating to the top. For the Li experiment, the specimen is dropped to the Li pool and sinks to the bottom. The capsule is heated and/or cooled on opposite sides to keep the temperature of Li (or LiPb) within a predetermined limit. The heating or cooling action, however, generates a natural convection current in the capsule and, therefore, the specimen is not under a static condition.

The velocity distribution of a parallel plate system heated on one side and cooled on the other is shown in Fig. 8.3. The velocity and temperature difference can be calculated by

$$V_z = \frac{\rho\beta g b^2 \Delta T}{12\mu} \left[\left(\frac{y}{b}\right)^3 - \frac{y}{b}\right] \qquad (8.1)$$

Table 8.1

Weight Losses of 12 Cr-1 MoVW Exposed to Pb-17 Atom % Li

Temperature (°C)	Weight Loss (g/m^2) 1000 h	3000 h	5000 h
300	2.3	6.6	6.0
400	3.2	5.6	5.0
500	6.5	7.6	7.6

Weight Losses of Type 316 Stainless Steel Exposed to Pb-17 Atom % Li

Temperature (°C)	Weight Loss (g/m^2) 1000 h	3000 h	5000 h
300	0.4	0.4	1.0
400	0.9	1.2	3.2
500	7.6	14.6	12.2
600	12.1	25.9	13.0
700	6.0	12.0	5.5

Fig. 8.1. Corrosion by $Li_{17}Pb_{83}$ and Li

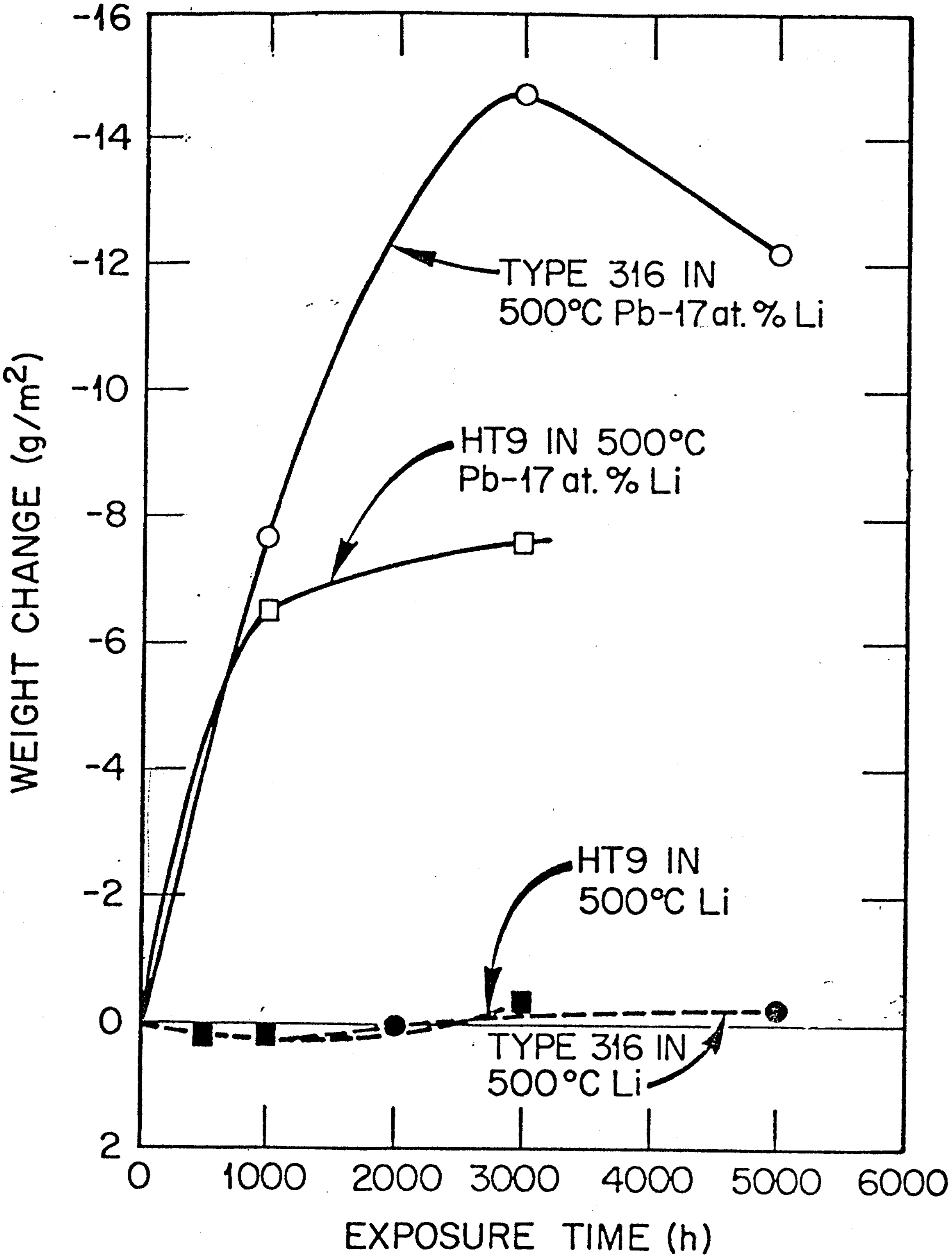

Fig. 8.2

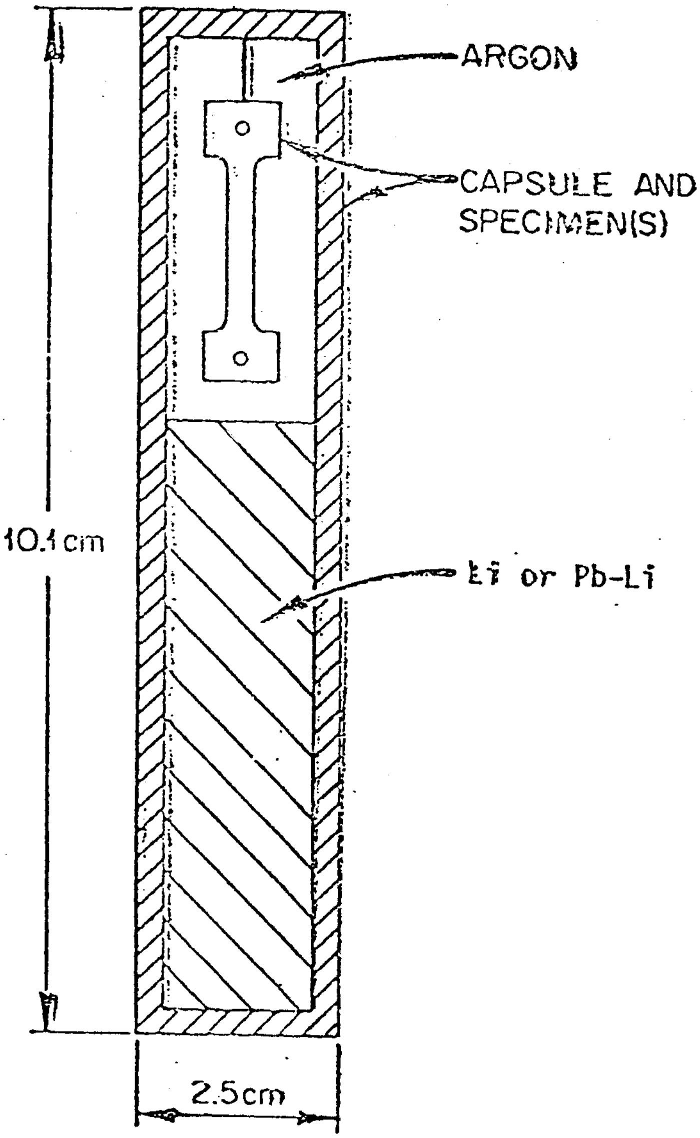

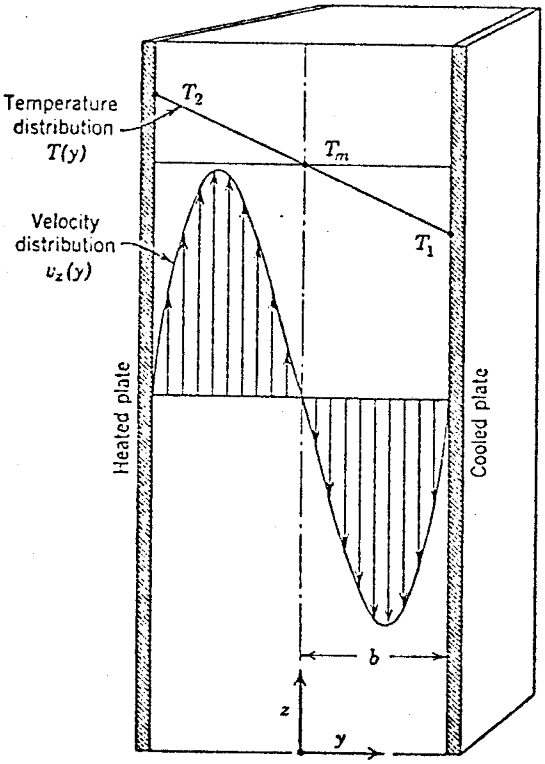

Fig. 8.3 Laminar free-convection flow between two vertical plates at two different temperatures; the velocity is a cubic function of the distance.

$$\frac{q''}{\Delta T} = \frac{k}{b} \cdot 0.56 \cdot \left[\frac{g\beta b^3 \Delta T}{\nu^2} \cdot \frac{c_p \mu}{k}\right]^{1/4} \quad . \qquad (8.2)$$

These equations can be solved for ΔT and V_z.

For the ORNL experiments, the maximum velocity of $Li_{17}Pb_{83}$ is calculated to be 6 cm/sec while for Li is 2 cm/sec.

The velocity is strongly location dependent, as can be seen in Fig. 8.1. The steel specimen in $Li_{17}Pb_{83}$ is suspended from the top of the capsule and is, therefore, subjected to the maximum velocity. On the other hand, the steel specimen in Li is leaning against the wall and is, therefore, subjected to a much lower velocity than the maximum value. Therefore, the capsule results of steel in $Li_{17}Pb_{83}$ are similar to a loop test, while that of steel in Li is similar to a static test. This is another interpretation of the difference in corrosion rate shown on Fig. 8.1. Further experiments will be required to verify this interpretation.

A theoretical model to predict the dissolution corrosion rate by Li or Pb on steel has been developed based on mass transfer considerations. The corrosion rate in a mass transfer system can be described by the following correlation:

$$\dot{M} = K_s \, (C_s - C_b) \qquad (8.3)$$

in which $\dot{M}$ is the corrosion rate

K_s is the mass transfer coefficent

C_s is the concentration of the corrosion product at the solid/liquid interface, and

C_b is the bulk concentration in the liquid.

This relationship is far more complicated that it appears. The mass transfer coefficient depends on the mass diffusivity, the flow characteristics and the physical properties of the two materials. The concentration of the corrosion products at the solid/liquid interface can be estimated from their solubilities. The bulk concentration in the liquid can be calculated by following the corrosion product transport through the entire coolant loop. To solve this equation is, therefore, clearly beyond the scope of this study. However, this relationship can provide some very useful information on the magnitude of corrosion of Pb on steel.

At the beginning of the operation, the coolant is clean, or $C_b = 0$. Therefore

$$\dot{M} = K_s C_s . \tag{8.4}$$

This will give the maximum corrosion rate. The mass transfer coefficient is linearly dependent on the diffusivity D. Therefore, the corrosion rate can be scaled as

$$\dot{M} \propto D C_s . \tag{8.5}$$

The diffusivity of a molecule through a liquid can be estimated by Stoke's Einstein equation,(3)

$$D = kT/6\pi\mu R_i \tag{8.6}$$

in which: k is Boltzmann's constant

T is temperature

μ is viscosity of the liquid

R_i is radius of the diffusing molecule.

The solubilities of iron in lithium and lead have been measured and are shown in Figs. 8.4 and 8.5, respectively. It is interesting to note that the solubility of iron in lead is much more temperature dependent than the solubility of iron in lithium. Since most of the lead corrosion experiments were carried out at high temperatures (>600°C), it is not surprising that lead has been observed as being very corrosive.

Figure 8.6 compares the solubilities as weight fractions and in terms of g/cm^3 for Fe/Li and Fe/Pb. The solubility in units of g/cm^3 is the driving force for the mass transfer. The solubilities cross over at 440°C. This means that Fe is less soluble in Pb than in Li below 440°C and, therefore, the driving force for mass transfer is smaller. However, as can be seen from Eq. (8.5), the kinetics of mass transfer also depend on the diffusivity. If the solubility of Fe in Pb is corrected by both the density factor and the diffusivity, the curves corresponding to Fe in Li and Fe in Pb cross over at 600°C, as can be seen in Fig. 8.7. Since the volumetric coolant flow rate is inversely proportional to the (ρc_p) of the materials, the solubility can also be normalized by (ρc_p). For such comparison the solubility curves cross over at 550°C as shown in Fig. 8.7. For this reason, it can be concluded that the corrosion of Li on Fe and Pb on Fe cross over at 550-600°C. Since HIBALL is designed for a maximum Li/steel interface temperature of 500°C, Pb is less corrosive than Li. It is conservative, therefore, to use Li corrosion data for the design of HIBALL.

Figure 8.4

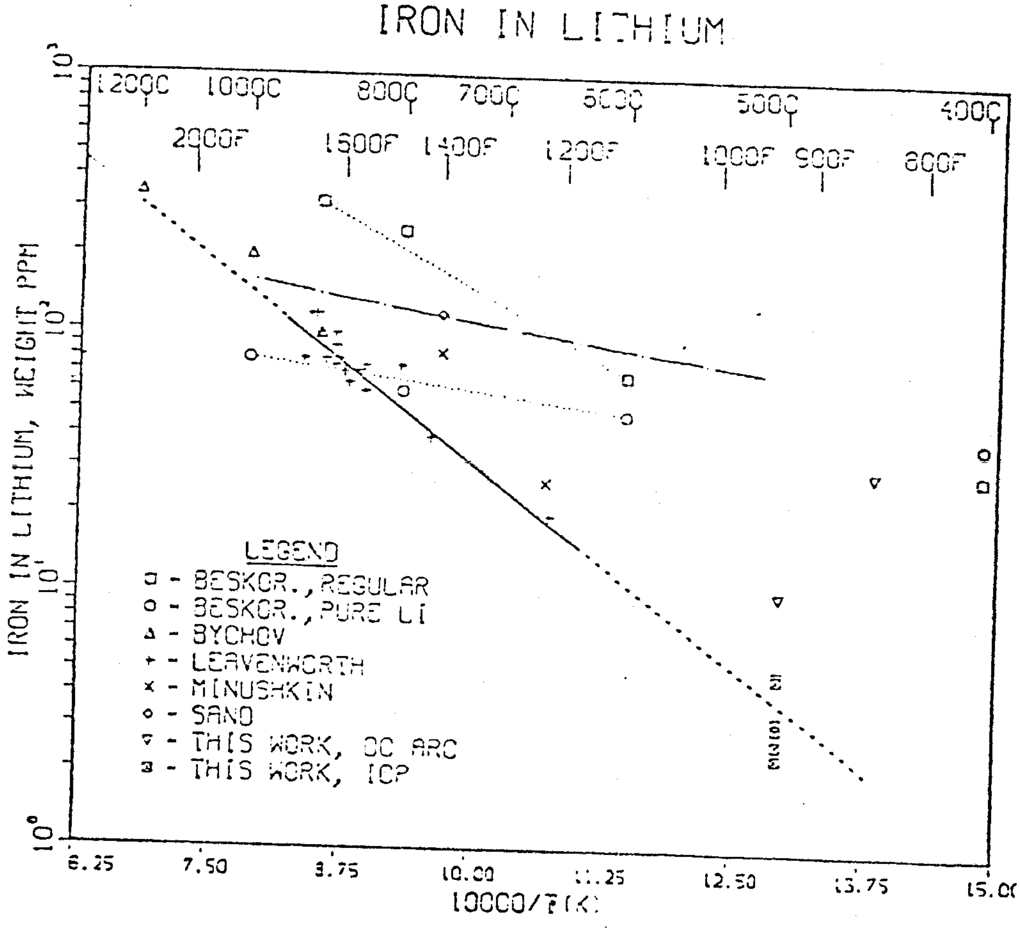
IRON IN LITHIUM
IRON IN LITHIUM, WEIGHT PPM
10^3
10^2
10^1
10^0
1200C
1000C
800C
700C
600C
500C
400C
2000F
1500F
1400F
1200F
1000F
900F
800F
LEGEND
□ - BESKOR., REGULAR
○ - BESKOR., PURE LI
△ - BYCHOV
+ - LEAVENWORTH
× - MINUSHKIN
◇ - SAND
▽ - THIS WORK, DC ARC
⊡ - THIS WORK, ICP
6.25
7.50
8.75
10.00
11.25
12.50
13.75
15.00
10000/T(K)

Figure 8.5

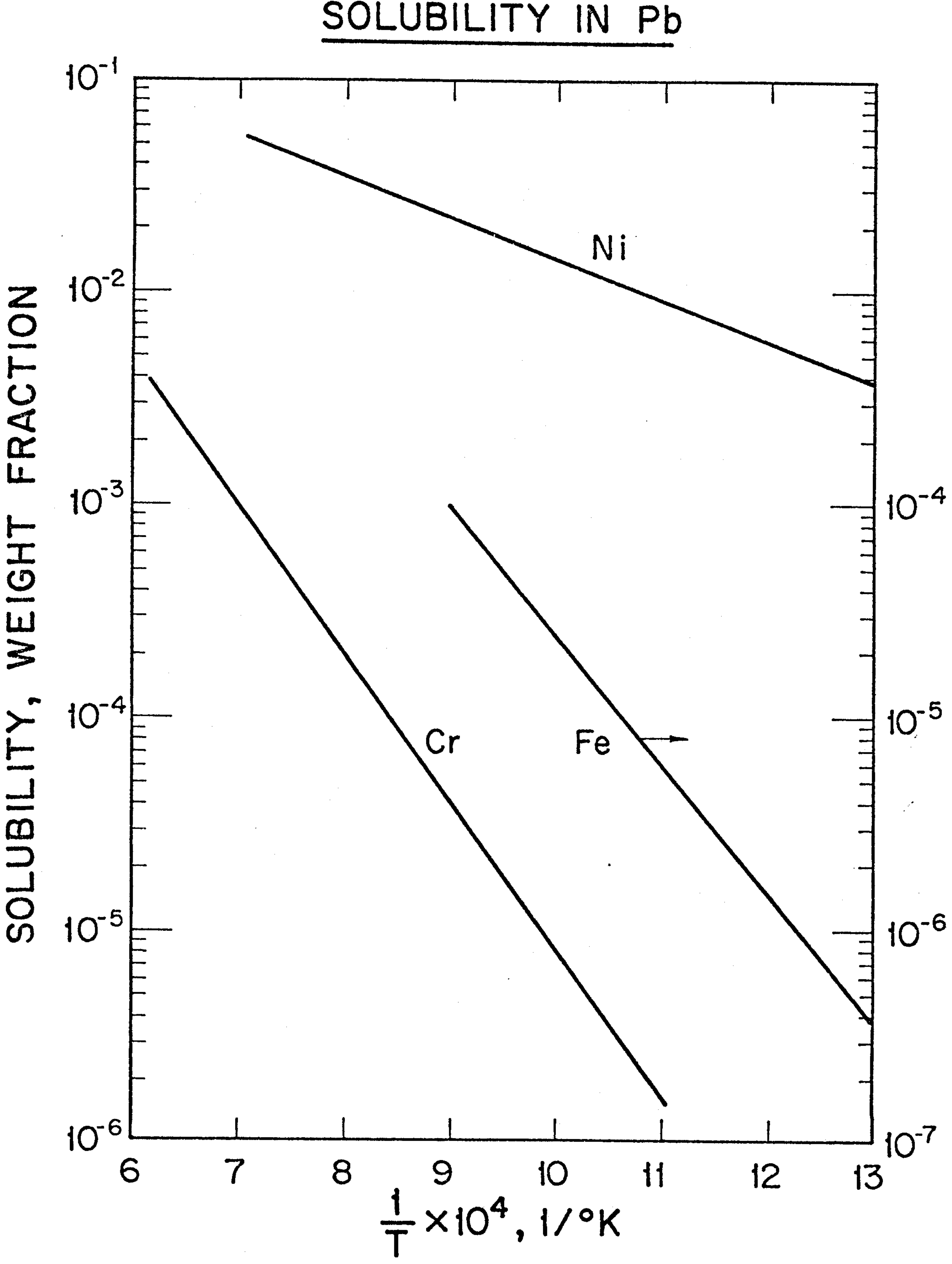
SOLUBILITY IN Pb
SOLUBILITY, WEIGHT FRACTION
10^{-1}
10^{-2}
10^{-3}
10^{-4}
10^{-5}
10^{-6}
10^{-4}
10^{-5}
10^{-6}
10^{-7}
Ni
Cr
Fe
6
7
8
9
10
11
12
13
$\frac{1}{T} \times 10^4$, 1/°K

Fig. 8.6

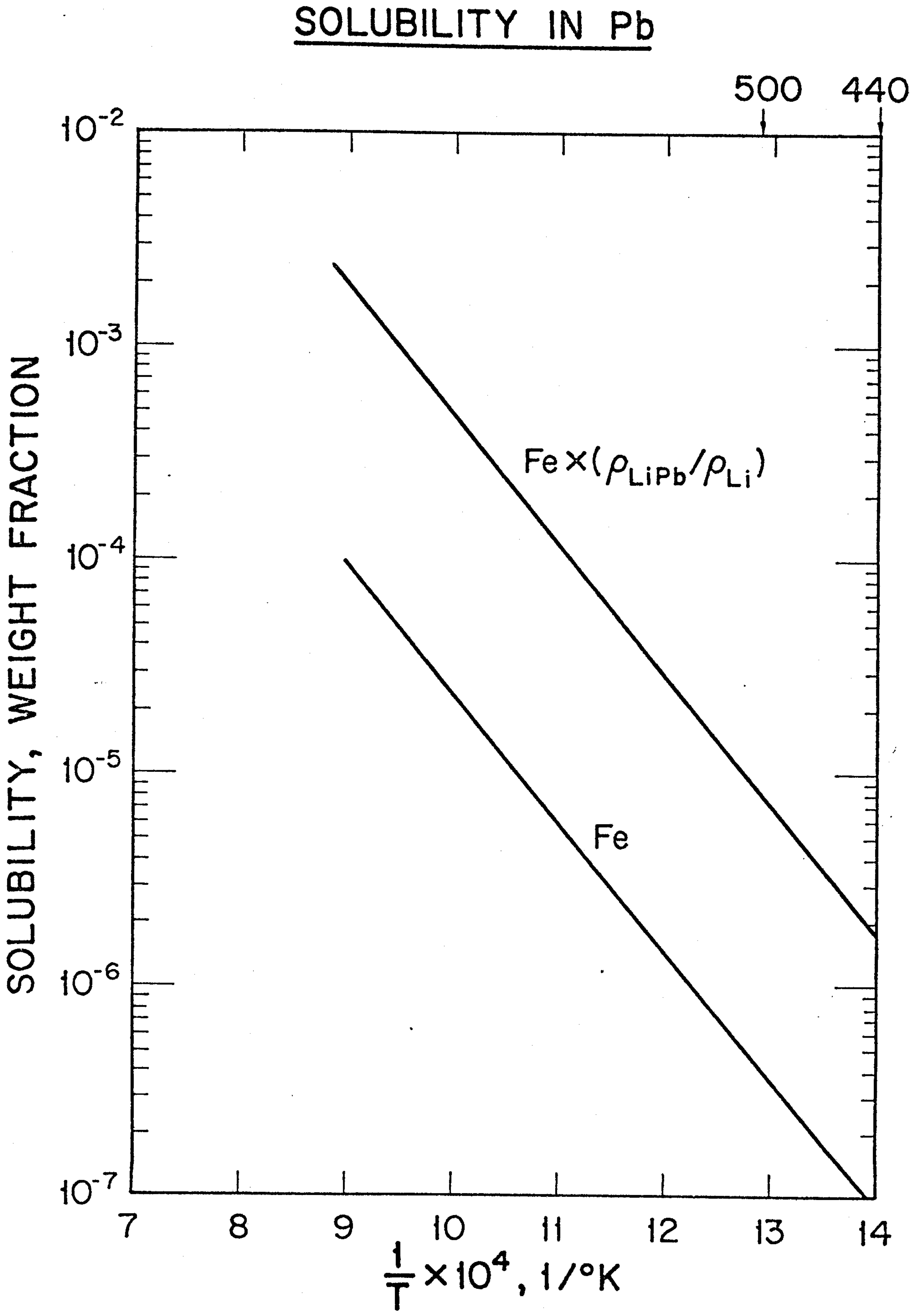
SOLUBILITY IN Pb
500
440
10^{-2}
10^{-3}
10^{-4}
10^{-5}
10^{-6}
10^{-7}
SOLUBILITY, WEIGHT FRACTION
Fe × (ρ_{LiPb}/ρ_{Li})
Fe
7
8
9
10
11
12
13
14
$\frac{1}{T} \times 10^4$, 1/°K

Fig. 8.7

COMPARISON OF Fe/LiPb vs Fe/Li

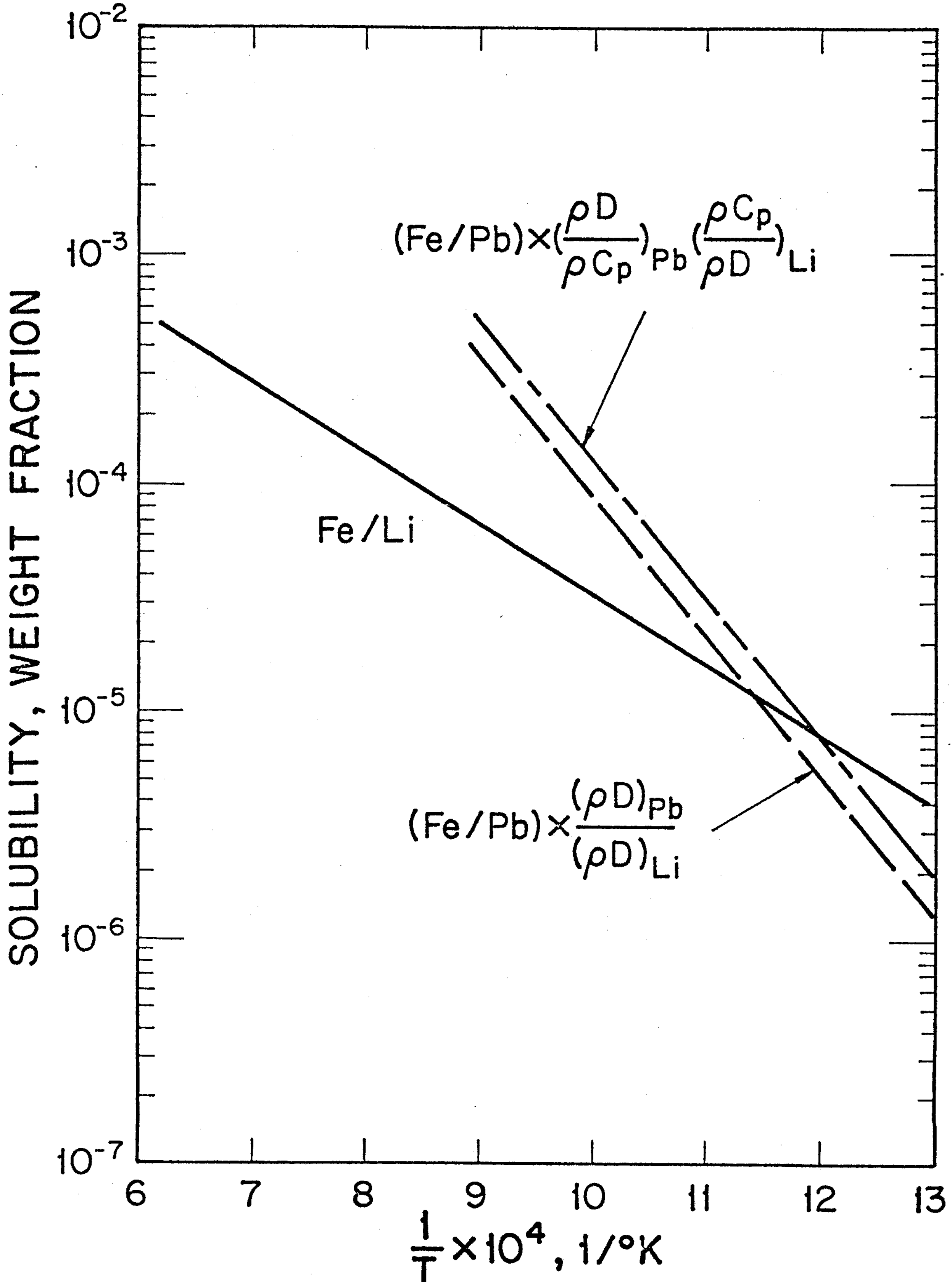

Figure 8.8 shows the comparison of experiemental data of corrosion of Pb and Li on steel in loop tests. At 600°C, the corrosion rate of Pb on steel is about a factor of 3 higher than Li on steel. The theoretical curves shown in Fig. 8.7 predict a factor of 2 higher, which is remarkably close.

Table 8.2 shows the corrosion of Croloy 2-1/2 by lead with a 225 ppm addition of Mg in the lead.(4) After three years of operation at a temperature of 550°C, no corrosion was detected. Therefore, if the corrosion of Pb in steel results in a severe problem in corrosion product transport, an inhibitor can be used to further reduce the corrosion rate.

Table 8.2

Pb and Pb-Mg Eutectic (Group 11A)

Loop #18; Liquid Metal: Pb

	T °C					
	Max	Min		Hr at ΔT	Additives	Remarks
	500	510		3056	225 ppm Mg	Zr added but would not go into soln. Lost all Zr.
	550	460		9100		
	550	430		9975		
	550	415		5634		No corrosion. Slight precipitation in cold leg.
Av:	550	445	Total:	27765		Loop shut down after power failure caused hot leg to overheat.

Fig. 8.8

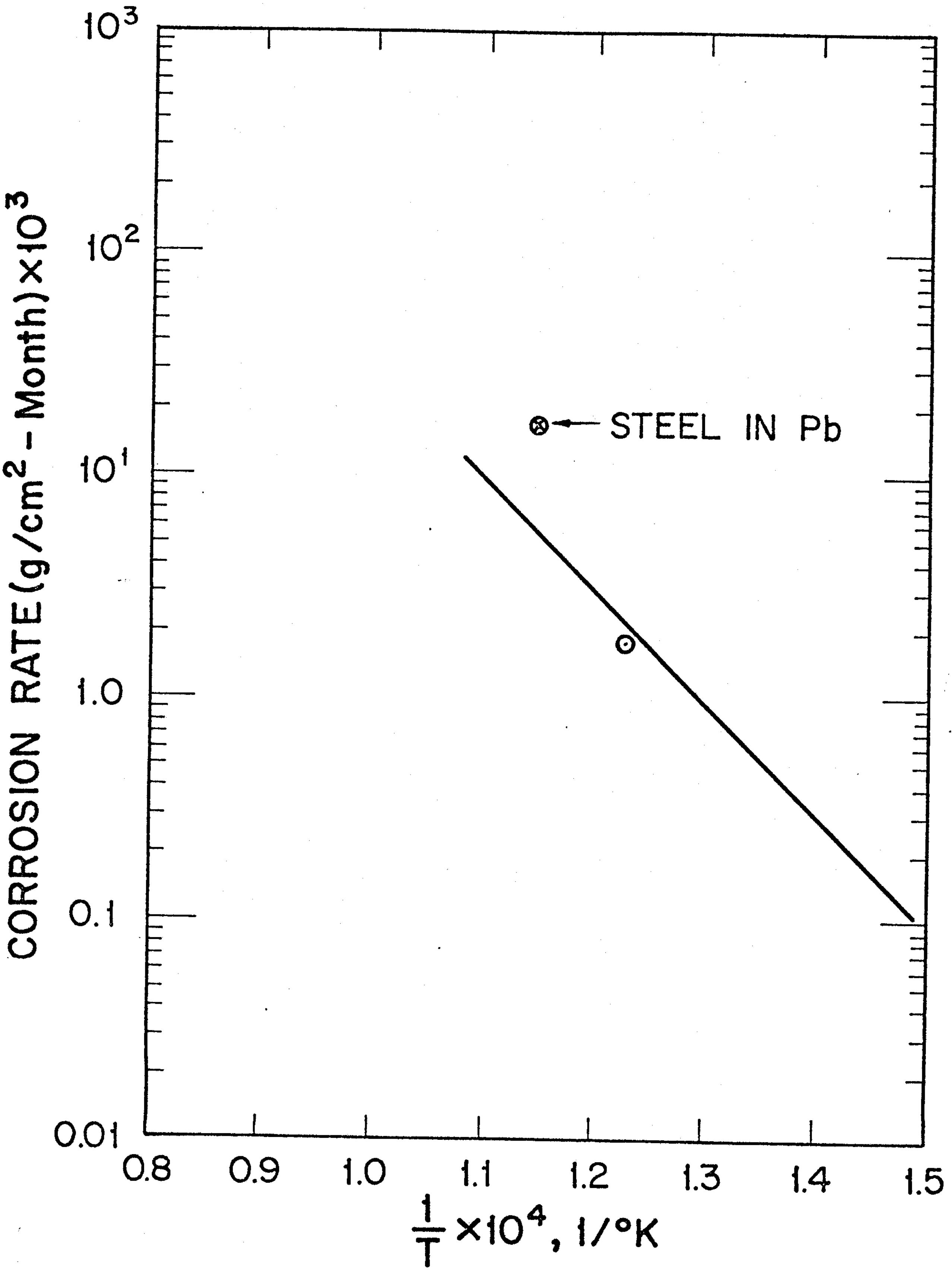
STEEL IN Li
CORROSION RATE (g/cm² - Month) × 10³
10³
10²
10¹
1.0
0.1
0.01
0.8
0.9
1.0
1.1
1.2
1.3
1.4
1.5
1/T × 10⁴, 1/°K
STEEL IN Pb

References for Chapter 8

1. P.F. Tortorelli and J.H. DeVan, "Compatibility of Stainless Steel with Pb-17% At.% Li," The International Corrosion Forum, March 22-26, 1982, Houston, TX.

2. G.M. Tolson and A. Taboda, "A Study of Lead and Lead Salt Corrosion in Thermal Convection Loops," USAEC Report ORNL-TM-1437 (April 1966).

3. R.B. Bird et al., Transport Phenomena, John Wiley and Sons, Inc., 1960.

4. A.J. Romano, C.J. Kamut and D.H. Gurinsky, "The Investigation of Container Materials for Bi and Pb Alloys, Part 1, Thermal Convection Loops," USAEC Report BNL-811 (July 1963).

9. Double Walled Steam Generator and T_2 Permeation

9.1 Heat Exchanger Arrangement and Power Cycle

The power cycle for the PbLi blanket is presented in Fig. 9.1. The MW_t heat input is split in two places to increase the effectiveness of heat transfer. The steam system is 16.6 MPa/482°C with 482°C reheat. The heat transfer temperature diagram, Fig. 9.2, illustrates the effectiveness of the cycle over a system where the first stage reheat and economizer do not share the blanket heat. The evaporator pinch point is moved from 23.5 to 30% of the total heat transferred and the ΔT is raised from 15 to 25°C. This causes a larger log mean temperature difference (LMTD) in the evaporator, first stage reheater and the economizer which reduces heating surface requirements and PbLi inventory. A larger pinch point ΔT also encourages investigation of a higher steam cycle pressure with potential improvements in steam cycle efficiency over that which can be achieved at 16.6 MPa.

9.2 Double Walled Steam Generator

Heat exchange equipment for the HIBALL power cycle must fulfill exacting requirements while at the same time retain design features acceptable to the utility industry. The design requirements of liquid metal to water heat exchangers are complicated by:

- The component must provide a tritium diffusion barrier between blanket coolant and steam cycle.
- The component design must permit practical inspection and maintenance procedures in spite of radiation levels produced by activated corrosion products present in the blanket coolant.

The design described in Figs. 9.3 through 9.6 was created to meet the above requirements. It provides the following features:

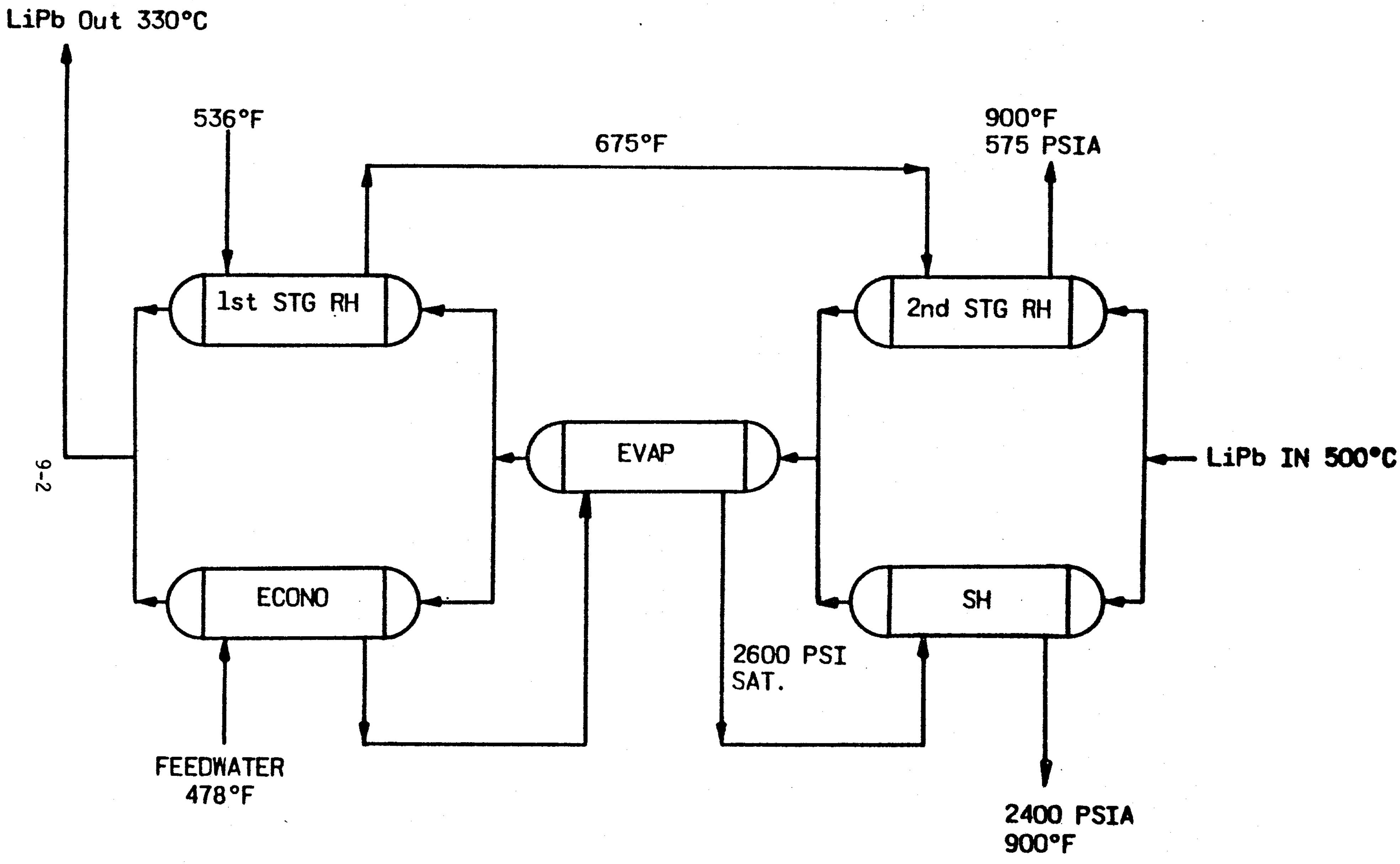

Fig. 9.1 Heat exchanger arrangement.

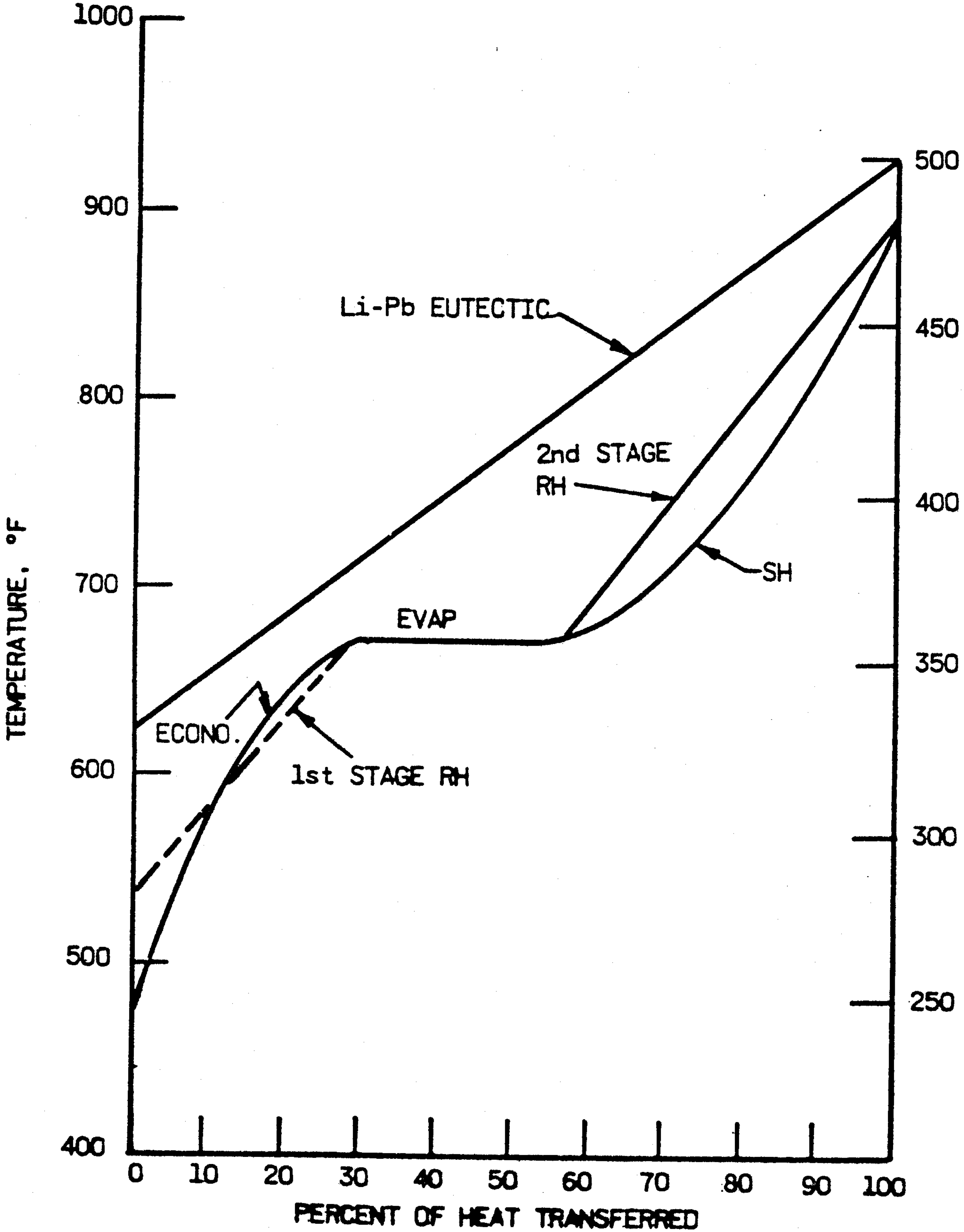

Fig. 9.2 HIBALL temperature diagram for 2400 psia 900°F/900°F steam cycle.

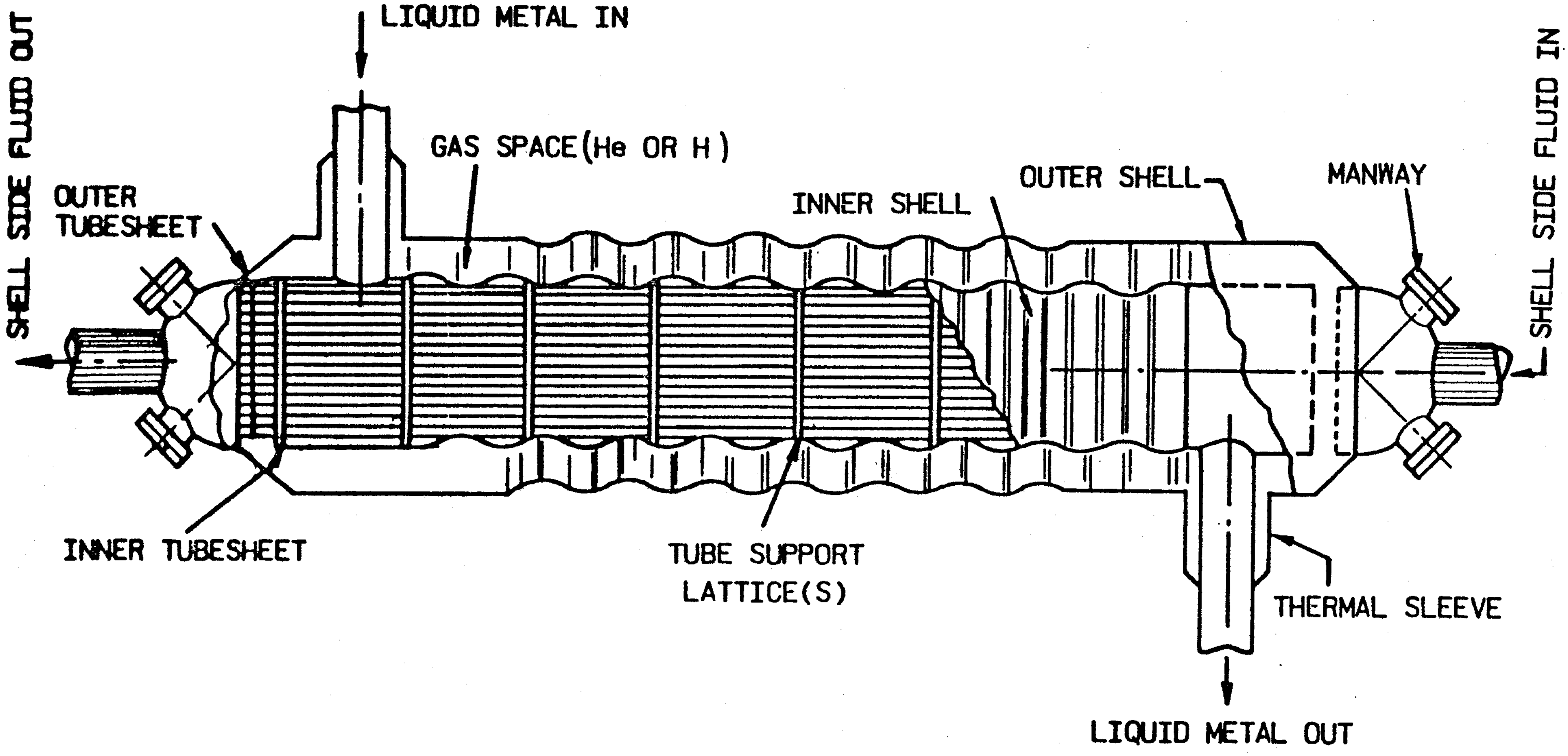

Fig. 9.3 General arrangement.

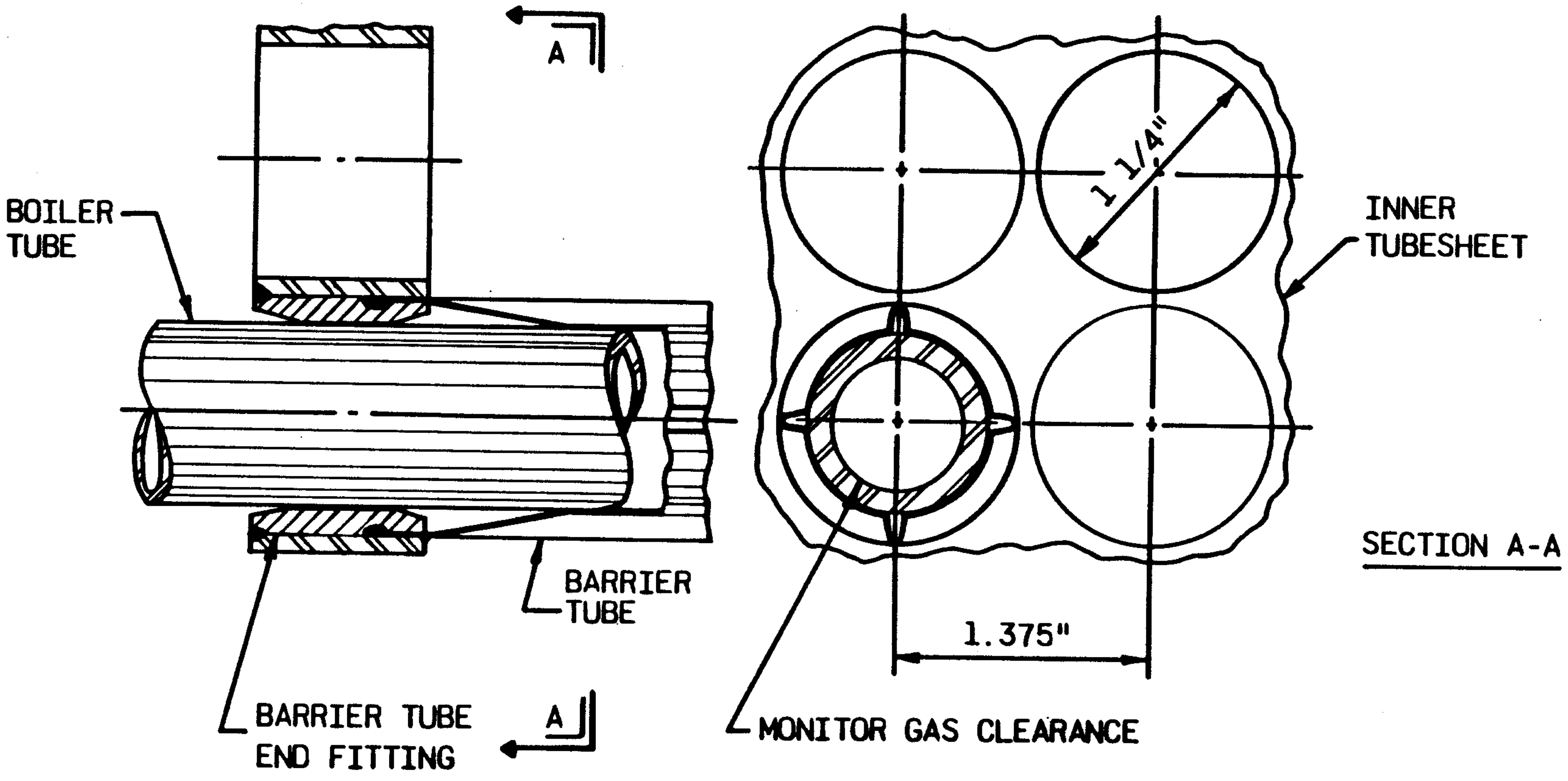

Figure 9.4 Barrier tube to inner tubesheet detail.

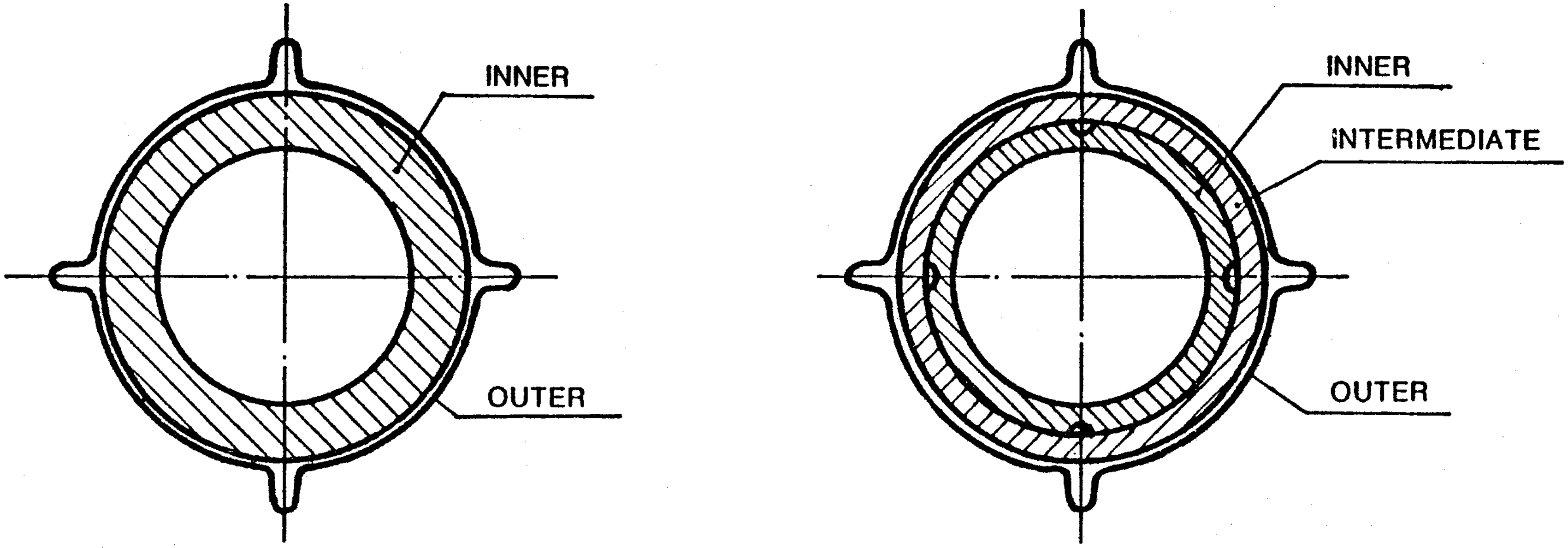

**2 WALL TUBE
(BASE DESIGN)**

**3 WALL TUBE
(OPTIONAL)**

Fig. 9.5 Double walled tube structure.

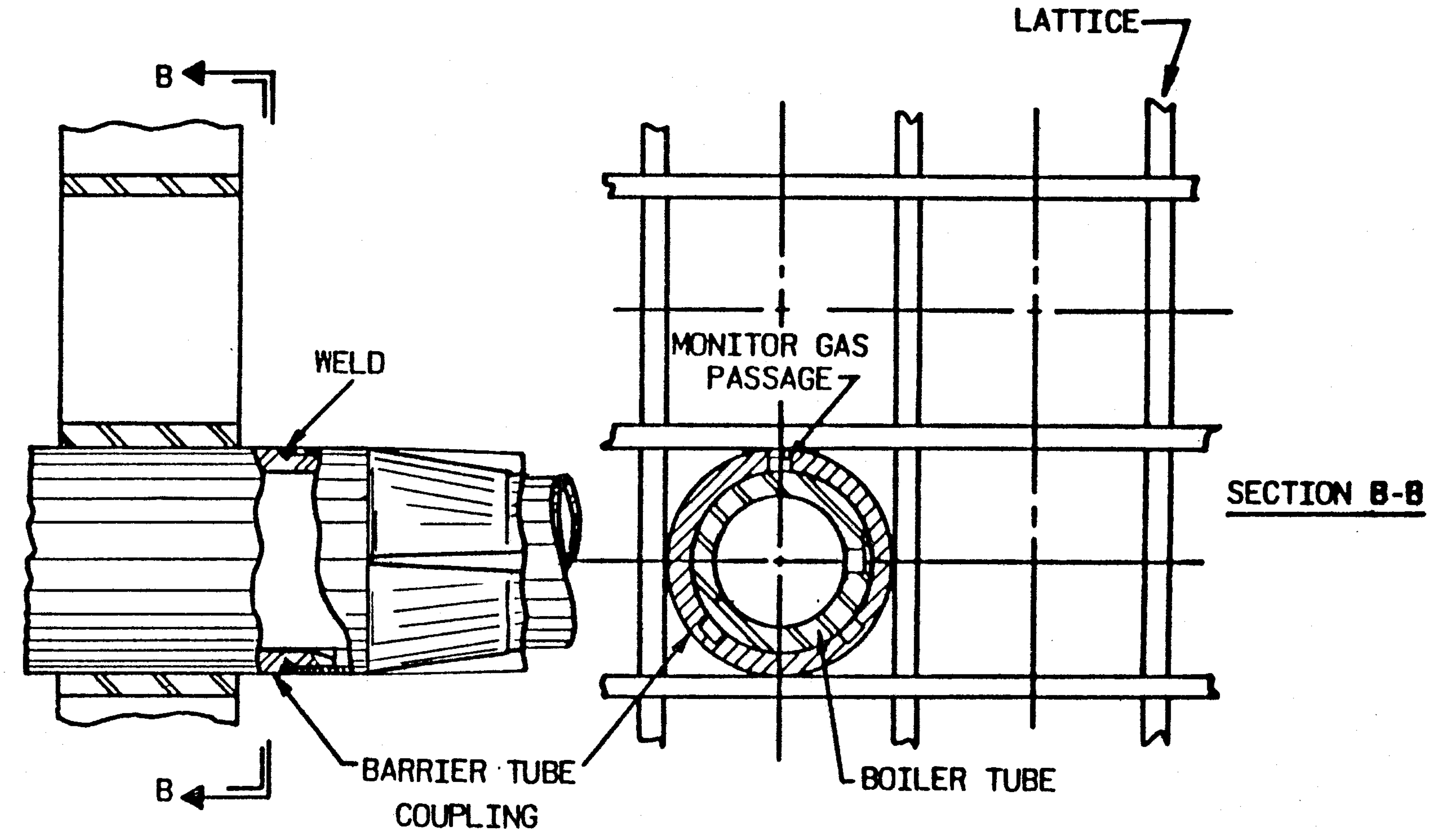

Fig. 9.6 Tube support detail.

1. Provision of an adequate tritium diffusion barrier.
2. Detection of potential tube defects that could lead to metal/water reactions.
3. Avoidance of size limitation problems typical of double walled heat exchangers.
4. Detection, location and repair of leaks by conventional methods (eddy current).
5. More compact construction.
6. More conventional, less difficult component assembly.

The space between inner and outer shells and between inner and outer walls of each tube assembly is filled with helium at 1 atm containing oxygen at a partial pressure of one torr. A pumping system (not shown) is used to circulate this gas longitudinally through each tube wall gap as a sweep (or monitor) gas to detect water vapor.

The hemispherical heads shown in Fig. 9.3 are similar in configuration to those used for "once through" PWR steam generators. Thus the tube inspection and repair equipment developed for this equipment is applicable to the design shown in the above figure. This equipment has been used satisfactorily to perform inspection and maintenance work in radiation levels up to about 15 rem at the hemispherical head tube face.

To cope with higher radiation levels, the manways can be replaced by full opening closures, which in turn will permit use of rotating plugs and other equipment developed in the past for hot maintenance. The effect of activated corrosion product radiation on inspection and maintenance tends to be minimized by the following:

1. Vertical (instead of horizontal) tube sheet faces which reduce collection of corrosion particles on the surfaces.
2. Inner and outer tube sheets with a space between which attenuates streaming of gamma rays through tube ID's.
3. Corrosion products will tend to collect at the top of the inner shell. Radiation from this location will not be in line with tube sheet holes.

9.3 Tritium Isolation

One of the most difficult problems associated with using $Pb_{83}Li_{17}$ is tritium confinement. The very low tritium solubility in $Pb_{83}Li_{17}$ results in a very high tritium partial pressure. The most vulnerable region in the primary loop for tritium leakage is the primary heat exchanger. To improve heat transfer, the surface of the heat exchanger is large and with thin-walled tube construction. Therefore, an effective tritium diffusion barrier is required between the primary loop and the steam cycle to reduce the tritium leakage to an acceptable level.

Hydrogen permeability through different ferritic steels is summarized in Fig. 9.7. The best estimation of tritium permeability through HT-9 is

$$P_e = \frac{1.8 \times 10^3}{\sqrt{3}} \exp\left(- \frac{11100}{AT}\right) \frac{\text{mol } T_2 \cdot \text{mm}}{\text{d} \cdot \text{m}^2 \cdot \text{atm}^{1/2}} .$$

With this permeability and a steam generator area of 3.46×10^4 m^2, the tritium leakage rate is 3.5×10^5 Ci/day. Therefore, a tritium diffusion barrier of 10^5 is needed.

In the HIBALL design, a double-walled heat exchanger is used to provide the required tritium diffusion barrier. The construction, with two tubes in close contact, was shown in Fig. 9.5. A helium purge with 1 torr of oxygen

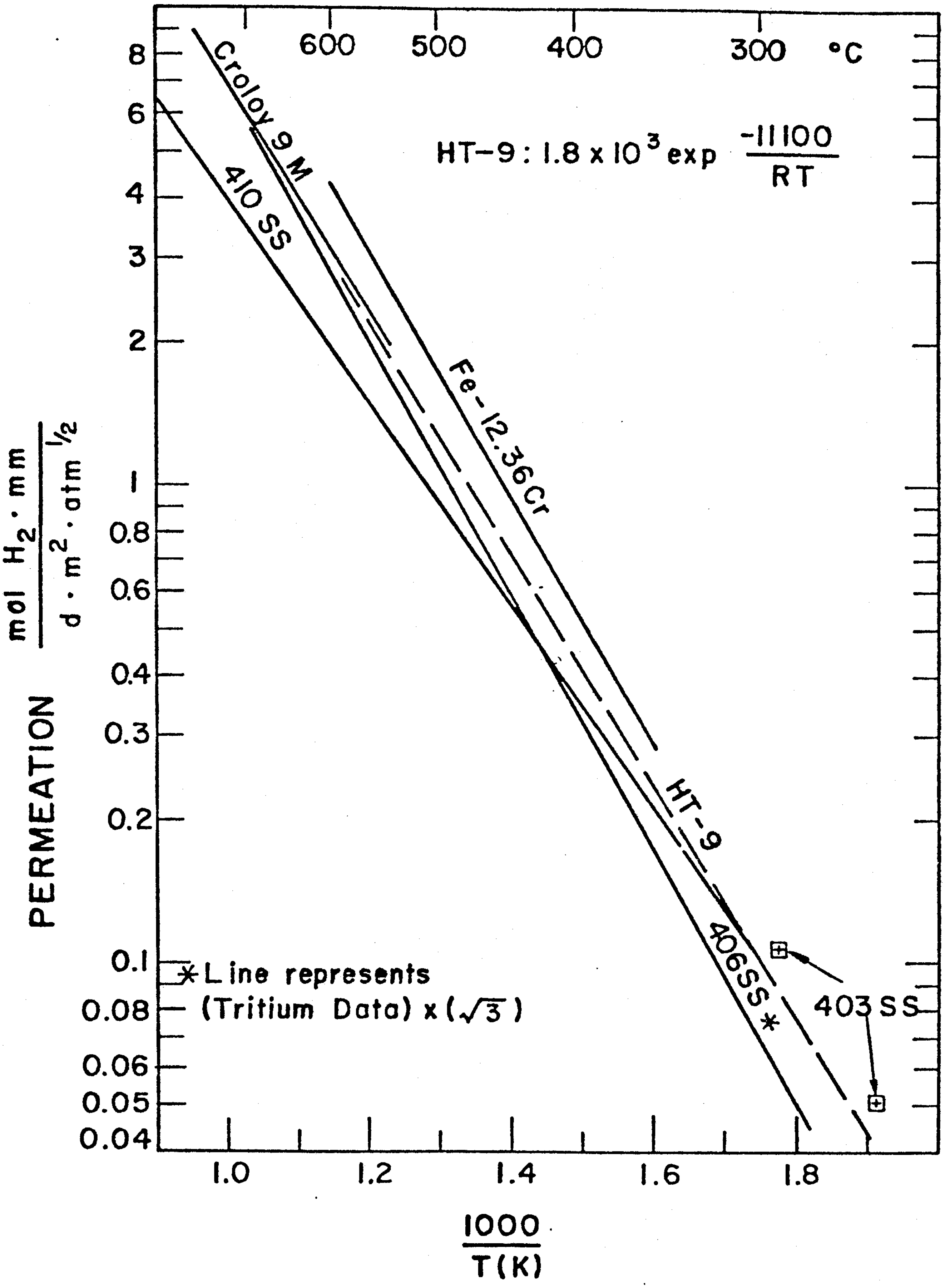

Fig. 9.7 Hydrogen permeation through chromium ferritic steels.

pressure passes through the channels to provide an oxidizing atmosphere between the two tubes. The oxide films formed between the two tubes, as well as the oxide film on the water side, provide an effective diffusion barrier.

Figure 9.8 shows two tritium diffusion paths through the double-walled steam generator. This is an enlarged figure around one contact point between the tubes.

Path 1: Through wall 1, across the gap and through wall 2.

Path 2: Through the contact point.

The resistance to diffusion across the gap is the product of the resistance due to the oxide films and resistance due to the gap. Figure 9.9 shows the attenuation factor due to the gap as a function of the gap width while Fig. 9.10 shows the attenuation factor due to the combined effect of three oxide coatings as a function of single oxide coating layer factor. If the gap width is 10^{-3} cm, the attenuation factor due to the gap is 3×10^{-3}. To obtain a total attenuation factor of 10^{-5}, an attenuation factor of 3×10^{-3} is needed from the oxide coatings, which corresponds to a single layer factor of 20. Experiments have indicated that a single layer factor of a few hundred is available for ferritic steel. It can be concluded, therefore, that the attenuation factor of $<< 10^{-5}$ is available for tritium leakage across the gap.

A two-dimensional, finite difference tritium diffusion calculation was performed for tritium leakage along path 2. The result shows that an attenuation of 10^{-5} is also available along this path. The total attenuation is the sum of the attenuation along those two paths and is, therefore, $< 10^{-5}$.

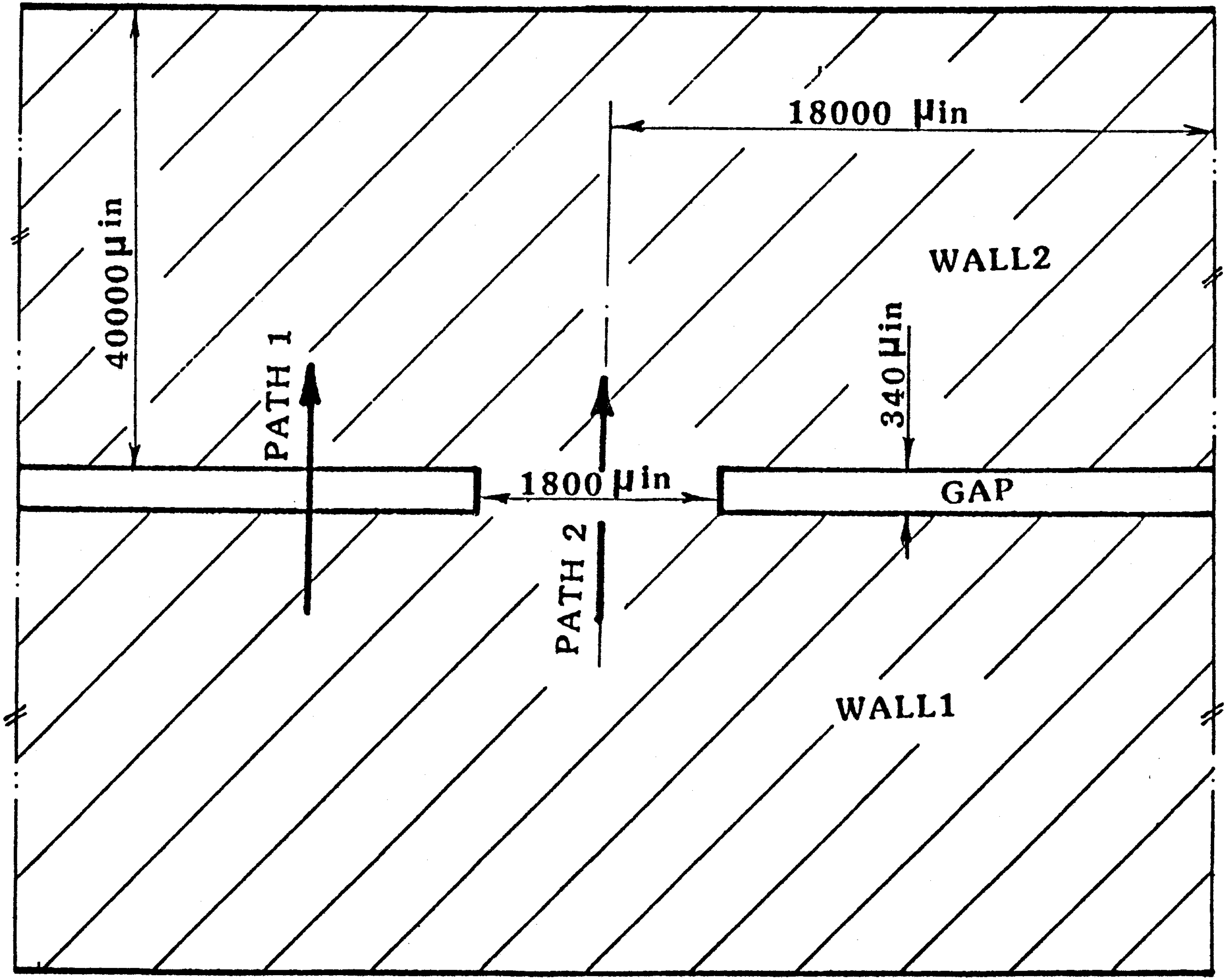

Fig. 9.8 Tritium diffusion path.

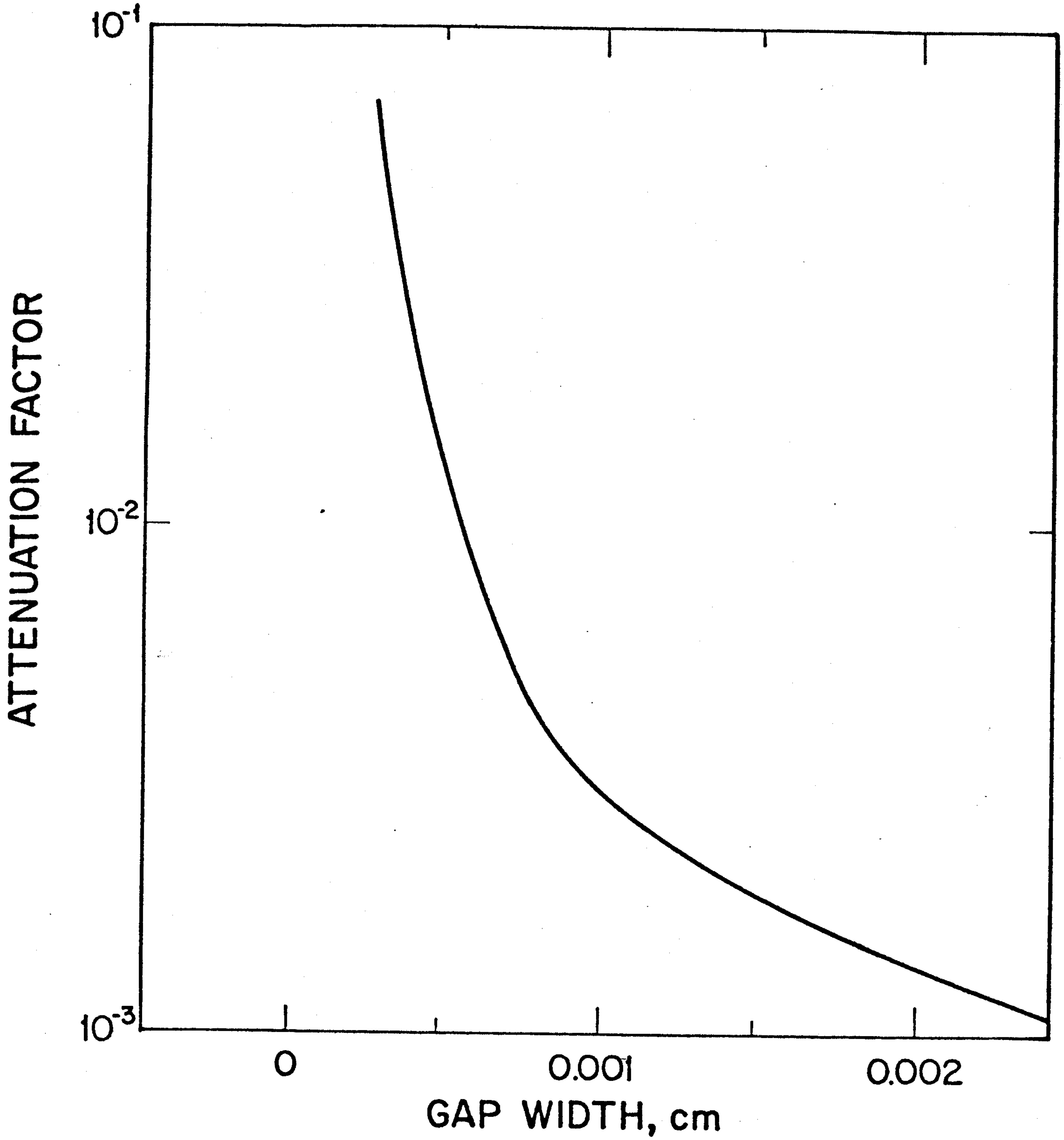

Fig. 9.9 Attenuation factor due to gap.

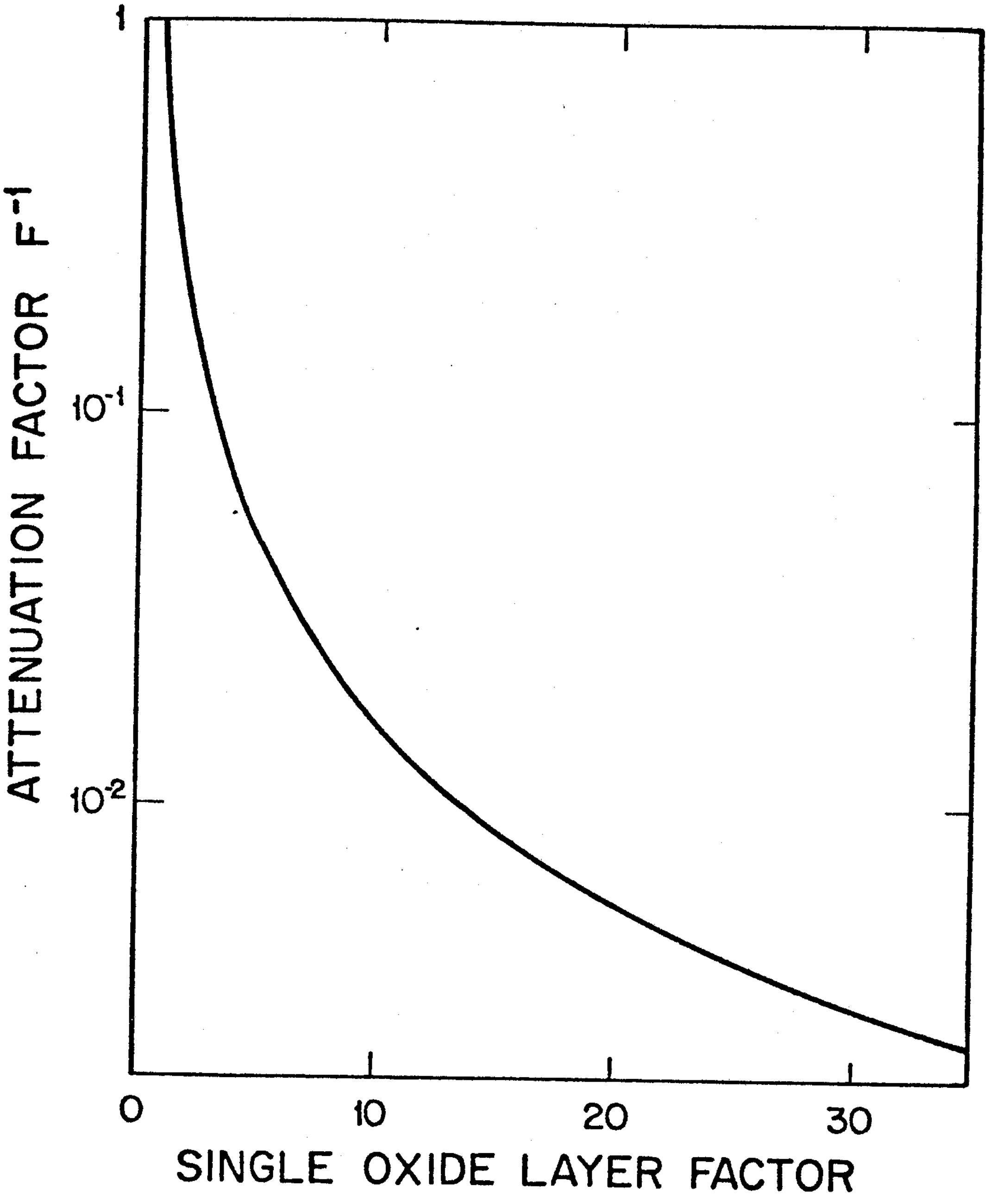

Fig. 9.10 Attenuation factor due to oxide coatings.

10. Tritium Releases from HIBALL

In the HIBALL-I reactor design study the tritium pathways and inventories were analyzed for the blanket and fuel processing systems. In subsequent progress reports the tritium source terms in the blanket and target factory were studied further. The containment systems and the environmental losses have not been studied in detail. A design goal of 10 Ci/d for tritium losses in all chemical forms was adopted. This design goal is a common assumption in many reactor studies; it stems from the premise that containment technology for fusion reactors would be developed to reduce tritium releases below levels experienced in current fission reactors. Normalized tritium production and release rates in present facilities(1) are shown in Table 10.1. The 10 Ci/d value falls between the release values for light water and heavy water reactors in present operation. The distribution of losses between atmospheric and aqueous releases for LWR's and HWR's is illustrated in Table 10.2.

The state of the art technology for controlling tritium losses from reactor coolant water is demonstrated by the Canadian HWR's. Tritium is produced in the heavy water moderator and coolant water primarily by neutron activation of deuterium. Present concentration levels at Pickering in the reactor coolant and moderator water are 0.65 Ci/ℓ and 24 Ci/ℓ respectively. The coolant system, which operates at 11.4 MPa and 310 to 268°C, is the major source of tritium losses. Main pathways for release of tritiated water include leakage from coolant piping and permeation into secondary coolant systems. Moderators, maintained at lower temperatures and pressures, experience less leakage. Losses of ~ 6000 Ci/yr occur during chemical upgrading of the moderator water. Current release values from Canadian reactors (Table 10.3) reflect the present technology for handling tritiated water.

Table 10.1. Normalized Tritium Production and Releases to the Earth's Surface*

Source	Production Rate	Release Rate
LMFBRs	3.5×10^4 Ci/1000MW(e)-yr	540 Ci/1000MW(e)-yr
HTGRs	2.0×10^4 Ci/1000MW(e)-yr	590 Ci/1000MW(e)-yr
LWRs	2.7×10^4 Ci/1000MW(e)-yr	650 Ci/1000MW(e)-yr
HWRs	2.4×10^6 Ci/1000MW(e)-yr	2.4×10^4 Ci/1000MW(e)-yr
Fuel Reprocessing Facilities(a)	---	1.3×10^4 Ci/1000MW(e)-yr
Savannah River	---	7.0×10^5 Ci/yr
Natural mechanisms	1.0×10^6 Ci/yr	1.9×10^6 Ci/yr
Weapons detonations(b)	---	4.6×10^9 Ci

---

* Taken from Reference 1. The most current values are used to reflect the state of the art.

(a) Fuel-reprocessing facilities do not produce tritium but release some produced in irradiation facilities. Values are put on a MW(e) basis by assuming an ^{3}H inventory of 0.78 Ci/kg uranium, 33 MW(e)/kg of uranium burnup, and 365 d/yr.

(b) Values are the release to the earth's surface before 1970. Bans against atmospheric weapons testing have limited subsequent production.

Table 10.2. Normalized Tritium Releases from LWR's and HWR's*

(Ci/1000 MW(e)-yr)

Reactors	Atmospheric Releases	Aqueous Releases	Total Releases
U.S. Boiling Water Reactors			
1973	51 (40%)	76 (60%)	130
1974	49 (44%)	62 (56%)	110
U.S. Pressurized Water Reactors			
1973	86 (4%)	2.2×10^3 (96%)	2.3×10^3
1974	210 (12%)	1.5×10^3 (88%)	1.7×10^3
Pickering Heavy Water Reactors			
1973	2.24×10^4 (88%)	2.97×10^3 (12%)	2.54×10^4
1974	1.54×10^4 (63%)	8.92×10^3 (37%)	2.43×10^4

---

*From Reference (1).

Table 10.3. Tritium Losses from Canadian Reactors[a]

Reactor	Atmospheric		Aqueous		Total
	Ci/yr	% Release	Ci/yr	% Release	Ci/yr
Pickering					
1980	2.1×10^4	(60)	1.4×10^4	(40)	3.5×10^4
1981	1.6×10^4	(68)	7.5×10^3	(32)	2.4×10^4
Bruce					
1980	4.9×10^4	(73)	1.8×10^4	(27)	6.7×10^4
1981	9.2×10^4	(82)	2.6×10^4	(18)	11.2×10^4

(a) Values interpolated from graphs of percentage derived emission limits (DEL) received from Ontario Hydro Nuclear.

Pickering - DEL(water) = 1.4×10^6 Ci/month
DEL(air) = 2.0×10^5 Ci/7 days

Bruce - DEL(water) = 1.2×10^6 Ci/month
DEL(air) = 2.0×10^5 Ci/7 days

Tritium release estimates for fusion reactors have been made in several recent design studies.(2-4) Reactor parameters and release estimates are shown in Tables 10.4 and 10.5. Notice that the release estimates are all approximately 10-20 Ci/d for reactor systems which range in thermal power from 620-4000 MW. A recent study on the environmental effects of fusion done by Oak Ridge National Laboratory (ORNL) for the U.S. Department of Energy, using STARFIRE as a reference design, estimated the tritium losses as 8000 Ci/yr, with 80% released to air and 20% to aqueous environments.(5) Dose calculations based on these values conformed to current standards and were considered acceptable.

Tritium releases from HIBALL were examined in three main categories: (1) losses from fuel reprocessing systems, (2) losses from breeder/coolant systems and (3) auxiliary systems such as building containment and target factory. The tritium parameters for HIBALL are given in Table 10.6.

In order to estimate the tritium losses from fuel reprocessing systems the method used in the ORNL environmental study was followed.(6) Tritium release rates were estimated by scaling projected release estimates from the Tritium Systems Test Assembly(7) (TSTA) with exhaust flow rate. A linear scaling was used; however, this was felt to give an overestimate. In HIBALL both unburned and the bred tritium are pumped from the reactor chamber resulting in a flow rate of 4.4 kg/d through the pumps and fuel processing units. The TSTA vacuum system will handle a tritium throughput of 0.188 kg/d and the fuel processing systems can handle 1.08 kg/d. The total releases for HIBALL from fuel processing units are 1960-3560 Ci/yr as shown in Table 10.7.

In the blanket system, the $Li_{17}Pb_{83}$ breeder and coolant is circulated through a heat exchanger. A double-walled heat exchanger is used to reduce

Table 10.4. Reactor Tritium Parameters

	ETF	INTOR	STARFIRE
Power (MW)			
Thermal	750	620	4000
Electric (Net)	---	---	1200
Tritium flow rates (kg/d)			
Fueled	1.600	1.500	1.296
Burned	0.085	0.074	0.536
Exhausted	1.500	1.430	0.760
Bred	---	0.045	0.562
Burn Fraction (%)	5.0	5.0	42.0
Breeder/Coolant	---	Li_2SiO_3/H_2O	$LiAlO_2/H_2O$
Inventory (kg)			
Pumps	0.130	0.120	0.063
Fuelers	0.020	0.020	0.054
Fuel Processing	0.130	0.180	0.154
Blanket		0.5-7.1*	7.4-380*
Blanket Recovery Systems	---	0.020	0.281
Storage	2.550	2.200	1.071

---

*Radiation effects included.

Table 10.5. Tritium Release Estimates

Source	ETF	INTOR	STARFIRE
Coolant			
Steady-State Concentration(Ci/ℓ)	0.001-0.1	0.003-0.03	~ 0.3
Leak Rate (ℓ/d)	1000-100	100-1000	30
Tritium Release (Ci/d)	1-10	3	~ 10
Buildings			
Volume (m^3)	$3x10^5$	$3x10^5$	$4x10^5$
Tritium Level (μCi/m^3)	5	same	same
Leak Rate (vol.%/d)	$3x10^{-5}$	same	same
Tritium Release (Ci/d)	<< 1	< 1	< 1
Ventilation			
Volume (m^3)	$3x10^5$	$3x10^5$	$2x10^4$
Tritium Level (μCi/m^3)	5	same	same
Number of Tritium Releases	< 5-7	5-10	5
Tritium Release (Ci/d)	8-10	8-16	< 1
Solid Waste			
Tritium Release (Ci/d)	< 1	< 1	~ 1
Total			
Tritium Release (Ci/d)	10-20	11-20	~ 13

Table 10.6. HIBALL Tritium Parameters

Power (MW)	
Thermal	10152
Electric (net)	3768
Tritium Flow Fates (kg/d)	
Fueled	4.10
Burned	1.20
Exhausted	2.90
Bred	1.50
Burn Fraction (%)	29
Breeder/Coolant	$Li_{17}Pb_{83}/Li_{17}Pb_{83}$
Inventory (kg)	
Pumps	0.370
Fuelers	---
Fuel Processing	0.124
Blanket	0.025
Blanket Recovery Systems	---
Target Factory and Storage	10-80*

---

*24 hour fill process for target production.

tritium permeation. Calculational analysis of the effectiveness of the double-walled steam generator has been done (see Chapter 9). Calculations predict that losses can be kept to ~ 10 Ci/d.

Tritium is present in the $Li_{17}Pb_{83}$ at a pressure of 10^{-4} torr and temperatures ranging from 330-500°C. Liquid metal holding tanks will be composed of thick, well-insulated walls to prevent heat loss and reduce tritium permeation. Large diameter, thick-walled, insulated piping is used to transport the lithium-lead. Aluminum sleeving can be used to provide a secondary containment barrier around piping. Additional jacketing or gloveboxes can be used to enclose valves, liquid metal pumps, or other components where leakage may occur.

Water coolants are used in HIBALL to cool the shield and other auxiliary reactor components. Auxiliary cooling systems should be far removed from the reactor core and should, therefore, be essentially tritium free. In the shield coolant small amounts of tritium will be produced by activation or permeation from reactor systems. The shield coolant operates at low temperatures (60-45°C) and pressures and does not produce recoverable heat; therefore, leakage from the shield coolant can be minimized. Estimated losses from water coolants are ~ 1 Ci/d.

The buildings which handle tritium will contain an atmospheric tritium recovery unit. This unit is designed to handle routine releases of tritium and releases as a result of standard maintenance procedures. In this system the tritium is catalytically oxidized and then absorbed onto molecular sieve beds.

Tritium losses due to building leakage are expected to be small. Using the same leakage rate as in STARFIRE, 3×10^{-5} vol.%/d, and a tritium concentration of 5 μCi/m^3, the leak rate from a containment volume of ~ 10^7 m^3 is < 1 Ci/d. Releases from the tritium facilities for HIBALL (~ 10^5 m^3) can be kept at about 1 Ci/d if there are two atmospheric turnovers per day under normal conditions. Tritium release through beam ducts which penetrate the primary containment building should be small. Active pumping is located throughout the beam lines to maintain a vacuum.

The target factory will contain the largest portion of the tritium inventory (10-80 kg). This inventory includes 8-28 kg in the fuel filling process, 0.5-12 kg in fuel recovery and 4-40 kg stored as targets for delivery to the reactor. This inventory is based on a 24 hour DT fill process. The range is due to two different possible modes of target production.(8) The leakage rate is difficult to determine. There is no existing target facility which can be used as an example. Also, the means of producing the HIBALL target has not been addressed and, therefore, the temperatures and handling conditions of the tritium are unknown. The target factory is assumed to be located on the reactor site in a facility separate from the reactor buildings. The conditions in the target factory can be carefully controlled to minimize losses. A large portion of the inventory (30-67%) will be stored as cryogenic targets. The transport of targets to the reactor has also not been addressed. The technology for handling tritium fuel in the target factory will be similar to the reactor fuel processing units. The loss rate is estimated to be of the same order of magnitude, ~ 10 Ci/d.

The summary of tritium losses is reported in Table 10.8. The total losses are estimated at about 30 Ci/d. Using the ORNL study guidelines, the losses are assumed to be 80% to air and 20% to water environments. The release rate is larger than for STARFIRE (~ 20 Ci/d); however, the size and

Table 10.7. Estimate of Tritium Releases from Fuel Reprocessing Systems

	Tritium Release	Ci/yr
	TSTA	HIBALL
Vacuum System	80-150	1800-3400
Fuel Cleanup Unit	Releases go to tritium waste treatment. No significant release to the environment.	
Isotopic Separation	20	80
Tritium Waste Treatment	20	80
Total Release Rate	120-190	1960-3560

Table 10.8. Summary of Tritium Losses from HIBALL

	Release Estimates Ci/d
Fuel Reprocessing Systems	5.5-10
Double-walled HX	10
Water Coolants	~ 1
Building and Atmospheric Recovery Systems	~ 2
Target Factory	~ 10
Solid Wastes	~ 1
Total Releases	30-34

power output from HIBALL are much larger. Analysis of the environmental effects of these losses should be studied.

References for Chapter 10

1. J.E. Phillips and C.E. Easterly, "Sources of Tritium," Nuclear Safety 22, 612-626, Sept.-Oct. 1981.
2. P.A. Finn, R.G. Clemmer and B. Misra, "Tritium Management Requirements for D-T Fusion Reactors (ETF, INTOR, FED)," Argonne National Laboratory, ANL-81-32.
3. W.M. Stacey et al., "US Contribution to the International Tokamak Reactor Phase-1 Workshop, Conceptual Design," USA INTOR/81-1 (1981).
4. C.C. Baker et al., "STARFIRE - A Commercial Tokamak Fusion Power Plant Study," Argonne National Laboratory, ANL/FPP-80-1 (1981).
5. "Draft Generic Environmental Impact Statement," Oak Ridge National Laboratory, Sept. 1982.
6. "Background Information & Technical Basis for Assessment of Environmental Implications of Magnetic Fusion Energy," Oak Ridge National Laboratory, Working Draft, Aug. 1982.
7. J.L. Anderson and R.H. Sherman, "Tritium System Test Assembly Design for Major Tritium Device Fabrication Review," Los Alamos National Laboratory, LA-6855-P (1977).
8. K.E. Plute and D.K. Sze, "A Modified Production Scheme to Reduce the Tritium Inventory in an ICF Target Factory," University of Wisconsin Fusion Engineering Program Report UWFDM-453 (to be published).

11. Fusion Safety Consideration For HIBALL Design

11.1 Introduction

Historically, reactor safety has been based on the concept of preventing the release of radioactive material to the environment following an unanticipated transient or accident. The method of prevention for current light water reactors (LWR) and fast breeder reactors has been a defense in depth; i.e. multiple containment barriers between the radioactive materials and the environment. For an LWR the primary source of radioactivity resides in the fuel, and defense in depth involves: (1) the fuel rod cladding and the assurance of its integrity during operation, (2) the primary coolant system and the prevention of leaks, and (3) the reactor containment building and the maintenance of its integrity during an accident. For a fusion energy system the concept of defense in depth could be applied; however, the nature, quantity and location of the radioactive materials is different.

In the LWR the primary sources of radioactivity are the fuel and the associated products produced in the fission process which reside in the zirconium clad fuel rods (e.g., 20 billion curies of radioactivity at shutdown for an 3100 MWt plant). The amount of radioactivity present in the surrounding structure, caused by neutron activation, and in the coolant, caused by corrosion product activation, is insignificant compared to this residual radioactivity in the fuel (more than two orders of magnitude smaller).

In the present designs for a fusion power plant the only radioactive "fuel" is the tritium which is in the plasma and the associated fueling systems. The amount of tritium present in the fusion reactor usually represents a small amount of radioactivity; i.e. relatively insignificant compared to an LWR (~ 1 kg of tritium or 10 million curies, a factor of 1000 less).

The tritium is enclosed within the vacuum boundary, and this with the reactor containment building comprises the multiple barriers of isolation from the environment. Because the neutrons produced by the fusion reaction are so energetic (14.1 MeV) the largest amount of radioactivity in the fusion system is found in the surrounding structure (blanket, reflector, and shield) where neutron activation induces radioactivity. The amount of radioactivity is large compared to that in an LWR surrounding structure, but still lower than that from the fuel and fission products in an LWR (e.g, for the HIBALL-I reactor design,(1) for 3100 MW_t about 2 billion curies at shutdown). The structural material activated is within the vacuum boundary for the fusion reactor (i.e., blanket and reflector) and also makes up the vacuum boundary (shield). The amount of radioactive corrosion products is approximately similar to that in an LWR. These are important differences in the amount and location of radioactivity, and this causes the safety concerns in fusion to be different.

A second consideration that one must remember is that in current LWR's the efforts in reactor safety for reducing the probability of an accident or for mitigating its consequences are being performed for very specific reactor designs. In a sense the safety investigations are confirmatory in nature where specific designs are evaluated with respect to accidents and modifications in the designs are made if needed.

In sharp contrast to this, safety research for a fusion power system can only focus its attention on generic issues, because the detailed fusion reactor designs are not available. In a sense this is quite beneficial because a broader design approach to safety can be undertaken. In this approach the fusion power system would have a set of goals for reliability; e.g. the fusion device will be designed to have an availability of 80%; and for safety; e.g. the probability of an accident involving a loss of the coolable geometry and the subsequent release of a significant fraction of its radioactivity will be designed to be less than 10^{-6} per reactor per year. Then, as part of the plant design, system reliability can be increased, probable accident paths can be identified, and consequences of fusion power system accidents can be assessed. Current trends in fusion reactor safety seem to stress the assessment of consequences more than improvement of the reactor design from a reliability standpoint.

In delineating the major generic safety concerns for a fusion power plant, we exclude steady-state operation and startup and shutdown of the system. The focus of the discussion will be on unanticipated transients and accidents that may lead to a release of radioactivity to the environment. If one accepts a safety design goal of a minimal release of radioactivity (e.g., the stated goal of 10^{-6} per reactor per year) then the approach is to design a system which minimizes the probability of a loss of the coolable geometry for the reactor, and investigates the system interactions and physical processes that are key to improving the design or that may be involved in causing a radioactivity release. Calculation of accident consequences fits into this framework primarily in the sense of assessing the impact of various radioactive source terms on the environment.

A possible list of these system interactions or physical processes is given below:

1. Power-cooling mismatch when the fusion power system is still at some level of power, e.g. a loss of flow accident while at power;

2. Power-cooling mismatch when the fusion power system is shut down, e.g. a loss of heat sink and failure to remove the decay heat; local quenching of the plasma on the first wall, e.g. a plasma disruption event;
3. Physical processes which can lead to overpressurization of containment by combustion or pressurization, e.g. lithium-water reactions in the blanket or coolant causing local heating and hydrogen generation;
4. Power-cooling mismatch in the magnet or vacuum pumping systems, e.g. a magnet quench or loss of cryogenic heat sink;
5. Asymmetric loading of the blanket and first wall by fireball;
6. External events, e.g. earthquakes or tornadoes.

This list, although not complete, gives an overall picture of what one should consider in the design of the fusion power plant system. Some of the issues given above have a greater impact on the design and provide redundant systems to assure a high reliability in reactor shutdown, blanket and reflector cooling, and magnet stability. Others are physical processes that should be understood in terms of their impact on how containment integrity might be threatened by possible chemical and physical reactions. In this sense the design would be affected by the choice of materials one makes for the blanket, structure, and coolant, and on what loads are to be designed for in the containment and pipe support structure. Figure 11.1 presents a description of some of the safety concerns in each area. Early work in fusion safety(2) considered a number of these generic issues when reviewing first and second generation fusion reactors.

11.2 Siting of the HIBALL Reactor

For any proposed reactor, the reactor performance, inherent and engineered safety features, and the quality of the design are all important

Fig. 11.1. Major Issues in Safety and Their Interrelation

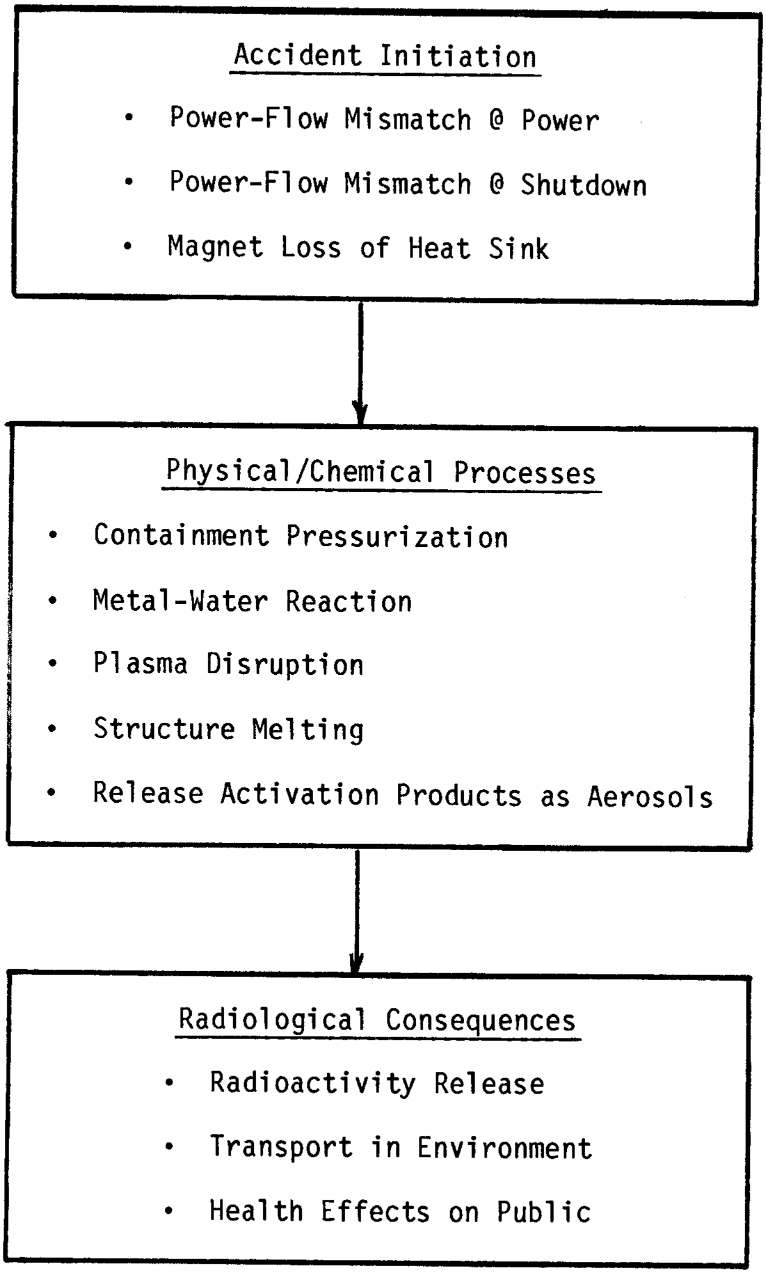

factors that must be considered when evaluating a plant site. For a particular site, land area, topography, meteorology, emergency planning all enter in an evaluation. Consideration of these as well as other issues of hazards analysis involves so many variables that it would be quite impossible to anticipate all situations. Therefore, when establishing the site boundaries one must consider the extremely unlikely occurrence of a release of radioactivity from the power plant. The probability and consequences of a severe reactor accident have been the subject of widespread interest and study since the earliest days of reactor development. To date, however, the technology has not progressed to the point where it is possible to assign, with a high degree of certainty, quantitative numbers to all significant factors relative to accident initiation, physical processes, or containment failure and health effects. Therefore, when the release of radioactivity is considered for a severe accident, conservative analyses must be done to bound the effects of the accident, and to establish the site boundaries beyond which the impact of the accident on the public health and safety is minimal.

For a fusion reactor design there are not directly relevant siting criteria. However, one can use the current siting criteria for light water reactors(3,4) with some alterations for a fusion reactor design. The major modification for a fusion reactor design is that the radioactive source term for the fusion reactor fuel is tritium. This is in contrast to the large number of fission product species in an LWR. We do not consider the radioactivity in the blanket, reflector, and shield at this time, because it is as yet unclear how the activation products could be mobilized and spread throughout the environment. Possible mechanisms for the mobilization of these radioactive sources are now being considered, and some of these are discussed later.

The regulatory guides set forth a calculational procedure to estimate the exclusion area boundary and the low population zone distance for the power plant. The exclusion area boundary is of such a size that an individual located at its boundary for two hours immediately following onset of the postulated radioactivity release would not receive a total radiation dose to whole body in excess of 25 rem and 300 rem to the thyroid. The low population zone is that distance in which the same total dose would not be exceeded for a person at this boundary for the entire time of the radioactivity release ($t \rightarrow \infty$). The 25 rem dose corresponds to the once in a lifetime accidental exposure for radiation workers. It is considered here as a reasonable basis for preliminary reactor siting calculations.

The radioactive source term used in these calculations is conservatively assumed to be the entire inventory of tritium in the fusion reactor. We neglect the tritium in the storage facility or the pellet factory, because these are separate facilities and would have their own safety and environmental isolation systems. For the HIBALL design this results in a tritium inventory of about 0.5 kg ($\sim 5(10^6)$ curies). This postulated source term is not based on any mechanistic analysis; rather it is a conservative upper bound source term for the fusion reactor "fuel." We will consider physical processes that may release this tritium and any of the radioactive activation products in the next section.

The procedure used to calculate these radioactive doses and the site boundary distances has been conservatively simplified. Because of this, one should be aware that the stated results are approximations which tend to over-predict the radiation dose one would receive from such a severe accident and radioactivity release. To illustrate this some parametric calculations are performed to show the sensitivity to the parameters. The key assumptions are these:

1. No credit is taken for the effect of washdown or filtering of the source term from engineered safety features. These systems could provide decontamination factors of one or two orders of magnitude.
2. The release rate of the tritium from the reactor containment building to the environment is assumed to occur at a constant leakage of 1.0% of the volume per day. This is a design number which may be altered by the designer.
3. Atmospheric dispersion of the radioactivity from the containment is assumed to occur according to the dispersion relation of Sutton(5) as modified by Gifford(6) and Meade(7) for the downwind direction at a zero release height.
4. It is assumed that a shift in a wind direction does not occur for the duration of the leakage from containment. This would further disperse the effluent and reduce the dose by an order of magnitude.
5. Atmospheric dispersion is assumed to occur under inversion type weather conditions. The actual weather conditions at most sites would be more favorable allowing further dispersion (factor 10-1000 more).
6. Decay of the source is considered during its holdup in the containment but neglected during its transit to the receptor point. This is not a significant conservatism.

Consider an instantaneous release of tritium (puff release) from the containment; the amount of radioactivity inhaled by an individual downwind from the release point is given by (4)

$$I_{p_g} = C_0 \; R \; D_I \tag{11.1}$$

where C_0 is the amount of radioactivity released, R is the breathing rate (or ingestion rate) and D_I is the dispersion rate in the atmosphere given by

$$D_I = \frac{1}{\pi U \theta_y \theta_z} \exp\left(- \frac{y^2}{2\theta_y^2} - \frac{h^2}{2\theta_z^2}\right) \tag{11.2}$$

where U is the wind speed, θ_y and θ_z are the atmospheric turbulence dispersion parameters for the horizontal and vertical directions respectively, y is the horizontal distance away from the downwind direction, and h is the vertical release height. If the amount of radioactivity released from the reactor containment building occurs in a continuous fashion over some time period then C_0 is a function of time and given by

$$C_0 = C_{TOT} \left(\frac{\lambda_{LK}}{\lambda_{LK}+\lambda_r}\right) [1 - \exp((-\lambda_{LK} - \lambda_r)t)] \tag{11.3}$$

where C_{TOT} is the total inventory in the containment, λ_{LK} is the leakage rate from the containment expressed in the fraction of the total released per unit time, and λ_r is the radiological decay constant.

The dose from this inhaled radioactivity can be calculated by a couple of methods. One method is to use the average decay energy of the radioisotope, $\bar{E}$, and the average time constant for removal of the radioactivity from the body, λ_e; the total dose is then given by

$$D_{p_g} = C\, I_{p_g}\, E\, [1 - \exp(-\lambda_e t)]/m_p \lambda_e \tag{11.4}$$

where m_p is the mass of the organ (in this case the whole body), and C is a constant equal to $3.7(10^8)$ (dps/curie) (rems/erg). Another method is to use published dose conversion factors for the radioisotope; e.g. for tritium these would be $1.48(10^{-7})$ mrem/picocurie inhaled (from NUREG-0172), or $0.84(10^{-7})$ mrem/picocurie inhaled (from ICRP-30).

For the base case assumptions of downwind exposure, zero release height and stable atmosphere, calculations were performed and results are presented in Fig. 11.2. We have plotted the dose for the low population zone distance because it governs the offsite dose results. Parametric calculations have also been performed to investigate the effect of some of these assumptions; results are given in Table 11.1. For example it is interesting to note that the conservative base case calculation including the effect of skin absorption results in a low population zone distance of about 1-2 kilometers. This distance is quite small for the HIBALL design considering the distance from the reactor cavities to the accelerator is also about 2 kilometers. Therefore, such a low population zone distance would present no more of a problem for siting than would simply siting the reactor and the associated accelerators.

One also notes that the assumptions of downwind, zero release height dose with stable weather conditions result in a large conservatism. If any one of these factors are included at all, then the dose decreases markedly. Finally, it is interesting to note that because the half-life for tritium is so large, the leak rate of the containment does not have a large effect on the dose to

Figure 11.2

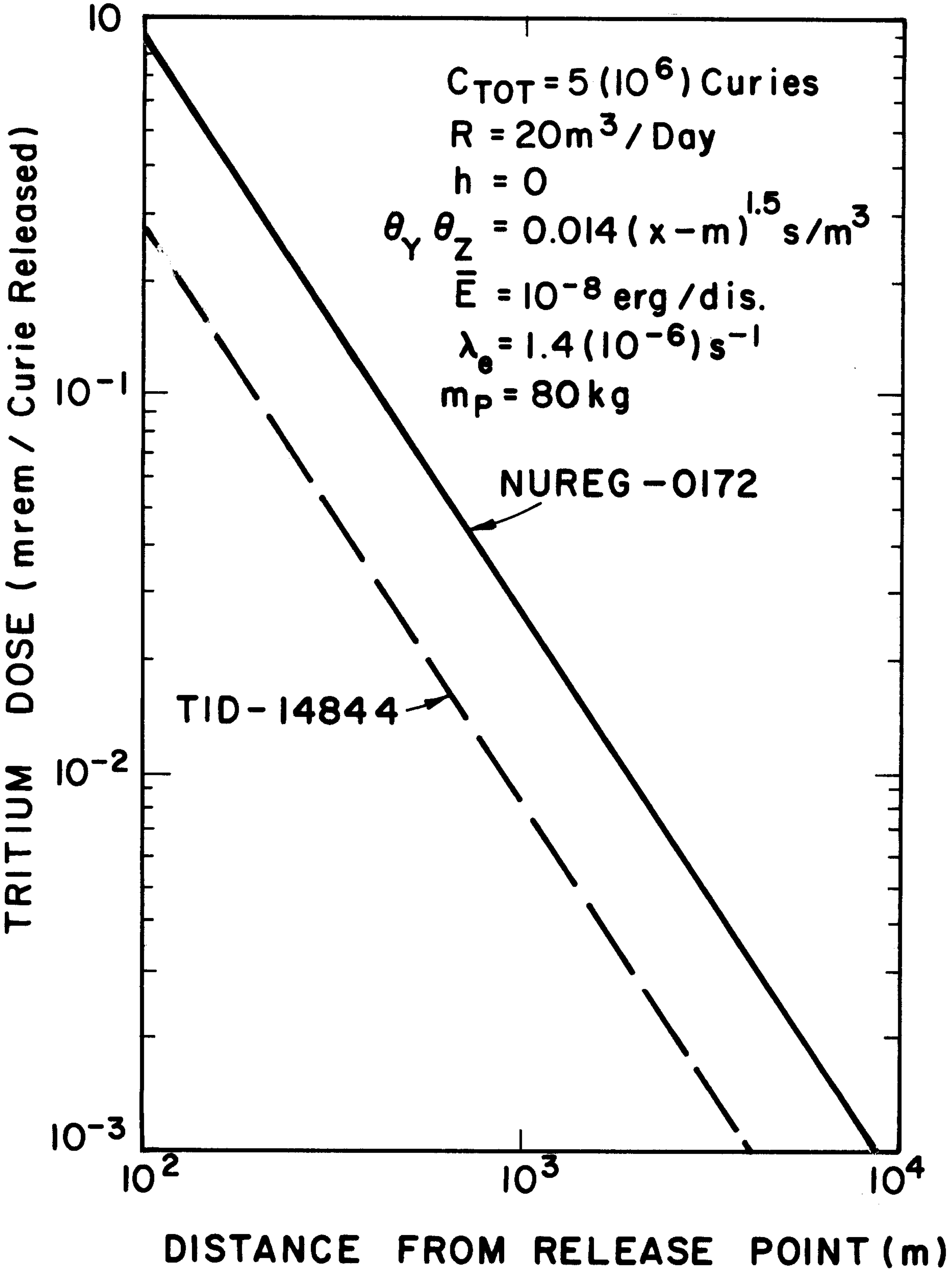
10
10^{-1}
10^{-2}
10^{-3}
10^2
10^3
10^4
TRITIUM DOSE (mrem / Curie Released)
DISTANCE FROM RELEASE POINT (m)
$C_{TOT} = 5(10^6)$ Curies
$R = 20 m^3/Day$
$h = 0$
$\theta_Y \theta_Z = 0.014 (x-m)^{1.5} s/m^3$
$\bar{E} = 10^{-8}$ erg/dis.
$\lambda_e = 1.4(10^{-6}) s^{-1}$
$m_P = 80 kg$
NUREG-0172
TID-14844

Table 11.1. Offsite Dose for the Low Population Zone Distance (in rem)

Distance	100 m	1000 m	10000 m
Specific Cases			
Base Case	1140 rem	36 rem	1.1 rem
Inclusion of Skin Absorption Increase Dose by 50%	1700	54	1.6
Vertical Release Height of 25 m	0	0.0001	0.5
Offwind Direction @ 45°	~ 0	~ 0	~ 0
Unstable Wind Conditions (Type C)	127	4	1.2
Change of Leakage Rate to 0.01%	427	13	0.4
Puff Release	1142	37	1.1

the individual. Varying the release rate by a few orders of magnitude only changes the dose by a factor of two to three.

Taking these results together implies that the containment of tritium during a severe fusion reactor accident is not as much of a concern as might be expected. Rather it is the containment of the radioactive activation products in the blanket, reflector and shield that must be considered. Although this radioactivity is in an immobile form, the remote possibility exists that some fraction of it could be released into the environment and have an impact on the public health and safety. Given the possibility and the fact that the release of these more immobile radioactive materials is highly unlikely (low probability), a probablistic approach to the problem of safety analysis is required.

If a probabilistic approach were taken then a quantitative safety goal is needed so that one can decide what accidents or transients must be designed for and which are truly incredible in regard to the design. One such safety goal might be that the reactor and containment system will be designed so that a loss of its coolable geometry and a significant radioactivity release to the environment would be less than 10^{-6} per reactor per year. Then, as part of the design process, the system reliability and possible accident paths can be identified. For those systems where the failure rate may be unacceptable, redundant features can be added so that the overall design will meet the safety goal. Accidents which fall into this category ($P_a > 10^{-6}$) must then be analyzed and calculations must show what is the likely outcome for specific designs, with an accurate quantification of safety margins. Accidents which fall below this probability would be deemed incredible, and would be analyzed only insofar as their consequences are assessed for a specific design; i.e. risk assessment not accident mitigation. A suggested methodology would then be for a given reactor design:

a) assert a design safety goal based on risk;

b) identify accident sequences and determine which are important to the system design;

c) for those accident sequences within the design envelope perform detailed calculations to better define the physical processes and the system criteria needed to mitigate their effects;

d) for those accident sequences outside the design envelope perform scoping calculations to determine the accident progression and its consequences.

11.3 Key Physical Processes

For a probabilistic approach to fusion safety to be viable a number of physical processes must be generically investigated in order that engineered safety systems be properly designed (e.g. decay heat removal systems, containment design). A list of some of these generic physical processes is given below:

1. Reactor decay power and stored energy
2. Molten-metal - water reactions
3. Hydrogen combustion
4. Melting and ablation processes
5. Aerosol formation and transport
6. Radioactive dispersion.

During the design of the HIBALL reactor decay power has been calculated as well as a detailed listing of the radioactive materials in the blanket, reflector and shield. We have begun to consider the physical process of molten-metal-water interactions and discuss this below. The remaining generic issues are now being investigated in relation to light-water and fast breeder reactor safety; only a brief discussion of how they would be involved in fusion designs is discussed at this time.

It is recognized that a molten metal can interact with water in such a way as to produce hydrogen and an accompanying release of mechanical energy. However, the magnitude of the interaction is highly dependent upon the metal composition, its temperature and mass, and the mode of contact between the metal and water. One of the efforts of the HIBALL design is to quantify the magnitude of the lithium-lead/water interaction that might occur in the blanket of the fusion power reactor, in the metal to water steam generator, or in the accompanying primary coolant loop and containment. One should realize that because some of the physical processes involved with molten metal/water interactions are not fully understood, our current analysis is scoping in nature and should be verified by experiments and more detailed analysis. In this discussion we present simple models for liquid-metal/water interactions to aid in understanding current data.

There have been scoping experiments performed by Clemmer et al.(8-10) at Argonne National Laboratory and by Jeppson, et al. (11) at HEDL using lithium and lithium-lead alloys in which the molten metal is poured into a water pool. The results of these experiments have indicated that molten lithium-lead (i.e., 17Li83Pb) undergoes a qualitatively more benign reaction than lithium. There are two physical processes that are involved in a metal-water interaction:

1. Physical explosion (alo called vapor explosion or fuel-coolant interaction) where the hotter liquid (molten metal-"fuel") mixes with the colder liquid (water - "coolant") rapidly producing high pressure steam and the fuel is finally fragmented.
2. Chemical reaction and burning where the molten metal which mixes with the water undergoes exothermic oxidation and produces hydrogen gas and the hydrogen burns.

The reasons why such a difference may exist are not completely known at this time. We suggest three possible reasons:

1. The relative temperature rise for the lithium-lead alloy (17Li83Pb) is smaller than for molten lithium during oxidation.
2. The lower reaction temperature coupled with realistic chemical kinetics produces slower reactions rates.

Table 11.2. Thermodynamics for Lithium and Lithium-Lead*

	Li	17Li83Pb
Heat of reaction, J/kg_{Li}	-34.3	-28.4
Summation of the thermal inertia of the reaction product, J/°K	73.2	158.1
Adiabatic temperature rise, K	3560	880
Maximum reaction zone temperature, K	4060	1380

---

*For the reaction of one mole of Li in $Li + H_2O \rightarrow LiOH + 1/2\ H_2$.

3. The surface area available for reaction is probably smaller for the lithium-lead alloys.

The relative temperature rise for a 17Li83Pb-water chemical reaction is lower than for lithium. If one computes the thermodynamic maximum reaction zone temperature derived from a stoichiometric reaction of one mole of lithium and water, one finds that the maximum temperature is ~ 4350 K for lithium and ~ 1750 K for 17Li83Pb (see Table 11.2). The major reason for the difference is the large thermal inertia of the lithium-lead alloy in comparision to lithium.

This difference in the reaction zone temperature manifests itself in the chemical kinetics of the reaction. As the reaction zone temperature increases, the process of vapor phase oxidation becomes more dominant. Vapor phase oxidation occurs when the molten metal temperature increases to such an extent that the metal vapor pressure rises and metal vapor diffuses toward the water vapor and oxidation occurs. The vapor phase reaction kinetics are much more rapid than the liquid-metal/water reaction because the protective oxide layer on the metal surface does not inhibit the vapor phase reaction. For lithium at ~ 4350 K the partial pressure is ~ 10^5 torr, whereas for 17Li83Pb at 1750 K the lithium partial pressure is ~ 1 torr (the Li activity in 17Li83Pb is 10^{-3}). This suggests that vapor phase oxidation would be much less of a concern for 17Li83Pb. In fact, if one uses data from sodium-water reactions, vapor phase oxidation becomes dominant when the metal vapor partial pressure rises above 100 torr. This analogy suggests that vapor phase oxidation is not a concern with 17Li83Pb.

In the absence of vapor phase oxidation the kinetic rate of reaction per unit area of molten metal in water (i.e., steam because of film boiling between the metal and water) is controlled by the rate of steam diffusion to the metal surface and the rate of diffusion of oxygen through the oxide surface layer into the liquid fuel phase. Although the kinetics of the lithium-lead alloy reaction have not been measured, we believe that the rate of reaction would be lower than pure lithium for two reasons. First, the chemical activity of 17Li83Pb is much lower than lithium. Second, the rate of reaction would be reduced because the lithium would be more quickly depleted near the surface of the metal for lithium-lead because of its low mole fraction (17 a/o).

Finally, the total rate of oxidation is the product of the kinetic rate per unit area and the total molten metal surface area. Based on current research in fuel-coolant mixing with a drop or pouring mode of contact,(12) it appears that the rate of mixing and, therefore, the rate of fuel surface area generation is given by

$$\frac{dA_f}{dt} \sim \frac{6V_f}{C_o D_f} \tag{11.5}$$

$$C_o \equiv \left(\frac{t}{T^+}\right) \exp\,(-T^+) \tag{11.6}$$

$$T^+ = \frac{tv_f}{D_f}\left(\frac{\rho_c}{\rho_f}\right)^{1/2} \tag{11.7}$$

where A_f = fuel surface area

V_f = fuel volume

D_f = initial fuel diameter (length)

t = time

v_f = fuel relative velocity

ρ_c/ρ_f = density ratio of coolant to fuel.

Notice that as the coolant to fuel density ratio decreases (as would be the case for 17Li83Pb) the rate of area generation decreases. Slower mixing and area generation implies less surface area available for chemical reactions. Therefore, mixing takes ~ 3 times longer for 17Li83Pb than for lithium. These results should be verified by experiments with molten metals and water.

Our preliminary results suggest that the rate of chemical reaction of lithium-lead is qualitatively less than lithium.

Once hydrogen is produced from molten metal-water interactions it may then be released to the containment atmosphere. If the containment atmosphere contains oxygen in the proper proportions, it can recombine with the hydrogen exothermically to produce water. This chemical reaction is of concern because the energy that might potentially be released could overheat the containment atmosphere causing the pressure to rise, thereby causing containment failure by overpressurization. In this regard a fusion power plant like the HIBALL design must consider hydrogen combustion in its containment design. Most probably the structural loading of the containment would have to be designed to withstand some amount of hydrogen combustion as well as a condensible vapor release; i.e. a coolant blowdown.

If the decay heat removal systems malfunction in the fusion power plant over long periods of time (more than a few hours) then the afterheat in the activated structure will eventually overheat and melt. This melting would cause the activated structural material to slump. This slumping molten mass could thermally attack the containment structure (steel and concrete), producing gases and radioactive aerosols. Although these physical processes would not be considered in the containment design, they are important from a risk standpoint. This is because the processes described could permit the radioactive materials in the structure to be released into the containment as mobile aerosols, and to the environment if the containment were to fail by overpressure. This is the only conceivable way these highly radioactive materials could be dispersed in the atmosphere and present an environmental risk to the general public.

There is no current work in this area of fusion safety; however, given the potential risk it seems prudent that some calculations be done to scope out the questions and identify key issues.

References for Chapter 11

1. B. Badger et al., "HIBALL- A Conceptual Heavy Ion Beam Driven Fusion Reactor Study," UWFDM-450, University of Wisconsin; also Kernforschungszentrum Karlsruhe Report KfK-3202 (December 1981).

2. W.E. Kastenberg et al., "Safety of Fusion Reactors," PPG-342, UCLA (October 1977).

3. "Reactor Site Critera," Title 10, *Code of Federal Regulations*, Part 100 (10CFR100), (February 1962).

4. J.J. DiNunno et al., *Calculation of Distance Factors for Power and Test Reactor Sites*, USAEC, TID-14844 (March 1962).

5. O.G. Sutton, "A Theory of Eddy Diffusion in the Atmosphere," *Proc. Roy. Soc.* (London), *135A*, 143 (1932).

6. F.A. Gifford, "Use of Routine Meteorological Observations for Estimating Atmospheric Dispersion," Nuclear Safety *2*, 47 (June 1961).

7. P.J. Meade, "Meteorological Aspects of the Safety and Locations of Reactor Plants," *World Meteorological Organization*, Tech. Note No. 33, 13 (1960).

8. R.G. Clemmer, D.R. Armstrong, et al., "An Experimental Study of the Reaction of Li_7Pb_2 With Water," Trans. Am. Nucl. Soc. *32*, 71 (1979).

9. R.G. Clemmer, D.R. Armstrong, et al., "The Reactions of Li-Pb Alloys With Water," Trans. Am. Nucl. Soc. *34*, 55 (1980).

10 A.G. Rogers, B.L. Benedict, et al., "Liquid Li-Pb-Bi, a New Tritium Breeder," Eng. Fusion Research Proc., Chicago, October 1981.

11. D.W. Jeppson and R.F. Keough, "Fusion Rector Blanket and Coolant Material Compatibility," Proceedings of the Second Topical Meeting on Fusion Reactor Materials, Seattle, WA (August 1981).

12. M.L. Corradini, "A Proposed Mode for Fuel-Coolant Mixing," Trans. Am. Nucl. Soc. *41*, 405 (1982).

12. Costs

The costs for HIBALL were published in the original report. Since then, a new driver scenario has been proposed, utilizing Bi^+. In the following section, the tables affected by the change in the cost of the driver will be amended and a new capital cost and busbar cost will be derived. For consistency, the original 1981 dollar values will be used and the same rate of exchange (2.5DM per US$) used at the time the report was issued will be retained.

Table 12.1 gives the new driver costs in DM and lists the increment factor over the initial HIBALL driver. The total increase in the driver cost is 51.5%. Table 12.2 gives the breakdown of the direct costs and Table 12.3 the indirect costs, interest during construction and the grand total cost in 1981 dollars.

The target costs, operation and maintenance, component replacement and interest on capital are based on the same assumption as in the original report. Table 12.4 gives the busbar costs for an assumed availability of 70% and a 10% interest on capital.

The effect of the new driver scenario on HIBALL is to increase the capital cost by 23% and the busbar cost by 20%. In spite of these increases, HIBALL still appears to be competitive with other fusion systems.

Table 12.1. Cost Breakdown for New Driver Utilizing Bi$^+$

	Properties	Cost Details (MDM)		Cost (MDM)	Cost Factor vs. HIBALL
Linac	length x 2	Structures	600	4900	3.1
	current x 4 beam power x 8	Tubes + Ampl. DC power	3636		
	pulse length x 1/8	Cables, etc.(x1.5) Tunnel	705		
Beam Lines	36 km			1200	1
Rings					
Kickers, Septa	Higher Stiffness!			100	1.5
RF in SR				50	1
Final Bunch RF	Instead of IL!			100	0.125
Final Lenses	Less Emittance!			140	0.5
Misc.				650	1
Total Driver				7150	1.515

Table 12.2 Breakdown of Direct Costs

	$\$ \times 10^6$ (1981)	
Reactor Plant		
Reactor cavities (4)	785	
Pellet injectors (4)	15	
Main heat transfer system	560	
RF linac	1960	
Transfer ring (1)		
Condenser rings (5)		
Storage rings (10)	900	
Beam lines		4220
Balance of Plant		
Land and land rights	5	
Structures and site facilities	280	
Turbine plant and heat rejection	430	
Electric plant equipment	275	
Miscellaneous plant equipment	50	1040
		5260

Table 12.3 Indirect Costs and Interest During Construction

		$\$ \times 10^6$ (1981)
Total Direct Costs		5260
Indirect Costs		
Construction Facilities (15% of TDC)	790	
Engineering & Cost Management (15% of TDC)	790	
Owners' Costs (5% of TDC)	260	1840
Interest During Construction		1210
5%/Annum Deflated Interest,		
8 year Construction Period		
Grand Total Cost		8310

The net electric power output of HIBALL is 3768 MWe. Thus the capital cost is:

$$\text{Capital Cost} = \frac{\$8310 \times 10^6}{3768 \times 10^3 \text{ kW}} = \$2205/\text{kWe} \cdot$$

This can be compared with other recent fusion designs (escalated at 5% to $1981):

STARFIRE	2100 $/kWe
NUWMAK	2227
WITAMIR	2236
UWTOR-M	2047

Table 12.4 HIBALL Busbar Costs

Assumptions: 70% availability

10% interest on capital

3768 MWe net power output = 2.31×10^{10} kWh/hr

$$\text{Busbar costs} = \$\ \frac{(66 \times 10^6 + 166 \times 10^6 + 64 \times 10^6 + 831 \times 10^6)\ 1000\ \text{mills/\$}}{2.31 \times 10^{10}\ \text{kWh}}$$

= 48.8 mills/kWh.

Some of the other recently designed fusion power systems have the following busbar costs (escalated at 5% to $1981):

STARFIRE	36.9 mills/kWh
NUWMAK	37.8
WITAMIR	37.9
UWTOR-M	36.2

13. Future Work

The HIBALL concept is a large, complex system involving many new ideas and situations. Since the time for the study was limited, many of these have either not been treated as completely as would be desired or their effect on the remainder of the system has not been addressed. This section is an attempt to enumerate some of the areas in which additional work is needed or alternative ideas should be considered. It will be limited primarily to the reactor chamber and its immediately associated systems. The problems associated with the accelerator and beam transport are not included unless they have a direct effect on the cavity design. The discussion will follow the order of the previous sections of this report and will not try to establish relative priorities between the various sections.

13.1 Cavity Atmosphere, Beams, and Targets

In this area, the primary concern for HIBALL is the condensation and evaporation of the lead-lithium on the INPORT tubes. The importance of this problem is clear since the time to reach a suitable pressure for beam propagation determines the allowable repetition rate of the chambers and thus the plant power level. While considerable progress has been made in the analysis, it is not yet in sufficiently satisfactory condition to be used to establish definitive criteria.

A second problem which is related to the previous one is the cavity gas requirements for beam transport. A more complete analysis and better values of the charge exchange cross sections would result in a more certain value for the allowable chamber background pressure.

Should the condensation characteristics of the cavity gas turn out to be such that ballistic focusing is not possible at the desired repetition rate, it would be desirable to consider beam propagation in the self-pinched mode. If this were to be considered, then such topics as beam propagation, cavity gas requirements, final focusing magnets, target heating, and gas flow up the beam lines would have to be considered.

In addition, attention should be given to beam plasma effects in the ion-target interaction.

13.2 INPORT Units

The INPORT tubes form an integral and unique part of HIBALL. The primary emphasis here should be on demonstrating that the concept will work. Questions to be answered are related to: the wetability of SiC by lead-lithium, the strength of the fibers and the tubes at temperature, the proper fiber size and weave for the tubes, the maintenance of the liquid surface on the outside of the tubes, and the stability of the tubes with high internal coolant flow. Some of these questions can only be answered by experiment. It would be quite desirable if a model for the INPORT tubes could be developed to predict the mechanical properties of the tubes and the fluid flow through the walls of the tubes. Such a model would permit comparison with experiment and could suggest suitable fiber size and weave characteristics.

13.3 Neutronics, Radioactivity, and Corrosion

The calculations for the beam ports in HIBALL were based on generic magnet and shield designs. These calculations indicated that radiation levels in the magnets presented no special problem. They also showed that some portions of the beam lines were overdesigned. A more detailed analysis based on realistic magnet designs, the presence of vacuum ducts, and optimized shields would provide a much more satisfactory description of this part of the system.

A second area which should be treated in more depth touches on radioactivity, materials, and safety problems. The transport of corrosion products throughout the primary loop has not been considered in this work (nor indeed has it been considered in any detail in any other study). The primary area of concern is that corrosion leads to the transport of radioactivity throughout the system as well as the presence of activity in the coolant itself. In order to evaluate shielding requirements, maintenance techniques, cleanup systems, and source terms for safety studies, this problem should be considered in some detail.

13.4 Tritium

Once of the largest contributors to the tritium inventory in HIBALL is the target factory. However, the detailed design of the factory, the actual processes used and the projected inventories associated with these processes have not been well established making it difficult to get good values for the total inventory and to determine tritium release rates and cleanup systems. In addition, the transport of targets from the factory to the reactor, the associated inventory, and the hazards incurred in transit have not been discussed.

Another area needing continuing work is to determine the expected tritium release rates from the rest of the plant outside the cavity. This encompasses such things as more detailed estimates of releases from piping, valves, and treatment systems as well as further work on the permeation of tritium in double wall steam generators.

A third area involving both tritium and safety has to do with tritium diffusion up the beam lines in routine or abnormal conditions. For example, if it is necessary to have a shutter of some sort in the beam line, how fast should it operate and where in the beam line should it be?

13.5 Safety

The overall conclusions of the current work on HIBALL are that: (1) tritium release does not pose a large problem in terms of plant siting or offsite doses during an accident; (2) the physical processes involved with metal-water reactions may pose the greatest threat to containment integrity through hydrogen generation and combustion; and (3) the risk assessment of the plant in time of accident would be most affected by mobilization of the activated structure, perhaps by structure melting and aerosol production. It appears then that future work ought to be directed in three specific areas:

1. Analysis of molten metal-water interactions so that the physical process may be understood in terms of hydrogen production rates under various conceivable contact modes; specifically for current fusion reactor designs.
2. Analysis of hydrogen combustion in containment to determine what loads must be withstood for structural design of the passive radioactivity barrier and what design measures should be employed to mitigate the effects of hydrogen burning.
3. Analysis of the physical processes which may cause structure melting, slumping, and possible aerosol formation; these processes play a large role in the potential for containment failure and dispersal of radioactivity to the environment.

13.6 Summary

These areas suggested for future work represent only a portion of the things that should be considered for HIBALL. Satisfactory resolution of some of them is vital if HIBALL is to be completely credible from a technical standpoint. It is also necessary if it is to be acceptable from an environmental point of view. When work proceeds on these issues, additional areas of concern will probably become apparent and will have to be resolved in turn. However, resolution of the issues enumerated here will represent considerable progress in the quest for a credible and economic design of a heavy ion fusion reactor.